INSTITUTO SUPERIOR DE ENGENHARIA DO PORTO
MESTRADO EM ENGENHARIA BIOMÉDICA



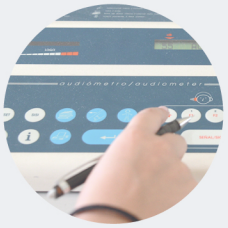


Análise Biomecânica de Calo Ósseo usando Método Sem Malha

ANDREIA FILIPA FERNANDES OLIVEIRA
novembro de 2021

P.PORTO

isep Instituto Superior de Engenharia do Porto

Instituto Superior de Engenharia do Porto ⊙ Rua Dr. António Bernardino de Almeida, 431 ⊙ 4249-015 Porto
Tel. +351 228 340 500 ⊙ Fax +351 228 321 159 ⊙ mail@isep.ipp.pt ⊙ www.isep.ipp.pt

INSTITUTO SUPERIOR DE ENGENHARIA DO PORTO

isep

The Biomechanical Analysis of Bone Callus using a Meshless Method

ANDREIA FILIPA FERNANDES OLIVEIRA
Novembro de 2021

INSTITUTO SUPERIOR DE ENGENHARIA DO PORTO

MESTRADO EM ENGENHARIA BIOMÉDICA

isep

The Biomechanical Analysis of Bone Callus using a Meshless Method

ANDREIA FILIPA FERNANDES OLIVEIRA
Novembro de 2021

P.PORTO

The Biomechanical Analysis of Bone Callus using a Meshless Method

Andreia Filipa Fernandes Oliveira

Biomedical Engineer by School of Engineering, Polytechnic of Porto

"Dissertation carried out at the School of Engineering, Polytechnic of Porto, to obtain a Master's degree in Biomedical Engineering"

Supervisor: Prof. Dr. Jorge Américo Oliveira Pinto Belinha

Co-Supervisor: Prof. Madalena Macedo Alves Peyroteo Gomes

November 2021

“Live as if you were to die tomorrow. Learn as if you were to live forever.”

Mohandas K. Gandhi

Agradecimentos

Como em tudo na vida e nos caminhos que escolhemos percorrer, nada é mais importante do que as pessoas que nos acompanham e apoiam em tudo.

Desta forma, em primeiro lugar gostaria sinceramente de agradecer ao Professor Jorge Belinha, por todo o acompanhamento, disponibilidade e dedicação constantes. Obrigada pela sua boa disposição e oportunidade dada. Gostaria também de agradecer à Professora Madalena Peyroteo pelo seu apoio e disponibilidade.

Agradeço aos meus queridos pais, pelo espírito de sacrifício e por me proporcionarem as melhores condições para os meus estudos e por sempre me motivarem a ser a minha melhor versão. Aos meus avós por serem os exemplos mais bonitos que poderia ter.

Um especial obrigado aos meus amigos, em particular à Isabel, Ana e Francisca pela compreensão, presença constante e motivação. À Mariana e à Nelma agradeço-lhes o apoio neste percurso académico e pela partilha de sorrisos nos momentos mais difíceis.

Resumo

O osso é um tecido fisiologicamente dinâmico e que quando lesionado tem a capacidade de se reparar com o próprio tecido, não envolvendo um tecido cicatrizante, ao contrário de outros tecidos. Esta característica torna-o particularmente interessante para investigar os processos inerentes de fraturas ósseas. A maior parte das fraturas cicatriza através de uma sequência de processos de diferenciação de tecidos, desde os processos iniciais de hematoma, aos tecidos conjuntivos, e através da cartilagem ao osso. No entanto, qualquer falha neste processo pode resultar em uniões tardias, más uniões ou não uniões. A compreensão na totalidade deste processo ainda constitui um desafio. Os mecanismos que envolvem os processos de estimulação mecânica não se encontram bem compreendidos, em consequência da complexidade dos testes experimentais *in vivo*, que se tornam dependentes de dados *in vitro*, tornando difícil validar os pressupostos biológicos. Consequentemente, os modelos computacionais têm demonstrado serem bastante úteis e eficazes na investigação sobre a cicatrização óssea.

Desta forma, com o presente trabalho foi possível analisar as condições mecânicas de um calo ósseo resultante de uma fratura, assim como compreender as metodologias de análise numérica aplicadas. O modelo teve por base um estudo *in vivo* de forma a obter uma variação temporal progressiva da forma do calo e das propriedades mecânicas durante a cicatrização óssea. Com este modelo obtiveram-se os campos de tensão e deformação nas diferentes fases do processo de regeneração, obtendo-se resultados que se encontram em conformidade com a literatura. Adicionalmente, foi aplicado um algoritmo de remodelação óssea em combinação com o Radial Point Interpolation Method (RPIM) que foi capaz de reproduzir as condições apresentadas pela respetiva imagem histológica nesta fase.

Por último, espera-se que os trabalhos desenvolvidos neste âmbito possibilitem a conceção de estratégias mais precisas e eficazes tanto para o tratamento como para aceleração da cura. De forma complementar, encontram-se em desenvolvimento modelos específicos dos pacientes e que incorporam variabilidade genética.

Palavras-chave: cicatrização da fratura óssea; calo ósseo; métodos numéricos; mecanobiologia; biomecânica.

Abstract

Bone is a physiologically dynamic tissue that, when injured, has the ability to repair itself, not involving scar tissue, unlike other tissues. This characteristic makes it particularly interesting for investigating the inherent processes of bone fractures. Most fractures heal through a sequence of tissue differentiation processes, from the initial hematoma, to connective tissues and through cartilage to bone. However, any failure in this process can result in a delayed union, mal-union or non-union. A complete understanding of this process is still a challenge. The mechanisms surrounding the mechanical stimulation processes are relatively poorly understood as a result of the complexity of *in vivo* experimental tests, which become dependent on *in vitro* data, making it difficult to validate the biological assumptions. Consequently, computational models have proven to be very useful and effective in the investigation of bone healing.

Therefore, in the present work, it was possible to analyse the mechanical conditions of a bone callus as a consequence of a fracture and to understand the methodologies of numerical analysis applied. The model was based on an *in vivo* experimental study in order to obtain a progressive temporal variation of the callus shape and mechanical properties during bone healing. With this model, the stress and strain fields in the different phases of the regeneration process were obtained, where the results are in agreement with the literature. Additionally, a bone remodelling algorithm was applied in combination with the Radial Point Interpolation Method (RPIM), which was able to reproduce the conditions presented by the respective histological image at this stage.

Finally, it is expected that the work developed in this area will enable the design of more accurate and effective strategies for both treatment and accelerating healing. Complementarily, patient-specific models and the incorporation of genetic variability are being developed.

Keywords: bone fracture healing; bone callus; numerical methods; mechanobiology; biomechanics.

Index

List of Figures

List of Tables

List of Abbreviations

ECM – Extracellular Matrix

MSC – Mesenchymal Stem Cell

BMU – Basic Multicellular Unit

RANKL – Receptor Activator of Nuclear Factor κB Ligand

CSF-1 – Colony Stimulating Factor 1

OPG – Osteoprotegerin

PTH – Parathyroid Hormone

TGF-β – Transforming Growth Factor-β

TNF-α – Tumour Necrosis Factor-α

PMN – Polymorphonuclear Neutrophil

BMP – Bone Morphogenetic Protein

FEMAS – Finite Element and Meshless Method Analysis Software

FEMAP – Finite Element Modelling And Post-processing software

RPIM – Radial Point Interpolation Method

RBF – Radial Basis Function

RPI – Radial Point Interpolators

SED – Strain Energy Density

SPH – Smooth Particle Hydrodynamics

CHAPTER 1 – INTRODUCTION

1. Introduction

Biomedical engineering encompasses careers and research projects that integrate biological processes in order to develop innovative approaches with application in prevention, diagnosis and therapy. The evolution of computational power, methodologies and the combination of high-resolution medical imaging, made it possible to evaluate a wide variety of biological processes that include the repair and healing of fractured bone.

Bone healing involves a complex and, at the same time, astonishing biomechanical process, which unlike other tissues does not require the production of scar tissue. Instead, new bone is formed and continuously remodelled until the original site of injury is not recognised. Bone fracture healing involves cell differentiation and tissue remodelling, both of which are influenced by the mechanical environment [1].

The approaches adopted by researchers usually require the union of experimental and theoretical methods by applying the theory to understand the experimental data or the data to demonstrate the theory. However, these are limited due to the complexity of bone fracture healing. Therefore, computational numerical simulation has emerged as a widely promising tool, constituting a dynamic simulation that can be used in order to explore and establish an understanding of the problem, where there is greater control of the interactions between the system's constituents. Thus, these computational models are developed in biomechanics in order to aid the understanding of biological phenomena, mainly time-dependent ones such as bone healing.

In this chapter the motivation and objectives are presented, as well as the outline of this document.

1.1. Motivation

Fractures are one of the most frequent injuries of the musculoskeletal system and the most common form of hospitalised trauma. Despite the extensive amount of research conducted, as well as the fact that treatment of fractures has improved considerably in recent decades, a large proportion of all fractures, up to 5-10%, still show delayed union, mal-union and non-union associated with some risk factors such as soft tissue injury, extensive bone loss, fracture instability, infection, and a poor general medical condition of the patient [2]. All these aspects contribute not only to considerable individual

disability and consequent loss of productivity but also to a reduction in quality of life and significant treatment costs [3]. In this regard, a detailed understanding of the biomechanical aspects of the bone healing process is essential for orthopaedic surgeons to create an optimal healing environment in the fractured limb [4].

The study of the bone healing process comprises two general approaches, experimental methods and computational modelling. Experimental studies in humans and animals provide detailed knowledge of the processes that occur during the bone healing response, such as: the influence of fixation stability, ageing, fracture size, etc. (tissue level); determination of the contribution of different cell phenotypes (cellular level) and, finally, investigation of intracellular signalling pathways for therapeutic application in bone regeneration (intracellular level) [5]–[9]. However, experimental approaches are unable to fully describe the underlying biochemical and biomechanical mechanisms leading to fracture healing and, therefore, understanding the process as a whole is still challenging [4].

Consequently, computer models have emerged to aid the investigation of bone regeneration and remodelling. These models have become increasingly complex, including more biological processes in order to understand the mechanical and biological interactions that lead to the different phases of bone healing. In general, the Finite Element Method (FEM) is one of the most widely applied methodologies in computational models. However, alternatively, to this method, meshless methods such as the Radial Point Interpolation Method (RPIM) have emerged, which have proven to be advantageous compared to mesh-based methods [10].

The main advantage of these simulation methodologies comes from the fact that they can predict the outcome of bone healing and how it might be influenced. Additionally, they are used in understanding the underlying mechanisms of the bone healing response. Ultimately, when the mechanisms of mechanically-regulated tissue formation are well defined, then physiological conditions and pharmacological agents can be developed and utilized to prevent non-unions and, furthermore, to promote and help accelerate fracture repair and restore optimal function.

1.2. Objectives

The main objective of this project is to develop a new mechanical model to predict bone callus formation as a consequence of a fracture.

To achieve this objective, several secondary objectives were defined:

- Understand the influence of stress and strain in tissues during bone healing phenomenon;
- Develop 2D and 3D tibial models and include transverse fractures;
- Analysis of the transverse fracture models in order to simulate the complete regeneration process and validation.
- Analysis of bone callus remodelling in the presence of a mechanical stimulus and validation.

1.3. Document Structure

This document is organized into seven chapters, starting with Chapter 1, which presents the theme under study and the main objectives of the work. Chapter 2 describes the bone tissue morphology, composition, structure and mechanical properties, and, lastly, bone formation. Chapter 3 focuses on the biological processes of bone growth and remodelling and also on bone fracture healing, ending with the bone callus mechanical properties. Then, Chapter 4 encompasses the numerical methods used in this work, describing their formulation, followed by an introduction of basic notions of solid mechanics. Chapter 5 corresponds to the state of the art of mechanobiological models that simulate bone callus. Afterwards, in Chapter 6, the numerical work performed is presented, with the computational models created, as well as the results obtained both in the analysis of the bone healing process over time and in the remodelling analysis. To finish, in Chapter 7, the main achievements of the work are outlined along with some limitations and suggestions for future improvements.

CHAPTER 2 - BONE TISSUE

2. Bone Tissue

Bone is a remarkably strong and lightweight material, being the hardest living tissue among other connective tissues in the body. Bone exerts important functions, such as: providing a stiff skeleton on which the muscles act to produce locomotion and other physical activities; protecting vital organs, such as the heart and lungs, which are protected within the rib cage, and the brain within the skull; storing calcium and phosphate ions, which are necessary for physiological function; and finally, harbouring of bone marrow [11], [12].

Bone consists of 50% water and the remaining solid part contains various minerals, especially 70% calcium salt and 30% cellular material [13]. Therefore, the extracellular matrix is a complex composite with organic and inorganic components. Most of the organic part is composed of collagen, a natural polymer, and the inorganic is mainly a mineral chemically and crystallographically similar to hydroxyapatite, $Ca_{10}(P0_4)_6(OH)_2$. The mineral component gives strength and stiffness to the tissue, while the collagen phase is ductile, giving bone its toughness [14]. Bone collagen is mainly type I collagen and has the same general composition and chemical structure as other type I collagens however, it differs in its mechanical and physicochemical properties. The third main component of bone is water. Wet bone and dry bone exhibit very different mechanical responses and, therefore, the importance of water for the mechanical functioning of bone cannot be underestimated [15], [16].

Bone has vascular tissue and cellular activity products, especially during growth which is very dependent on the blood supply as a basic source and hormones that greatly regulate this growth process. It is also a highly dynamic structure undergoing constant remodelling, being removed and replaced by two species of bone cells, osteoclasts and osteoblasts respectively, which are found on the free surfaces of bone. These cell species play an essential role in determining bone growth, the thickness of the cortical layer and the structural arrangement of the lamellae. Bone reacts to its mechanical environment by increasing or decreasing the amount of material present depending on the stress regime. This relationship between bone mechanical environment and bone internal and external structure was first described by J. Wolff [17]. Also, it continuously renews itself, removing old or damaged bone and replacing it with new material. As a consequence of the effects of gravity and compressive loads produced by muscle action, the stresses in

bone are usually compressive, although some tensile loading is seen in certain regions of the body and during specific activities.

2.1. Bone Morphology

The skeletal system is the body system composed of bones, cartilages, ligaments and other tissues that perform essential functions for the human body. The adult human skeleton consists of 206 bones. Bones can be categorized into five types, i.e., long, short, flat, sesamoid and irregular [18]. Long bones include the femur, tibia, fibula, humeri, radii, ulna, metacarpals, metatarsals, phalanges, clavicles, which provide skeletal mobility and are subject to the most of the load during everyday activities [18].

The shafts of the long bones are referred to as the diaphysis and the expanded ends as the epiphyses. Inside the diaphysis is the medullary cavity, which is filled with yellow bone marrow in an adult, consisting mostly of adipose tissue. The outer walls of the diaphysis (cortex, cortical bone) are composed of dense and hard compact bone. The epiphysis is filled internally with trabecular bone. Red bone marrow fills the spaces between the trabecular bone in some long bones and is composed of blood-forming cells, being the only site of blood formation in adults. Children's bones have proportionally more red bone marrow than adults due to ageing the red bone marrow is mostly replaced by the yellow bone marrow. Each epiphysis meets the diaphysis at the metaphysis. During growth, the metaphysis contains the epiphyseal plate, the site of long bone elongation. When the bone stops growing in early adulthood (approximately 18–21 years), the epiphyseal plate becomes an epiphyseal line (Figure 2.1).

The interior of the bone adjacent to the medullary cavity is lined with a layer of bone cells forming a thinner connective tissue membrane, the endosteum. These bone cells promote the growth, repair and remodelling of bone throughout life (Figure 2.2).

Most of the external surface of the bone is covered by dense connective tissue called the periosteum, also composed of a layer of cells that grow, repair, and remodel the bone. It consists of two layers and contains blood vessels, nerves and lymphatic vessels that nourish compact bone. In the periosteum tendons and ligaments are attached to the bones. It covers the entire outer surface except where the epiphyses meet with other bones to form joints (Figure 2.2), at this site the epiphyses are covered with articular cartilage, which constitutes a thin layer of hyaline cartilage that reduces friction and acts as a shock absorber.

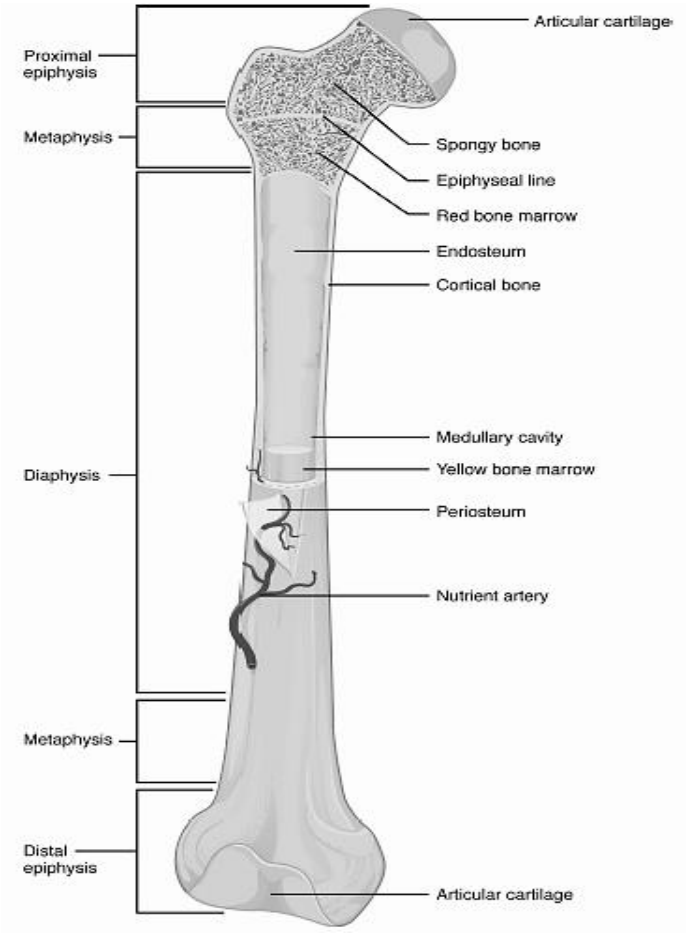

Figure 2.1- Anatomy of a long bone. Adapted from [19].

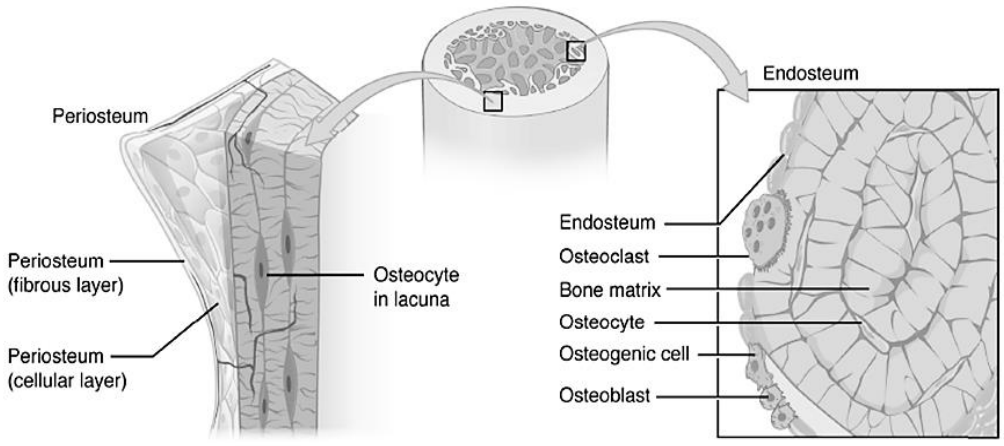

Figure 2.2- The periosteum forms the outer surface of the bone, and the endosteum lines the medullary cavity. Adapted from [19].

2.2. Bone Composition and Structure

2.2.1. Bone Matrix

Bone tissue is connective tissue and consequently contains relatively few cells and large amounts of extracellular matrix (ECM). Concerning the bone body dry weight, the ECM is divided into organic and inorganic components. By mass, the bone tissue matrix consists of 30% collagen fibres (primarily of type I collagen) and 70% calcium phosphate salt [13]. The collagen provides a scaffolding surface for inorganic salt crystals to adhere. These salt crystals form when calcium phosphate and calcium carbonate combine to create carbonate-rich hydroxyapatite, also called bone apatite, which is smaller and less perfect in crystal arrangement than pure hydroxyapatite, $Ca_{10}(P0_4)_6(OH)_2$ [13]. Other inorganic salts are also present in the bone mineral matrix like sodium, magnesium, potassium, fluoride and chloride. The hydroxyapatite crystals give bones their hardness, stiffness and high ultimate compression stress. The collagen fibres (according to the orientation and the quantity of these fibres) confer a framework for calcification and give the bone elasticity and high ultimate traction and shear stress. The remainder of the skeleton consists of cells and blood vessels.

The bone matrix constitutes a complex and organized framework that provides mechanical support and exerts an essential role in bone homeostasis. The bone matrix can release several molecules that interfere in the bone cells activity and, consequently, has a participation in the bone remodelling. Once the loss of bone mass alone is insufficient to cause bone fractures [20], it is suggested that other factors, including changes in the bone matrix proteins and their modifications, are of crucial importance to the understanding and prediction of bone fractures [21]. It is known that collagen plays a critical role in the structure and function of bone tissue [22]. Accordingly, it has been demonstrated that there is a variation in the concentration of bone matrix proteins with age, nutrition, disease, and antiosteoporotic treatments [21], [23], [24] which may contribute to post-yield deformation and fracture of the bone.

2.2.2. Bone Cells

Even though bone cells constitute less than 2% of bone mass, they are essential for bone function. Therefore, five types of cells are found within bone tissue: osteogenic

(osteoprogenitor) cells, bone-lining cells, osteoblasts, osteocytes, and osteoclasts (Figure 2.3) [25].

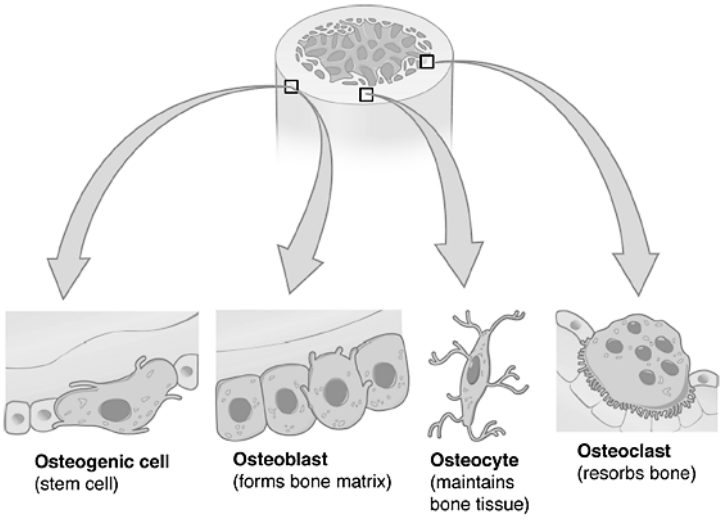

Figure 2.3- Development of bone precursor cells. Bone precursor cells are divided into developmental stages, which are: osteogenic cell (osteoprogenitor); bone-lining cell (pre-osteoblast); osteoblast; osteocyte, and osteoclast. Adapted from [19].

The osteogenic (osteoprogenitor) cells are undifferentiated with high mitotic activity and they are the only bone cells that divide. Immature osteogenic cells are found in the cellular layer of the periosteum, endosteum and the Haversian's and Volkmann's canals. They differentiate and develop into osteoblasts. These cells are involved in the formation of all bone structures during the growth process and are generated in the bone marrow, or other connective tissues [25].

Osteoblasts are cuboidal cells responsible for forming new bone and are found in the growing portions of bone, including the endosteum and the cellular layer of the periosteum (comprising 4–6% of the total resident bone cells) [25]. Osteoblasts are derived from mesenchymal stem cells (MSC) and present morphological characteristics of protein-synthesizing cells and secrete the collagen matrix and other proteins [25]. With the calcification of the secreted matrix involving the osteoblasts, they get trapped in matrix-bound lacunae and as a result, they change the structure and become osteocytes, the primary cell of mature bone and the most common type of bone cell (90-95% of the total bone cells).

The morphology of osteocytes differs depending on the type of bone, where the osteocytes from trabecular bone are more rounded than the osteocytes from cortical bone,

which exhibit an elongated morphology [26]. Osteocytes are derived from the MSC lineage through osteoblasts differentiation. They maintain the mineral concentration of the matrix through the secretion of enzymes. While sharing most matrixes related to osteoblast activities, osteocytes also express many different proteins, including paracrine and endocrine factors that help regulate bone remodelling. Osteocytes communicate with each other and receive nutrients via long cytoplasmic processes that extend through thin canals within the bone matrix, called canaliculi, and are connected within the canaliculi through gap junctions. These connections between osteocyte processes and nearly all other bone cells in the extensive lacunar-canalicular network allow osteocytes to serve as mechanosensors detecting the mechanical load on the bone as well as stress- or fatigue-induced microdamage and to trigger remedial activity in osteoblasts and osteoclasts.

Bone-lining cells, also called pre-osteoblasts, are inactive elongated and thin osteoblasts found in the periosteal and endosteal surfaces, where neither bone resorption nor bone formation occurs [25]. Once the bone formation or the bone remodelling has finished, these cells remain inactive in the bone surface but can be reactivated in response to mechanical or/and chemical stimulation [27].

The dynamic nature of bone means that new tissue is constantly formed, and old, injured, or unnecessary bone is dissolved for repair or calcium release. The cells responsible for bone reabsorption and/or elimination are the osteoclasts. These multinucleated cells originate from monocytes and macrophages, two types of white blood cells (hematopoietic stem cell lineage). Osteoclasts are continually breaking down old bone while osteoblasts are continually forming new bone. The ongoing balance between osteoblasts and osteoclasts is responsible for the constant but subtle reshaping of bone.

2.2.3. Bone Tissue Hierarchy

The various levels of hierarchical structural organization of bone are [28]: (1) the macrostructure: trabecular and cortical bone; (2) the microstructure: osteons or Haversian and trabeculae systems (10–500 μm); (3) the sub-microstructure: mineralised lamellae and collagen fibres (1–10 μm); (4) the nanostructure: mineralised collagen fibrils (about 100 nm–1 μm), and (5) the sub-nanostructure: molecular and atomic structure of main components (<100 nm) (Figure 2.4). This hierarchically organized structure has an

irregular, yet optimized, arrangement and orientation of the components, making the material of bone heterogeneous and anisotropic.

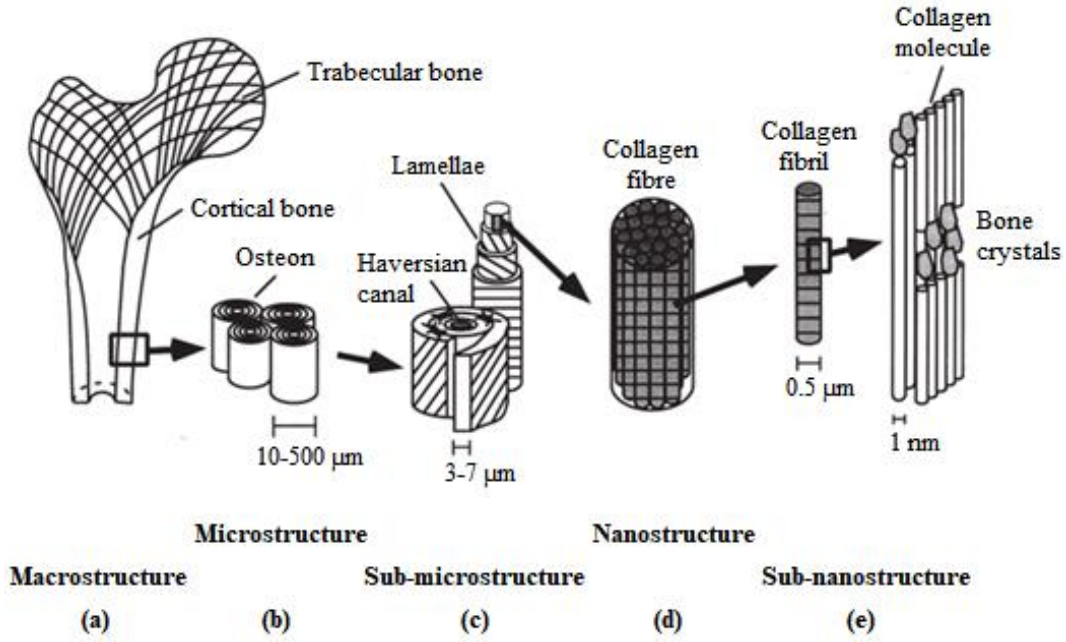

Figure 2.4- Hierarchical structural organization of bone: (a) cortical and trabecular bone; (b) osteons with Haversian systems; (c) lamellae; (d) collagen fibre assemblies of collagen fibrils; (e) bone mineral crystals, collagen molecules, and non-collagenous proteins. Adapted from [29].

2.2.3.1. Cortical and Trabecular Bone

At the macrostructure level, bone is distinguished into the cortical (or compact) and trabecular (or cancellous, spongy) types. In cross-section, the end of a long bone such as the femur has a dense cortical shell with a porous, trabecular interior. Although both types of bone (cortical and trabecular) are most easily distinguished by their degree of porosity or density, true differentiation comes from a histological evaluation of the tissue's microstructure. The microstructure of cortical bone is composed of regular, cylindrically shaped lamellae. In contrast, the microstructure produced by the compaction of trabecular bone is composed of irregular, sinuous convolutions of lamellae. Therefore, reliable differentiation can only be achieved by microscopy methods.

In general, trabecular bone is much more active metabolically, being remodelled more frequently than cortical bone, and is, therefore, younger on average than cortical bone [30]. In fact, every year 25% of trabecular bone is replaced compared to only 2–3% of cortical bone. Cortical bone makes up 80% of the human skeleton; the remainder is

trabecular bone, which has a spongelike appearance with numerous large spaces and is found in the marrow space (medullary cavity) of a bone [31].

The cortical bone microstructure consists of Haversian systems also known as osteons (Figure 2.5).

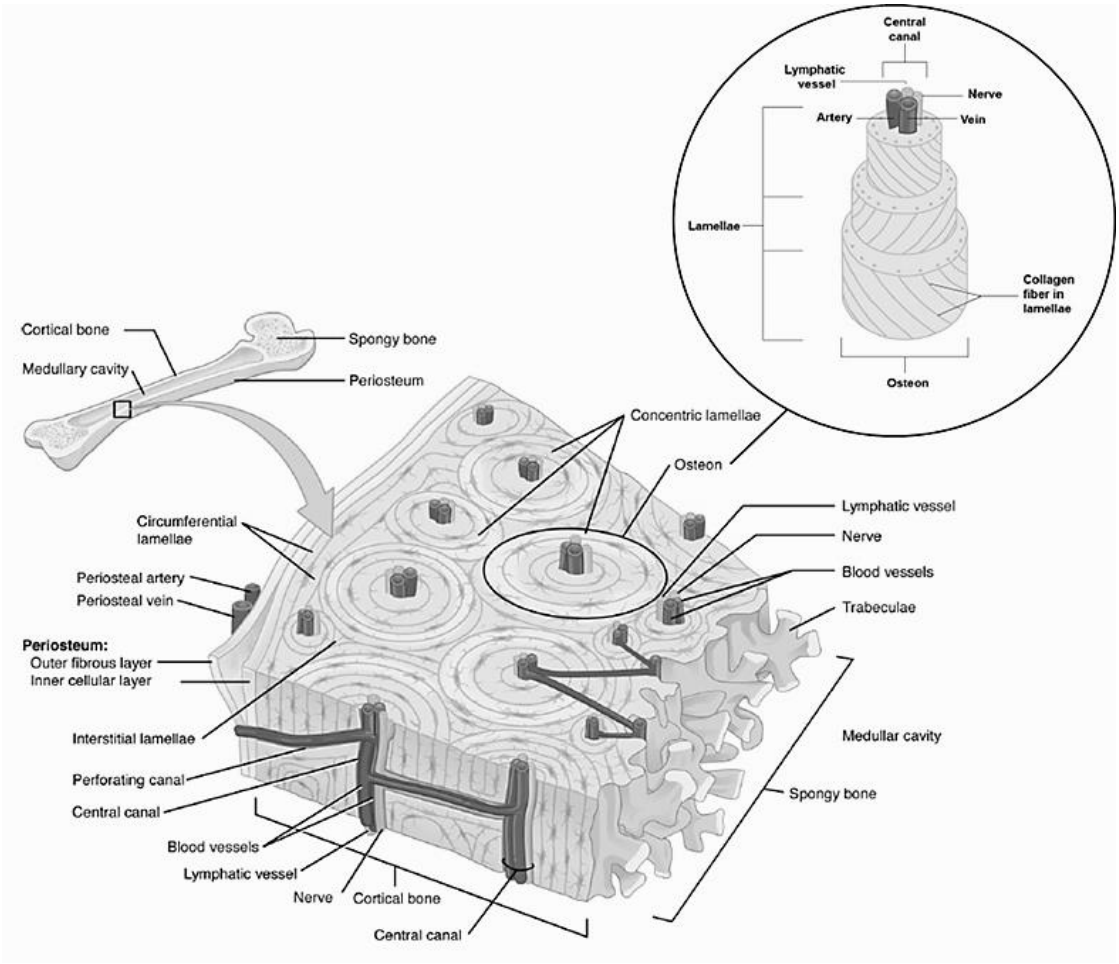

Figure 2.5- Cortical (or compact) bone. A cross-sectional view of cortical bone showing several osteons, the basic structural unit. Adapted from [19].

Osteons are circular or oval in cross-section, 20–110 μm in diameter and contain central blood vessels, in a cylindrical canal known as a Haversian canal and are typically 2–3 mm long. The blood vessels are surrounded by three to eight concentrically arranged lamellae which are each 3–7 mm thick. Osteons generally run parallel to the long axis of the bone or the major loading direction, though they give off branches, Volkmann canals, which join adjacent Haversian canals. Between the individual lamellae are small spaces called lacunae and each contains a cell called an osteocyte. They are arranged

circumferentially around the central canal and the lacunae are interconnected by fine canaliculi containing osteocyte processes, which connect to adjacent osteocytes to allow osteocyte to osteocyte communication. The Haversian canals are organised to accommodate the small blood vessels of the microcirculation and are generally formed as part of a microvascular network. Nutrients and oxygen cannot diffuse easily through the calcified matrix. Instead, the branching canaliculi provide routes for nutrients and oxygen to reach the osteocytes and for the waste products of metabolism to diffuse away [32].

In contrast to the compact bone, the trabecular bone contains osteocytes housed in lacunae, but they are not arranged in concentric circles. Instead, the lacunae and osteocytes are found in a lattice-like network of matrix spikes called trabeculae (Figure 2.6). The trabeculae are covered by the endosteum, which can readily remodel them. The trabeculae may appear to be a random network, but each trabecula forms along lines of stress to direct forces out to the more solid compact bone providing strength to the bone. Trabecular bone provides balance to the dense and heavy compact bone by making bones lighter so that muscles can move them more easily [19].

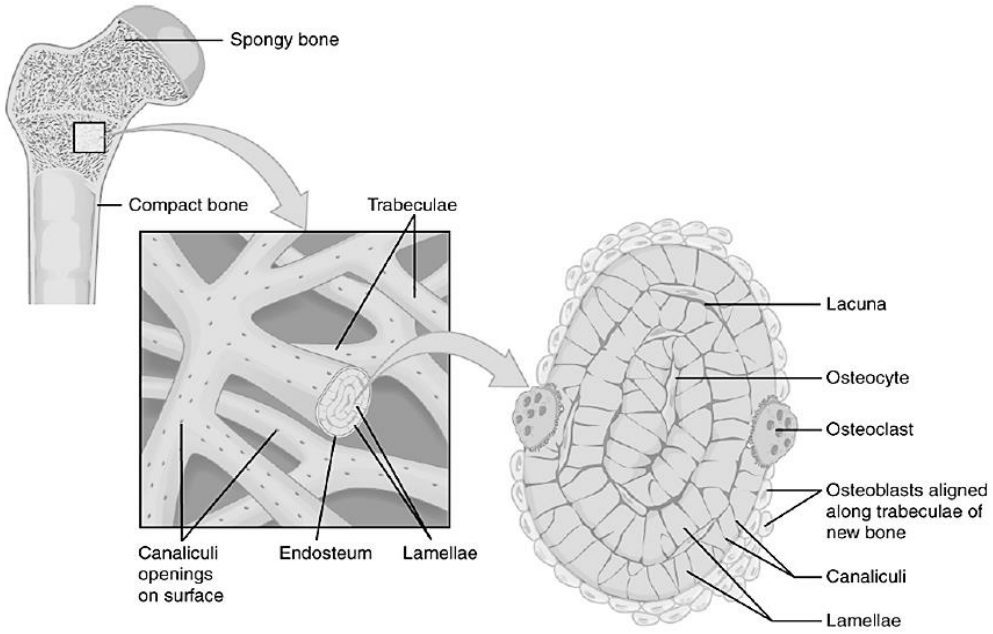

Figure 2.6- Trabecular (or cancellous, spongy) bone. Trabecular bone is composed of trabeculae that contain osteocytes. Red marrow fills the spaces in some bones [19].

Trabecular bone is structurally inhomogeneous at various levels, from sub-microscopic to macroscopic, making it mechanically heterogenous and anisotropic; however, trabecular bone behaves like any other porous structure with the tensile and compressive strengths being proportional to apparent density squared [19].

2.3. Bone Tissue Mechanical Properties

The mechanical properties of bone tissue have been a topic widely addressed and discussed by several researchers over time. As mentioned above, bone tissue can be classified as cortical bone and trabecular bone. The distinction between cortical and trabecular bone can be made based on porosity (directly related to bone density). The cortical bone presents a porosity, p, lower than around 30% [33]. The porosity of adult human femoral cortical bone can vary from 5% at age 20 up to almost 30% above age 80 [34]. In contrast, the porosity of trabecular bone can range from 70% in the femoral neck [35] to about 95% in the elderly spine [36].

Additionally, density can be defined in several ways at either the bone tissue or the bone material level. The wet mineralised mass of bone of the sample tissue, w_{sample}, over the volume occupied by the same sample tissue, V_{sample}, defines the value of apparent density, ρ_{app}, (Eq. (2.1)). Whereas the same mass of bone material over the volume occupied by the material itself defines the material density of bone. The two will differ in the presence of pores or the vacuous spaces that are related to canaliculi, osteocyte lacunae, osteonal canals and analogous non-mineralised architectural features. Additionally, there is also a relation that corresponds to the concept of porosity, defined by BV/TV, i.e., the ratio of bone material volume over tissue volume. It represents a geometric and visible marker of the level of porosity in the structure, relating the apparent density value (primary influence of mechanical properties at the tissue/structural level) with the material density (determines material behaviour at the trabecular level and, consequently, properties at the structural level) [37].

$$\rho_{app} = \frac{w_{sample}}{V_{sample}} \qquad \text{Eq. (2.1)}$$

The apparent density depends on the bone porosity, which can be obtained through the following expression,

$$p = \frac{V_{holes}}{V_{sample}} \quad \text{Eq. (2.2)}$$

in which V_{holes} corresponds to the volume of bone holes obtained by the Archimedes principle. Therefore, the apparent density can also be established by applying the porosity,

$$\rho_{app} = \rho_0 \cdot (1 - p) \quad \text{Eq. (2.3)}$$

where ρ_0 is the compact bone density, $\rho_0 = 2.1\ g/cm^3$.

With the increasing knowledge about the mechanical properties of bone tissue, it was possible to move from models that assumed an isotropic bone behaviour to models, based on experimental studies, that consider an orthotropic bone behaviour.

2.3.1. Lotz's Material Law

The work of Lotz et al. [38] was one of the first that considered the bone orthotropic nature. This work involved the determination of the elasticity modulus and the ultimate compression stress mathematical laws for both cortical and trabecular bone in the axial and transverse directions, with the apparent density being the only variable. Thus, the macroscale bone mechanical properties are approximated with the following expressions,

$$E_i = a_1 \cdot (\rho_{app})^{a_2} \quad \text{Eq. (2.4)}$$

$$\sigma_i^c = a_3 \cdot (\rho_{app})^{a_4} \quad \text{Eq. (2.5)}$$

in which E_i and σ_i^c correspond to the elasticity modulus and the ultimate compression stress in direction i, respectively, both expressed in MPa and the apparent density, ρ_{app}, in g/cm^3. The coefficients a_j are presented in Table 2.1 for both cortical and trabecular bone in the axial and transverse directions.

Table 2.1- Coefficients of Lotz's Law.

Bone Tissue	Direction	a_1	a_2	a_3	a_4
Cortical	Axial	2065	3.09	72.4	1.88
	Transversal	2314	1.57	37	1.51
Trabecular	Axial	1904	1.64	40.8	1.89
	Transversal	1157	1.78	21.4	1.37

2.3.2. Belinha's Material Law

An experimental study developed by Zioupos et al. [37], also highlights that density is a property that has a crucial role in determining the mechanical properties of both its trabecular and cortical structural forms. In this work, from the measured apparent density in cubic micropatches, the bone was objectively isolated into trabecular and compact forms. The results show that the relation between apparent density and elasticity modulus is no longer an increasing monotonic function but rather a function with a "boomerang"-like pattern. It was shown that the law governing the mechanical behaviour of bone tissue corresponds to the same for cortical and trabecular bone, as opposed to the two distinct material laws as proposed by Lotz [38]. Thus, based on Zioupos' work [37], Belinha [10] also proposed a law that regulates the mechanical behaviour of bone tissue, as observed in Figure 2.7.

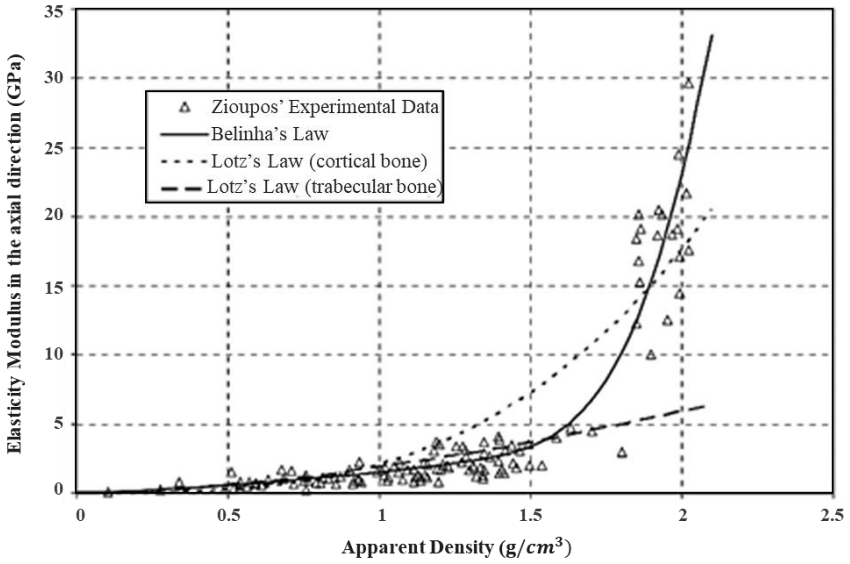

Figure 2.7- Representative graph of the elasticity modulus in the axial direction with the respective comparison between the experimental data obtained in Zioupos' work with Lotz's law for cortical and trabecular bone and with the mathematical model proposed by Belinha.

Belinha's work [10], established a unifying law for cortical and trabecular bone. Zioupos' work only involved the analysis of the bone elasticity modulus in the axial direction [37]. However, Belinha proposed the mathematical curves for the elasticity modulus in the transverse direction and the ultimate compression stress in the axial and transverse directions, based on the values suggested by Lotz [38]. Thus, it was defined a novel anisotropic material law that correlates accurately the bone apparent density with the obtained level of stress by means of a mechanical stimulus [39].

The bone elasticity modulus, E, and the ultimate compression stress, σ^c, for the axial and transverse directions are obtained using the approximation curves of Eq. (2.6), (2.7), (2.8), (2.9) and (2.10).

$$E_{axial} = \begin{cases} \sum_{j=0}^{3} a_j \cdot \rho^j & if \quad \rho \leq 1.3\ g/cm^3 \\ \sum_{j=0}^{3} b_j \cdot \rho^j & if \quad \rho > 1.3\ g/cm^3 \end{cases}$$

Eq. (2.6)

Eq. (2.7)

$$E_{trans} = \sum_{j=0}^{3} c_j \cdot \rho^j \quad \text{Eq. (2.8)}$$

$$\sigma_{axial}^{c} = \sum_{j=0}^{3} d_j \cdot \rho^j \quad \text{Eq. (2.9)}$$

$$\sigma_{trans}^{c} = \sum_{j=0}^{3} e_j \cdot \rho^j \quad \text{Eq. (2.10)}$$

where the coefficients a_j, b_j, c_j, d_j and e_j are given in Table 2.2. The E_i and σ_i^c in direction i are both expressed in MPa and the apparent density, ρ, in g/cm^3.

Table 2.2- Coefficients of Belinha's Law.

Coefficients	$j = 0$	$j = 1$	$j = 2$	$j = 3$
a_j	0.00	721.61	805.86	0.00
b_j	-177044.29	386136.43	-279771.43	68357.14
c_j	0.00	0.00	2003.56	-144.23
d_j	0.00	0.00	26.80	20.35
e_j	0.00	0.00	25.01	1.25

2.4. Bone Formation

In the early stages of embryonic development, the embryo's skeleton consists of fibrous membranes and hyaline cartilage. By the sixth or seventh week of embryonic life, the actual process of bone development, ossification (osteogenesis), begins. There are two osteogenic pathways – intramembranous ossification and endochondral ossification – but in the end, mature bone is the same regardless of the pathway that produces it.

2.4.1. Intramembranous Ossification

During intramembranous ossification, cortical and trabecular bone develops directly from sheets of mesenchymal (undifferentiated) connective tissue. The flat bones of the face, most of the cranial bones, and the clavicles (collarbones) are formed via intramembranous ossification [19].

The process begins when mesenchymal cells in the embryonic skeleton gather together and begin to differentiate into specialized cells (Figure 2.8(a)). Some of these cells will differentiate into capillaries, while others will become osteogenic cells and then osteoblasts. Although they will ultimately be spread out by the formation of bone tissue, early osteoblasts appear in a cluster called an ossification centre [19].

The osteoblasts secrete osteoid, uncalcified matrix consisting of collagen precursors and other organic proteins, which calcifies (hardens) within a few days as mineral salts are deposited on it, thereby entrapping the osteoblasts within. Once entrapped, the osteoblasts become osteocytes (Figure 2.8(b)). As osteoblasts transform into osteocytes, osteogenic cells in the surrounding connective tissue differentiate into new osteoblasts at the edges of the growing bone [19].

Several clusters of osteoid unite around the capillaries to form a trabecular matrix, while osteoblasts on the surface of the newly formed trabecular bone become the cellular layer of the periosteum (Figure 2.8(c)). The periosteum then secretes cortical bone superficial to the trabecular bone. The trabecular bone crowds nearby blood vessels, which eventually condense into red bone marrow (Figure 2.8(d)). The new bone is constantly also remodelling under the action of osteoclasts [19].

Intramembranous ossification begins in utero during fetal development and continues on into adolescence. At birth, the skull and clavicles are not fully ossified nor are the junctions between the skull bone (sutures) closed. This allows the skull and shoulders to deform during passage through the birth canal. The last bones to ossify via intramembranous ossification are the flat bones of the face, which reach their adult size at the end of the adolescent growth spurt [19].

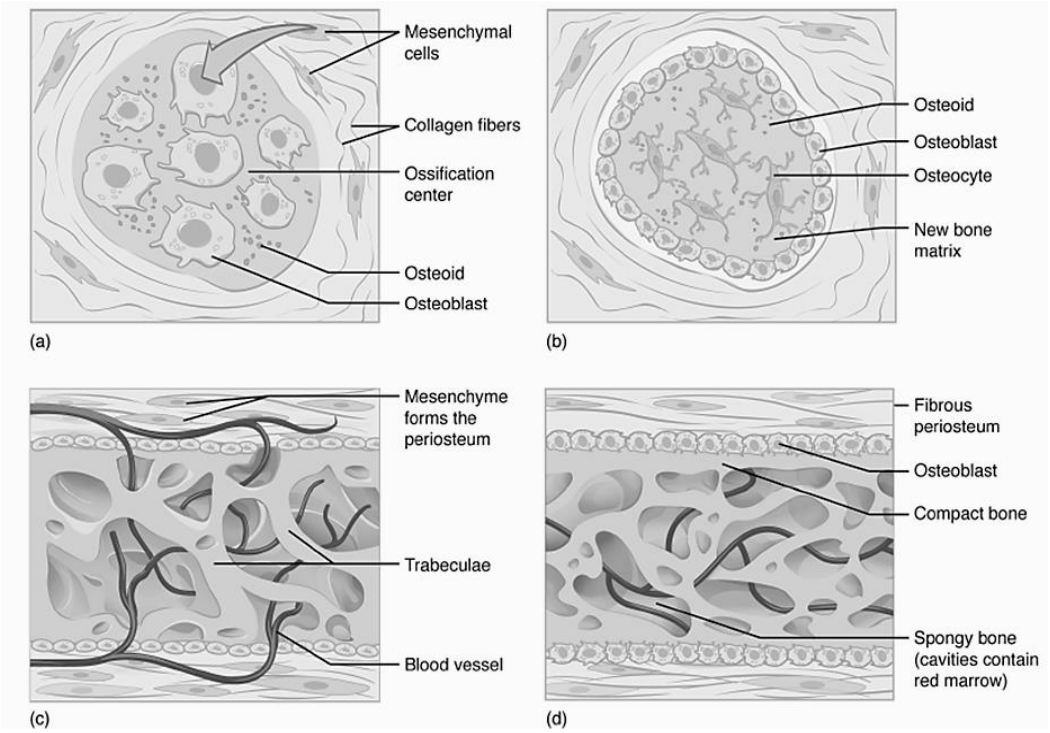

Figure 2.8- Intramembranous Ossification. (a) Mesenchymal cells group into clusters, differentiate into osteoblasts, and ossification centres form. (b) Secreted osteoid traps osteoblasts, which then become osteocytes. (c) Trabecular matrix and periosteum form. (d) Cortical (or compact) bone develops superficial to the trabecular bone, and crowded blood vessels condense into red bone marrow [19].

2.4.2. Endochondral Ossification

In endochondral ossification, bone develops by replacing hyaline cartilage. Cartilage does not become bone. Instead, cartilage serves as a template to be completely replaced by new bone. Endochondral ossification takes much longer than intramembranous ossification. Bones at the base of the skull and long bones form via endochondral ossification.

In a long bone, for example, at about six to eight weeks after conception, some of the mesenchymal cells differentiate into chondroblasts (cartilage cells) that form the hyaline cartilaginous skeletal precursor of the bones (Figure 2.9(a)). This cartilage is a flexible, semi-solid matrix produced by chondroblasts and consists of hyaluronic acid, chondroitin sulphate, collagen fibres, and water. As the matrix surrounds and isolates chondroblasts, they are called chondrocytes. Unlike most connective tissues, cartilage is avascular, meaning that it has no blood vessels supplying nutrients and removing

metabolic wastes. All of these functions are carried on by diffusion through the matrix from vessels in the surrounding perichondrium, a membrane that covers the cartilage [19].

As more and more matrix is produced, the cartilaginous model grows in size. Blood vessels in the perichondrium bring osteoblasts to the edges of the structure and these arriving osteoblasts deposit bone in a ring around the diaphysis – this is called a bone collar (Figure 2.9(b)). The bony edges of the developing structure prevent nutrients from diffusing into the centre of the hyaline cartilage [19], [40].

This results in chondrocyte death and disintegration in the centre of the structure. Without cartilage inhibiting blood vessel invasion, blood vessels penetrate the resulting spaces, not only enlarging the cavities but also carrying osteogenic cells with them, many of which will become osteoblasts. These enlarging spaces eventually combine to become the medullary cavity. Bone is now deposited within the structure creating the primary ossification centre (Figure 2.9(c)) [19], [40].

While these deep changes are occurring, chondrocytes and cartilage continue to grow at the ends of the structure (the future epiphyses), which increases the structure's length at the same time bone is replacing cartilage in the diaphysis. This continued growth is accompanied by remodelling inside the medullary cavity (osteoclasts were also brought with invading blood vessels) and overall lengthening of the structure (Figure 2.9(d)). By the time, the fetal skeleton is fully formed, cartilage remains at the epiphyses and at the joint surface as articular cartilage [19], [40].

After birth, this same sequence of events (matrix mineralization, death of chondrocytes, invasion of blood vessels from the periosteum, and seeding with osteogenic cells that become osteoblasts) occurs in the epiphyseal regions, and each of these centres of activity is referred to as a secondary ossification centre (Figure 2.9(e)). Throughout childhood and adolescence, there remains a thin plate of hyaline cartilage between the diaphysis and epiphysis known as the growth or epiphyseal plate (Figure 2.9(f)). Eventually, this hyaline cartilage will be removed and replaced by bone to become the epiphyseal line [19], [40].

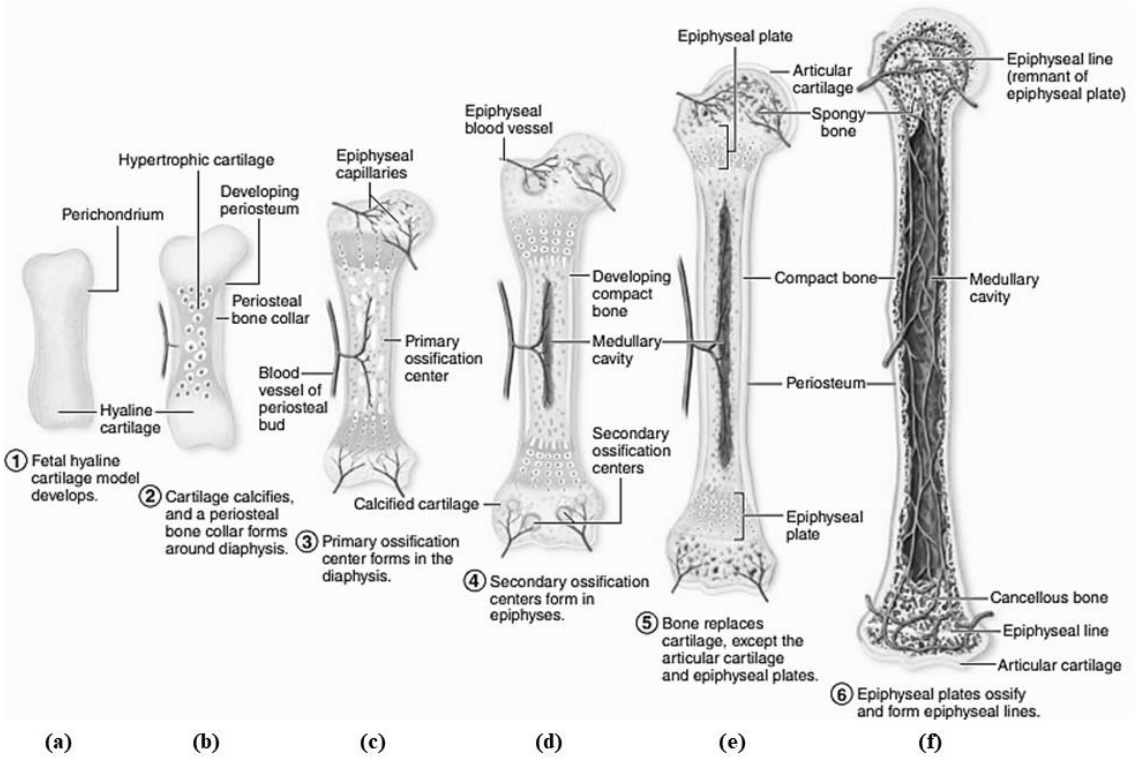

Figure 2.9- Endochondral Ossification. (a) Mesenchymal cells differentiate into chondrocytes that produce a cartilage model of the future bony skeleton. (b) Blood vessels on the edge of the cartilage model bring osteoblasts that deposit a bony collar. (c) Capillaries penetrate cartilage and deposit bone inside cartilage model, forming primary ossification centre. (d) Cartilage and chondrocytes continue to grow at ends of the bone while medullary cavity expands and remodels. (e) Secondary ossification centres develop after birth. (f) Hyaline cartilage remains at epiphyseal (growth) plate and at joint surface as articular cartilage. Adapted from [40].

CHAPTER 3 – GROWTH AND REMODELLING OF BONE TISSUE

3. Growth and Remodelling of Bone Tissue

In order to understand tissue regeneration, it is important to describe similar biological processes, such as embryogenesis and skeletal growth. During the third month of intra-uterine life, the development of cartilage bone height occurs. However, due to the small size of the embryo, it consists of a chondroskeleton without an internal blood supply. In the fourth month, vascular elements develop, allowing the cartilage to grow and be replaced by bone. Thus, bone growth encompasses interstitial epiphyseal growth (oppositional) characterized by the production of long bones as the cartilage elongates and is replaced by bone tissue, until adolescence. This process consists of bone formation and resorption. On the other hand, it will also include appositional growth, which occurs when new bone tissue is deposited on the surface of the bone, resulting in bone thickening, which is usually the only one found in healthy adults.

After the moment skeletal maturity is reached, bone undergoes successive resorption and is replaced by new bone in a process known as bone remodelling. Both bone growth and remodelling can be affected by multiple cell types and signalling pathways, such as: chondrocytes and osteoblasts derived from bone marrow mesenchymal stem cells, osteoclasts of haematopoietic origins, and hormones and other neuromodulators that assist in regulating the balance of osteoblastic bone formation and osteoclastic bone resorption.

3.1. Bone Growth

3.1.1. Oppositional Growth

Growth in the length of a bone, which is the major source of increased height in an individual, occurs in the epiphyseal plate. This process is called oppositional growth. It includes a layer of hyaline cartilage where ossification can continue to occur in immature bones. On the epiphyseal side of the epiphyseal plate, hyaline cartilage cells are active and are dividing and producing hyaline cartilage matrix (reserve and proliferative zones) [13]. On the diaphyseal side of the growth plate, cartilage calcifies and dies, then is replaced by bone (zones of hypertrophy and maturation, calcification and ossification) [13]. As cartilage grows, the entire structure grows in length and then is turned into bone. Once cartilage cannot grow further, the structure cannot elongate more.

The epiphyseal plate is composed of five zones of cells and activity (Figure 3.1). The reserve zone is the region closest to the epiphyseal end of the plate and contains small chondrocytes within the matrix. Chondrocytes increase in number on the epiphyseal side of the epiphyseal plate. They line up in columns parallel to the long axis of the bone, causing the bone to elongate. Then the chondrocytes enlarge and die. The proliferative zone is the next layer toward the diaphysis and contains stacks of slightly larger chondrocytes. It makes new chondrocytes (via mitosis) to replace those that die at the diaphyseal end of the plate. Chondrocytes in the next layer, the zone of maturation and hypertrophy, are older and larger than those in the proliferative zone. The more mature cells are situated closer to the diaphyseal end of the plate. The longitudinal growth of bone is a result of cellular division in the proliferative zone and the maturation of cells in the zone of maturation and hypertrophy. This growth within a tissue is called interstitial growth. Most of the chondrocytes in the zone of calcified matrix, the zone closest to the diaphysis, are dead because the matrix around them has calcified, restricting nutrient diffusion. Capillaries and osteoblasts from the diaphysis penetrate this zone, and the osteoblasts secrete bone tissue on the remaining calcified cartilage. Thus, the zone of calcified matrix connects the epiphyseal plate to the diaphysis. A bone grows in length when osseous tissue is added to the diaphysis [13].

When the chondrocytes in the epiphyseal plate cease their proliferation and bone replaces all the cartilage, longitudinal growth stops. All that remains of the epiphyseal plate is the ossified epiphyseal line.

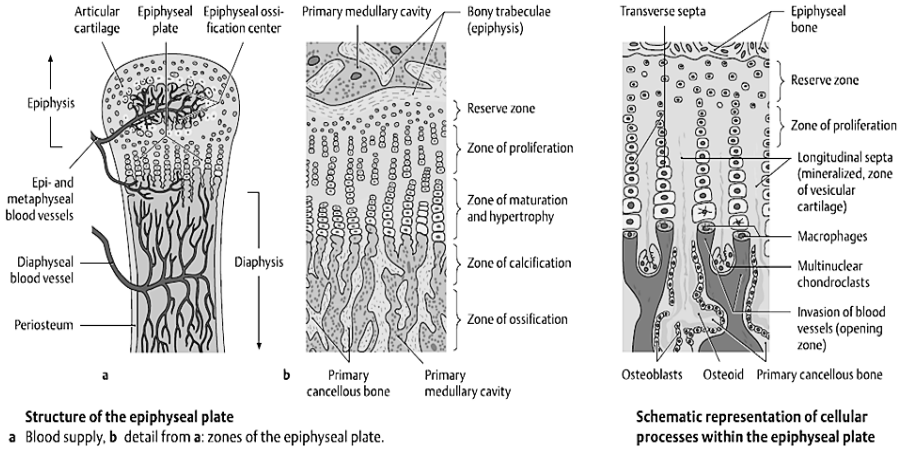

Figure 3.1- Longitudinal bone growth. The epiphyseal plate is responsible for longitudinal bone growth [41].

3.1.2. Appositional Growth

When bones are increasing in length, they are also increasing in diameter; growth in diameter can continue even after longitudinal growth ceases in response to stress from increased muscle activity or to weight. This process is called appositional growth (Figure 3.2).

The bone is absorbed on the endosteal surface and added to the periosteal surface. Osteoblasts and osteoclasts play an important role in appositional bone growth where osteoblasts secrete a bone matrix to the external bone surface from diaphysis, while osteoclasts on the diaphysis endosteal surface remove bone from the internal surface of the diaphysis. The more bone around the medullar cavity is destroyed, the more yellow marrow moves into the empty space and fills the space. Osteoclasts reabsorb the old bone that lines the medullary cavity, while osteoblasts through intramembranous ossification produce new bone tissue under the periosteum. The periosteum on the bone surface also plays an essential role in increasing thickness and reshaping the external contour. The erosion of old bone along the medullary cavity and new bone deposition under the periosteum not only increases the diameter of the diaphysis but also increases the diameter of the medullary cavity. This remodelling of bone primarily takes place during bone's growth, although, in adults, bone undergoes constant remodelling as a result of injuries, exercise and other activities [13].

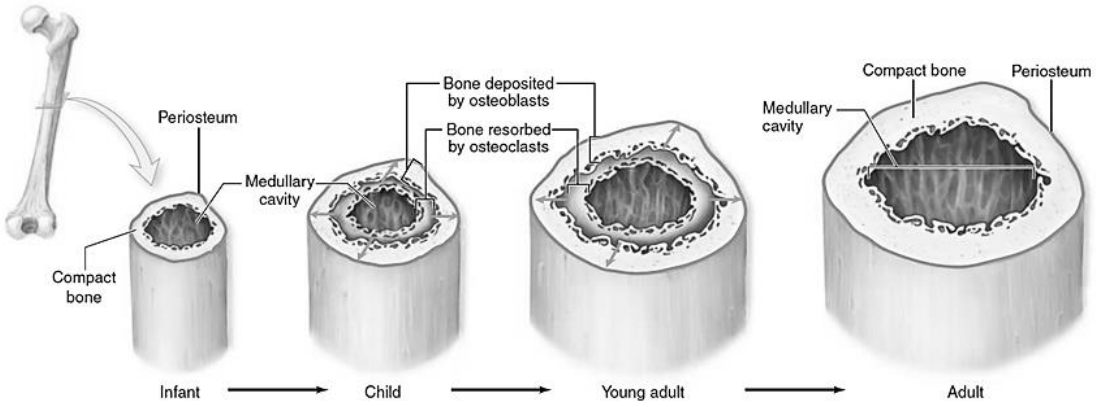

Figure 3.2- Appositional bone growth [40].

3.2. Bone Remodelling

Bone remodelling constitutes a complex and tightly regulated process that involves: repair of microdamage; modification of the structure in response to stress and other biomechanical stimulus; continuous replacement of old bone with new bone to ensure the integrity of the skeleton and, the maintenance of mineral homeostasis. These are accomplished by the coordinated activities of osteoclasts (resorption of bone), osteoblasts (replacement of bone), osteocytes (present in the bone matrix), bone-lining cells (cover the bone surface) and the capillary blood supply [42]. Some significant deviations in this balance between resorption and formation in regulation may imply severe accelerated bone loss or bone gain with disastrous consequences, increasing the probability of fracture or compression syndromes [43].

Bone remodelling occurs in temporary anatomical structures, called Basic Multicellular Units (BMUs), composed of the coupling of osteoclasts and osteoblasts within the bone remodelling cavity. The BMUs will remain longer than the life span of the osteoblasts and osteoclasts within it, and therefore, constant replenishment of these cells is required, ensured by the osteocytes. These structures guarantee a continuous remodelling of bone tissue throughout life. The regulation of the remodelling rate is ensured by a wide variety of calciotropic hormones, such as PTH, thyroid hormone, sex steroids, etc [43]. The structure and composition of BMUs will vary depending on whether they are located within the trabecular or cortical bone (Figure 3.3). In trabecular bone, BMUs are located on a surface, called “Howship's lacunae”, where it is resorbed and then refilled. On the contrary, in cortical bone, the remodelling occurs through tunnels formed by osteoclasts in “cutting cones”, with the removal of damaged bone. Subsequently, behind the osteoclasts, a refilling of new bone occurs in the “closing cone” by osteoblasts [43]. In both cases, the BMUs are covered by cells delimiting the bone remodelling cavity. The BMUs in cortical bone forms a cylindrical channel about 2,000 μm long and 150-200 μm wide, in which osteoclasts gradually burrow through the bone at a rate of 20-40 μm/day. Therefore, the remodelling is between 2% and 5% of the cortical bone each year. Concerning trabecular bone, osteoclasts travel with a speed of approximately 25 μm/day, digging a trench with a depth of 40-60 μm. Thus, considering the surface-to-volume ratio, trabecular bone is more actively remodelled than cortical bone [44].

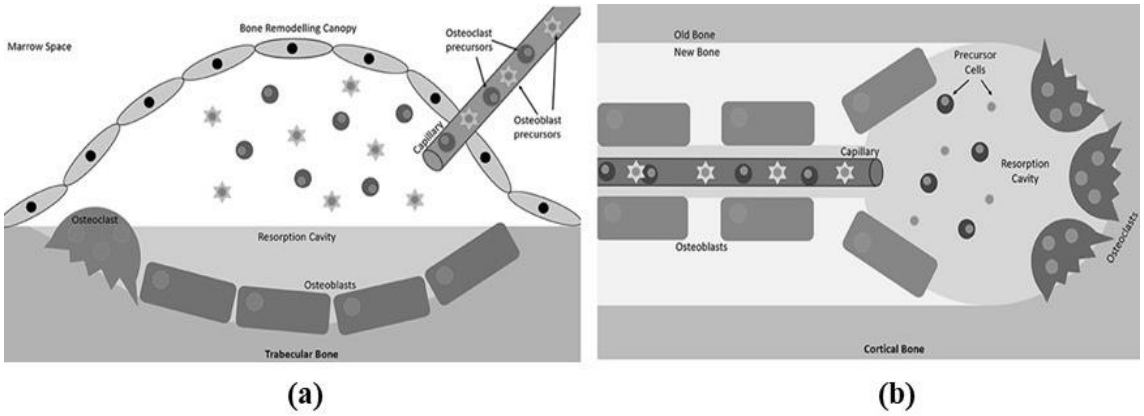

Figure 3.3- Schematic representation of bone multicellular units (BMUs). (a) In trabecular bone, these begin below the bone remodelling canopies formed from bone-lining cells and (b) In cortical bone, at points within the Haversian canals. Adapted from [45].

3.2.1. Bone Remodelling Cycle

Bone remodelling is composed of a sequential process that begins with the activation phase in which osteoclasts are recruited and differentiated into mature osteoclasts. This is followed by the activation and maintenance of bone resorption and then a period of reversal and formation whereby osteoclastic bone formation is inhibited and undergo apoptosis whilst osteoblasts are recruited and begin to differentiate, establishing a new organic bone matrix that subsequently mineralises, as can be depicted in Figure 3.4.

The remodelling cycle occurs over the course of 120-200 days in cortical and trabecular bone, respectively [46]. Additionally, there is a regulation by osteocytes for osteoclast and osteoblast differentiation and thus bone resorption and formation.

I. Activation

The activation phase corresponds to a continuous process that occurs at the boundaries of the BMU, with the recruitment of osteoclast precursor cells after detecting the presence of remodelling initiating signals, which may be related to a mechanical or hormonal nature, from external mechanical stimulus or alterations in systemic homeostasis. This dynamic environment of biophysical stimulus that cells are exposed to

includes stress, strain, shear, pressure, fluid flow, streaming potentials and acceleration, which have the potential to independently regulate cellular responses and influence bone remodelling [42]. As the lining-cells separate from the underlying bone, they expose the bone surface, forming a raised canopy over the site to be resorbed [47].

Additionally, osteocytes located in the cortical bone are sensitive to biophysical stimulus and use the canaliculi network to activate the regulation of the proteins sclerostin and receptor activator of nuclear factor κB ligand (RANKL), which are essential in bone remodelling [48].

II. Resorption

The resorption phase involves the formation and activity of partially differentiated mononuclear preosteoclasts, which adhere to the bone surface and form multinucleated osteoclasts, creating a sealing zone in order to initiate resorption. These activities are controlled by osteoblast cells activating the movement of mature osteoclasts with the expression of colony stimulating factor 1 (CSF-1), RANKL, osteoprotegerin (OPG) and by parathyroid hormone (PTH) [49]. The resorption phase ends with programmed cell death by osteoclasts so that no excess resorption occurs [50].

III. Reversal

The reversal phase occurs from the moment when the maximum eroded depth is reached (between 60 and 40 μm) and is characterised by the transition from osteoclast to osteoblast activity [51]. At this stage, the recently resorbed bone surface is prepared for the arrival of new osteoblasts and consequent deposition of a new bone matrix. Hence, cells of an osteoblastic lineage remove the unmineralized collagen matrix and deposit a cement line of a non-collagenous mineralized matrix in order to increase the adhesion of pre-osteoblasts that begin to differentiate [52].

IV. Formation

The new formation phase involves the deposition of bone by osteoblasts until the resorbed bone is entirely replaced by new bone and is slower than bone resorption. Growth factors released from the matrix that act as chemotactic attract the pre-osteoblasts and stimulate their proliferation. Additionally, the transforming growth factor-β (TGF-β) protein released from the matrix upon bone resorption enables the recruitment of MSC. These cells and the presence of BMP leads to the differentiation of pre-osteoblasts into

osteoblasts. Subsequently, osteoblasts synthesise and secrete an osteoid matrix rich in type 1 collagen, an excess of which contributes to the cessation of cell growth. At this stage, the process of bone mineralisation occurs in which the collagen matrix constructed allows minerals (phosphate and calcium) to begin to form hydroxyapatite crystals between the collagen fibrils creating mature bone tissue [48], [53].

V. Termination

The termination phase includes the terminal differentiation of the osteoblast. Some osteoblasts become bone-lining cells or differentiate into osteocytes and remain within the bone matrix. Osteocytes may secrete inhibitory factors, particularly antagonists of the Wnt signalling pathway, such as SOST, that slow the rate of bone formation as resorbed cavity becomes complete [48], [54].

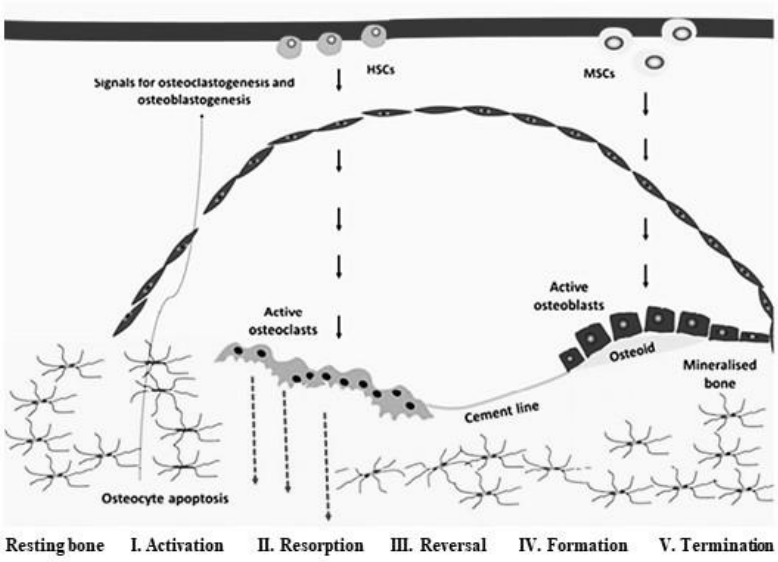

Figure 3.4 – Schematic representation of the bone remodelling cycle, illustrating the phases of: Activation, Resorption, Reversal, Formation and Termination. Haemopoietic stem cells (HSCs), Mesenchymal stem cells (MSCs). Adapted from [55].

3.3. Bone Fractures

Bone fracture is an mechanical event that results from an impact whose applied magnitude was superior to its capacity to resist. This injury causes a loss in bone continuity and scant bone support. It represents one of the most frequent injuries of the musculoskeletal system and the most common form of hospitalised trauma. Fractures of

the femoral shaft, humerus and tibia account for 3%, 14% and 24% of fractures in working-age adults, respectively, and are generally the result of high-energy trauma such as transport accidents and falls from large heights [3].

Long bone fractures are difficult and slow to heal and may require months until consolidation is completed, resulting in long periods of hospitalisation and rehabilitation [56]. Long treatments involve the significant loss of working days with economic effects for the patient and society and also entail the risk of non-union and permanent disabilities related to mal-union, joint stiffness, muscle atrophy, or reflex sympathetic dystrophy [19].

Although the treatment of fractures has improved considerably in recent decades, a large proportion of all fractures, up to 5-10%, still show delayed union, mal-union and non-union associated with some risk factors such as soft tissue injury, extensive bone loss, fracture instability, infection, and a poor general medical condition of the patient (Figure 3.5) [18]. All these aspects contribute not only to considerable individual disability and consequent loss of productivity but also to a reduction in quality of life and significant treatment costs [18]. In fact, in the United Kingdom (UK), the cost of hospital treatment of non-union has been estimated at £7000 to £79,000 [57], [58]. In the United States (US), direct costs for healthcare in the first six months post-injury are estimated at up to $23,000 per isolated limb fracture and specifically the average cost of treating fracture non-unions has been estimated at $25,556 per open tibial fracture, with increased healthcare utilisation, and increased drug prescription [57], [58].

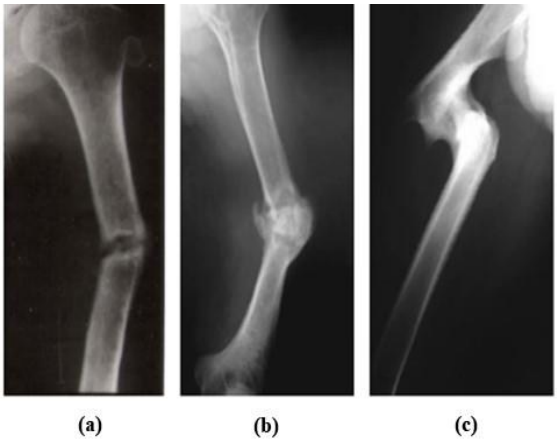

Figure 3.5 – Radiographic images of a delayed union, non-union and mal-union. (a) Humeral delayed union, (b) atrophic non-union of the midshaft of the humerus, (c) sever mal-union of the proximal femur; the fracture united with shortening of 5 cm and severe malalignment due to complete translation and angulation. Adapted from [59], [60].

Bone fractures can be classified as open (or compound) if the bone perforates through the skin and closed (or simple) if the skin is not perforated. In closed fractures, distinct events may develop: a transverse fracture, occurs in a straight line through the bone; oblique fracture, the fracture is diagonal across the bone; spiral fracture, a twisted bone; comminuted fracture, bone broken into three or more pieces; avulsion fracture occurs when a fragment is pulled off the bone by a tendon or ligament; impacted fracture occurs when the extremities go into one another by the force of the injury that caused the fracture; torus fracture, occurs when only one side of the bone is compressed and buckles but does not break and, greenstick fracture, bone bends and breaks, but there is no separation into two parts (Figure 3.6).

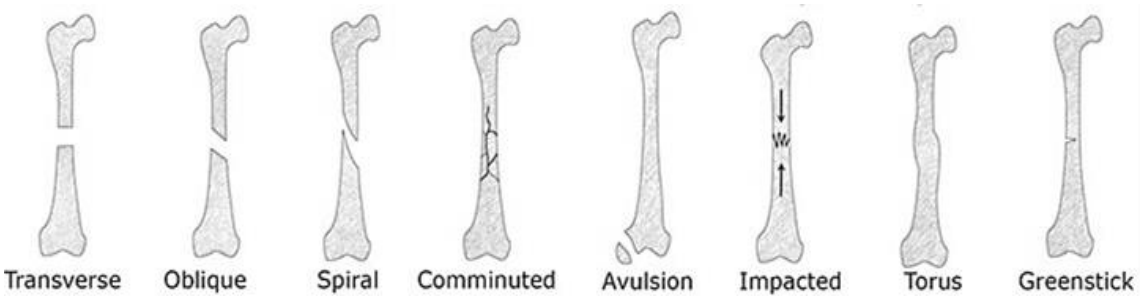

Figure 3.6 – Types of bone fractures. Adapted from [61].

3.4. Biology of Bone Fracture Healing

Unlike other tissues, the "perfect" regeneration capability of the bone is unique, being able to recover its form without permanent scars. Knowledge of the mechanisms involved and their interdependencies with external factors supports the understanding of the accelerated regeneration processes and the success of rehabilitation.

The healing process strongly depends on the mechanical actions on the callus, which determine the relative movement of the bone fragments. In fact, formation of new bone after a fracture is a complex interaction of cellular and molecular processes by which connective tissue, cartilage and bone are formed [62]. Constant remodelling of these tissues reconstitutes the bone's anatomy and structure and recovers its functional competences. The most fundamental aims of the healing process are recovery of load bearing capacity and restoration of bone strength. As both aims represent mechanical

features, it is not surprising that the processes of tissue differentiation and formation are primarily regulated by mechanobiological feedback signals. The mechanical stimulus is experienced by the cells in the healing zone leading to congregation of mesenchymal cells in the early healing phase, formation of callus tissue in the repair phase and the reconstitution of the original bone in the final remodelling phase.

3.4.1. Classification of Fracture Healing

The fracture results in a series of tissue responses that remove tissue debris, re-establish the vascular supply, and produce new skeletal matrix [63]. Fracture healing is a natural process to reconstruct injured tissue and restore its original function and form, returning to the preinjury state. There are two main types of fracture healing: primary (direct) and secondary (indirect).

3.4.1.1. Direct or Primary Fracture Healing

Primary fracture healing (also known as direct healing, or intramembranous bone formation), is a faster healing process than the secondary healing and does not commonly occur in the natural process of fracture healing [64]. It requires surgical stabilization with perfect reduction of the fracture fragments and a rigid construct. Primary healing of fractures involves direct cortical remodelling without any external tissue (callus) formation [65]. It can either occur through gap healing or contact healing of the fractured compact bone ends, under small displacements (Figure 3.7). Primary bone formation by gap healing occurs when small gaps (less than 800 μm to 1 mm) exist between the fractured ends. Is a result of woven bone bridging the gap followed by remodelling to lamellar bone [66], [67]. Larger gaps will heal via secondary healing. In the primary bone formation by contact healing the two fractured bone ends are in full contact and stable by using an internal fixation device. Is a result of simultaneous bony union, lamellar remodelling and re-establishment of Haversian canals [67].

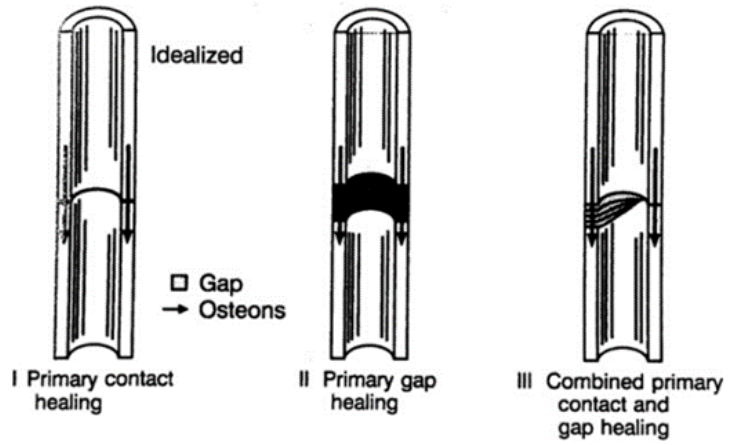

Figure 3.7- Schematic representation of primary osteonal bone healing [68].

3.4.1.1. Indirect or Secondary Fracture Healing

Secondary healing (also known as indirect healing, endochondral ossification or callus healing), is an ordered process of bone repair and reorganization and is the process by which most fractures heal naturally and occurs in the presence of some inter-fragmentary movement between the extremities of the fractured bone. Thus, does not require fracture fragment reduction and rigid stabilization, in fact, it is enhanced by micro-motion and weight-bearing [67].

The interfragmentary motion causes soft callus formation and leads to secondary bone formation through both intramembranous and endochondral ossifications (Figure 3.8) [62]. Recovery of bone strength is generally more rapid than in primary healing. The callus stabilizes the fracture by enlarging its cross-sectional area and increasing its stiffness through tissue differentiation. As the callus stiffens, the interfragmentary movement decreases with healing time. Lastly, the hard callus bridges the bone fragments and reduces the interfragmentary movement to such a low level that bone formation can occur in the gap.

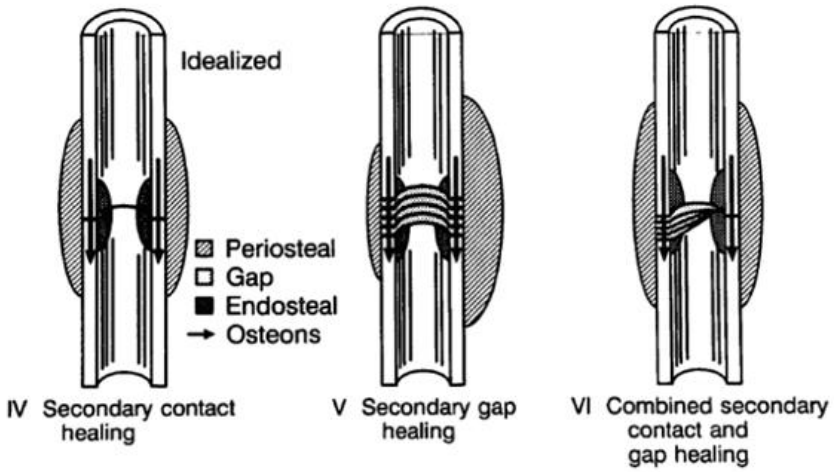

Figure 3.8- Schematic representation of secondary osteonal bone healing [68].

3.4.1.2.1. Stages of Bone Repair during Secondary Fracture Healing

Bone fracture healing is a multipart, arranged, reformative procedure that contains a vital numeral of progenitor cells along with inflammatory, endothelial and hematopoietic cells [69].

The process of bone repair by secondary healing is divided into three overlapping stages – the inflammatory (resulting in granulation tissue), reparative (formation of soft and hard callus tissue), and remodelling (resorption of the callus) (Figure 3.9) [62].

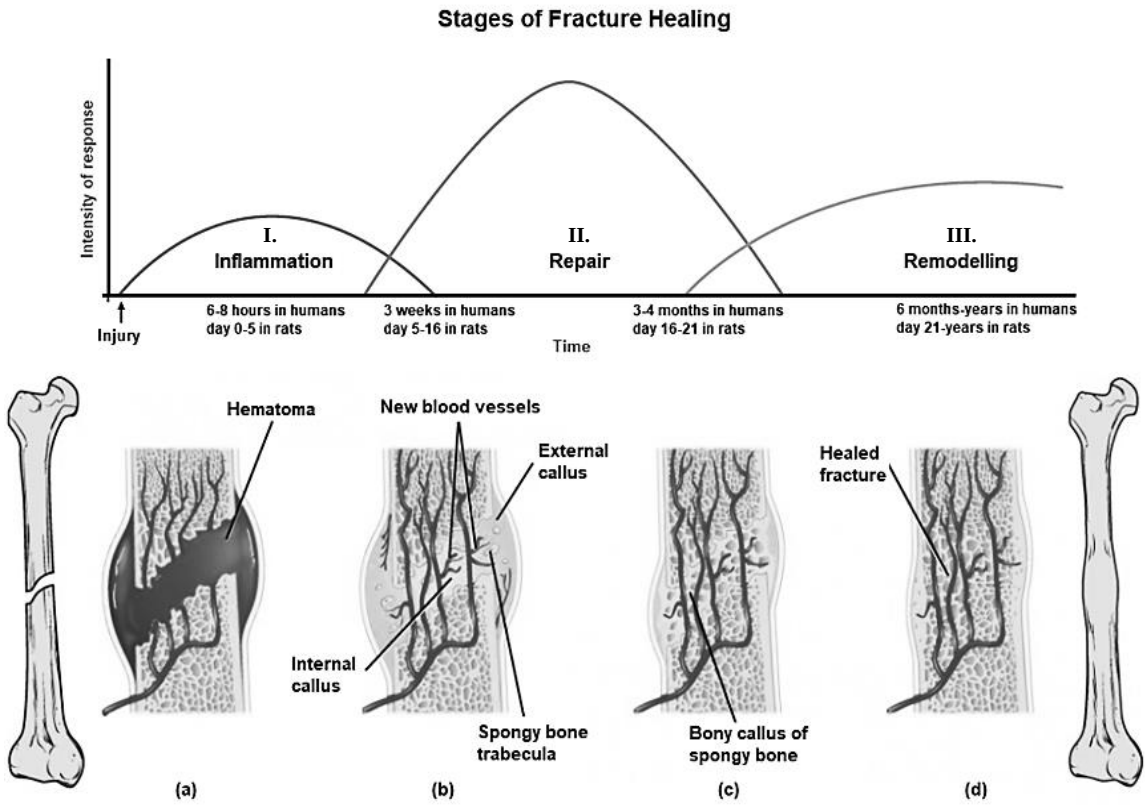

Figure 3.9- Stages of fracture healing. Fracture healing can be divided into three overlapping phases: inflammation, repair and remodelling. (a) A fracture hematoma forms. (b) Internal and external callus form. (c) Cartilage of the callus is replaced by trabecular bone. (d) Remodelling occurs. Adapted from [19], [70], [71].

I. Inflammatory Phase

The first stage begins after bone fracture, with the inflammatory phase. Blood emanates from the ruptured vessels and a haemorrhage quickly fills the fracture gap space, creating a hematoma. The hematoma is characterized by hypoxia and low pH, and contains peripheral blood-derived inflammatory cells, along with pro-inflammatory and anti-inflammatory cytokines (Figure 3.10).

The first cells to be recruited are polymorphonuclear neutrophils (PMNs), attracted by dead cells and debris and rapidly accumulate during the first hours after injury. PMNs are short-lived (about 1 day) but secrete several chemokines that attract longer-lived macrophages. The resident macrophage cell population (osteomacs) – present on the endosteal and periosteal surfaces near bone lining cells of healthy unfractured bone – are fundamental for the formation of intramembranous bone during

fracture healing. However, inflammatory macrophages recruited to the site of injury have a particular influence on endochondral ossification. After macrophage activity, the lymphocytes migrate into the fracture callus and initiate the adaptive immune response.

At the beginning of the inflammatory phase a large number of pro-inflammatory cytokines are released (interleukin-1 (IL-1), IL-6, tumor necrosis factor-α (TNF-α), receptor activator of nuclear factor κB ligand (RANKL), macrophage colony stimulant factor 1, members of the transforming growth factor (TGF)-β superfamily (morphogenetic bone protein BMP-2, BMP-4, BMP-5, BMP-6) and angiogenic factors (angiopoietin-1, and vascular endothelial growth factor)) as a result of hypoxic conditions created by the disturbed vascularisation. These proinflammatory mediators have chemotactic effects on other inflammatory cells. An additional aggregation of platelets and angiogenesis then occurs. Angiogenesis is necessary to re-establish normoxic conditions, remove debris and supply the fracture zone with cells and mediators. Therefore, the endothelial cells, fibroblasts, and osteoblasts participate in filling the fracture gap by the formation of granulation tissue, rich in collagen fibres, invasive cells and capillaries. Throughout the inflammatory phase, a primitive callus develops and reduces the uncontrolled mobility at the fracture site. Under a normal condition, the inflammatory stage is fast and lasts up to a week after the fracture. Subsequently, lymphocytes are not required for the initiation of wound healing, but an intact cellular immune response is essential for a normal outcome of tissue repair. Injury affects lymphocyte immune mechanisms leading to generalized immunosuppression, which, in turn, increases host susceptibility to infection and sepsis. Posttraumatic impairment of T-lymphocyte immune function is reflected by the decreased lymphocyte numbers, as well as the altered T-cell phenotype and activity. Antibody-producing B lymphocytes are variably affected by injury, probably secondary to alterations of T-lymphocyte function, because of their close interaction with helper T cells [62].

Following the inflammatory response, mesenchymal stem cells (MSCs) are recruited to the fracture location and may differentiate into chondrocytes, osteoblasts or fibroblasts, depending on the biological and mechanical conditions. These differentiated cells begin to synthesize the extracellular matrix of their corresponding tissue. Intramembranous (woven) bone is produced by direct differentiation of the stem cells into osteoblasts and appears adjacent to each side of the gap site, advancing to the centre of

the callus. The conditions at the rest of the fracture site led to preferred differentiation of MSCs to chondroblasts for endochondral bone repair [62].

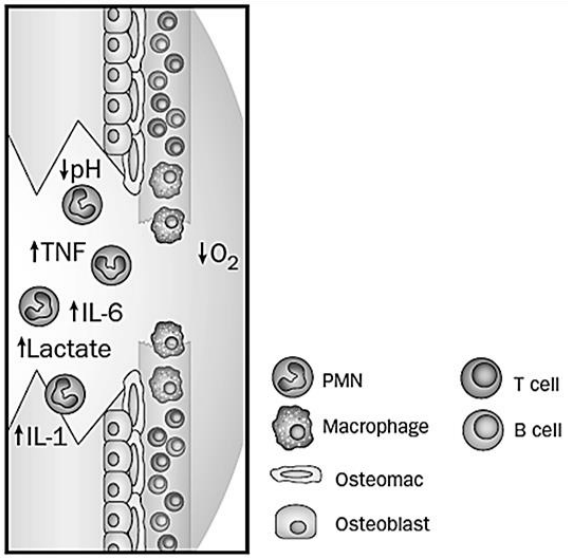

Figure 3.10- Schematic representation of the inflammatory phase during fracture healing. After the initial trauma, the fracture hematoma is formed as a result of blood clotting. It is characterized by hypoxia and low pH and contains blood-derived inflammatory cells from the peripheral blood, along with pro-inflammatory and anti-inflammatory cytokines. In the inflammatory phase, immune cells are recruited to the fracture site, with neutrophils being the first cells to invade the callus, followed by macrophages and lymphocytes. Adapted from [62].

This early inflammatory phase, with its complex network of interactions between molecular factors, immune cells, resident tissue cells and progenitor cells, precedes the onset of the repair phase by stimulating angiogenesis, attracting and promoting differentiation of MSCs, and enhancing extracellular matrix synthesis. This stage is not radiographically visible as the hematoma is not sufficiently dense.

II. Repair Phase

At the centre of the callus, occurs the second stage of bone healing – the repair phase, with the soft callus (fibrocartilage) formation, partially overlapping with the inflammatory phase – where cartilage is formed by chondrogenesis, except right beside the gap where the stability is still very small, and high relative displacement prevents the differentiation of MSCs (Figure 3.11). The soft callus is principally avascular. Once the callus is filled (mainly by cartilage), endochondral ossification begins following a

complex sequence of cellular events including cartilage maturation and degradation, vascularity and osteogenesis. Chondrocytes become hypertrophic, release calcium and undergo apoptosis. Subsequently, upon bridging of the fracture by the cartilaginous callus wedges, the interfragmentary movement and tissue strain during loading of the fracture is markedly reduced, allowing blood vessel to invade the calcified cartilage and resulting in hypervascularization. Blood vessels enable the recruitment of MSCs and monocytes. Whereas monocytes differentiate into osteoclast-like cells, which resorb the calcified cartilage, MSCs differentiate into osteoblasts, which fill the resorption lacunae with new bone. The osteoblasts begin to synthesize intramembranous (woven) bone tissue distal to the fracture site. Endochondral bone formation occurs in the region, which is mechanically less stable. TGF- β2 and TGF- β3, BMPs, and other molecular signals induce endochondral bone ossification in the cartilaginous callus [62]. The second stage is the earliest that the evidence of callus formation will be seen on a radiograph.

At a later stage of bone healing the hard callus formation occurs. Vasculature ingrowth in the soft callus increases the oxygen tension which promotes osteoblast differentiation and the formation of bone. The soft callus is removed and replaced with irregular and under-remodelled woven bone increasing the stability of the fracture or the osteotomy site. This stage is highly evident on radiographs with copious visible callus.

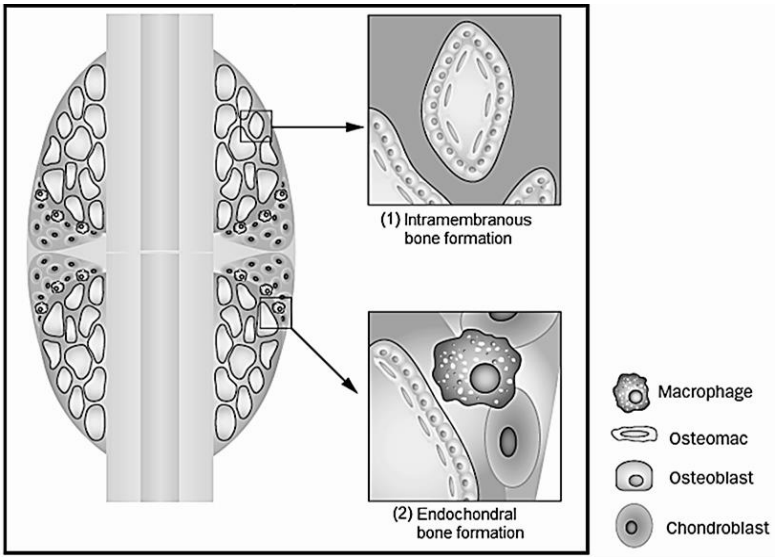

Figure 3.11- Schematic representation of the repair phase during healing of the fracture. In this phase, osteomacs are essential for osteoblast-driven mineralization in areas of intramembranous ossification (1), while inflammatory macrophages mainly contribute to endochondral bone formation (2). Adapted from [62].

III. Remodelling Phase

The third and final phase involves the formation and mineralization of the callus and replacement of the mineralized callus with mineralized bone and sculpting of the bone back to its original structure, shape, and biomechanical competency via modelling and remodelling. This stage entails the remodelling of the woven bone hard callus into its original lamellar configuration, cortical or trabecular. This process is similar to bone remodelling and is mediated by osteoclasts and osteoblasts. Osteoclasts resorb the newly woven bone and osteoblasts replace this matrix with the lamellar bone. Therefore, the balanced action of osteoclastic resorption and osteoblastic deposition is governed by Wolff's law. The important functional outcome of the remodelling phase of fracture healing during homeostatic remodelling is the restoration of mechanical strength and stability [67].

The process of replacement as well as the mechanisms involved in fracture healing have major similarities with the mechanism of the healthy skeleton, although, there are some differences in the process according to if it is occurring in cortical or trabecular bone. In the case of trabecular bone, the cells are close to the blood vessels and so the whole process of bone apposition or replacement occurs on the surface of the trabeculae. This remodelling phase is regulated by several proinflammatory signals. In contrast with hypervascularization of the fracture zone during the repair phase, vascularization during remodelling is reduced to pre-fracture levels. In addition, growth hormone and parathyroid hormone also play key roles in this phase, speeding up the healing and strengthening of the fractured callus [67].

In order to enhance stability and strength at the fracture site, the size of the callus must be sufficiently large to compensate for the relatively poor strength of primitive bone. Lamellae are aligned in a direction parallel to the longitudinal axis of the greatest force and adequate loading is required to enhance osteogenesis and direct the optimal geometric configuration of osteons [67].

In this third phase, a large portion of the biomechanical strength of the bone is restored but remodelling is necessary to regain full strength. Adequate strength develops by 6 months and remodelling phase may occur over months to years. Permanent evidence of fracture will remain on X-ray. Mechanical bone strains created by muscular forces present during physical activity stimulate the remodelling.

Therefore, an adequate blood supply and a gradual increase in mechanical stability are essential for successful bone remodelling. This is demonstrated in cases where neither is achieved, resulting in the development of an atrophic fibrous non-union. However, in cases in which there is good vascularity but unstable fixation, the healing process progresses to form a cartilaginous callus but results in a hypertrophic non-union or a pseudoarthrosis [67].

3.5. Mechanical Properties in Bone Fracture Healing

As mentioned in chapter 2, tissues are composed of structures of various length scales, and as a consequence, the mechanical properties of the material are dependent on the chosen scale. Thus, through experimental tests, the viscoelastic material properties of tissues have been determined and evaluated at the following levels: macroscopic, by standard mechanical tests (compression tests); microscopic, by scanning acoustic microscopy (SAM) or nanoindentation and, at an even lower level by atomic force microscopy (AFM). However, the determination of these properties at the distinct levels are complex and difficult tasks to perform, as these are measured *ex vivo* which, in order to access the desired tissues, may lead to non-physiological conditions [72]. In addition, in order to simplify the investigations, non-linear tissue properties are neglected. Moreover, given the hierarchical organization, the anisotropy makes the theoretical descriptions of the materials and experimental studies more complex [73].

It should be noted that tissues are living materials and that material properties may vary considerably over time due to mechanical or biological influences. Particularly in "normal" bone fracture healing, as tissues regenerate and remodel, the material properties change. Thus, considering cortical bone, its mechanical properties vary depending on the site. For example, the tensile strength of the human femur and tibia, which are located in the leg, differ considerably (Femur $-\ 124\ \text{MPa}\ \pm 1.1$; Tibia $-\ 174\ \text{MPa}\ \pm 1.2$) [74]. Additionally, the macroscopic anisotropy along the long bone axis of the human femur was shown by the respective elastic modulus, wherein the longitudinal direction $E\ =\ 18.2\ \text{MPa}\ \pm 1.01$ and in the transverse direction $E\ =\ 11.7\ \text{MPa} \pm 0.85$, in both cases under compression [75]. Whereas for lower hierarchical levels, for example, the elastic modulus of cortical bone packages in fibrolamellar bovine bone ($\sim 100\ \mu\text{m}$) differ by 20

times, depending on the orientation of the fibrils [76]. Furthermore, the compressive elastic modulus of cortical bone corresponds to about 20 GPa [77], constituting a rather high stiffness of the bone.

On the other hand, experimental studies have established that the (bulk) elastic modulus of trabecular bone is dependent on the bone volume fraction. This relationship was defined by a power law. Consequently, the (bulk) elastic modulus will depend on the elastic modulus of the material E_{mat} and the bone volume fraction BV/TV [78].

Regarding the measurement of the material properties of cartilage and soft tissue, these represent a major problem, particularly when applied to studies evaluating the mechanical properties during the bone healing process. One of the few nanoindentation studies found intended to evaluate the material properties of the tissue within the fracture callus concluded that the callus corresponds to a heterogeneous mixture of the tissues present and, therefore, showed a wide range of indentation modulus. Specifically, this mixture and the consequent maturation of the tissues leads to a significant variation in the values describing the soft tissue or cartilage [79]. Additionally, after blood coagulation in the fracture, granulation tissue corresponds to the first tissue to be formed. Thus, in a nanoindentation test, a mean elastic modulus of $0.99\,\text{MPa} \pm 0.2$ was shown [79]. Subsequently, the granulation tissue is replaced by fibrous tissue over time. In an experimental test performed on dogs, the elastic modulus found was about 1.9 MPa under unconfined uni-axial compression [80]. Additionally, most experimental studies performed on cartilage encompass articular cartilage in which the range of elastic modulus for cartilaginous tissue begins from 1 MPa [81] to 11.8 MPa [82].

CHAPTER 4 – NUMERICAL METHODS

4. Numerical Methods

Several physical systems that occur in a wide range of engineering and science areas (such as physics, biology, structural mechanics, biomechanics, image processing, control theory, circuit analysis, etc.) can be modelled in order to understand and interpret the behaviour of each system. These are formulated in terms of algebraic, ordinary or partial differential and/or integral equations, constituting conceptual and mathematical models that simulate any physical event based on scientific laws of physics [42]. However, the majority of physical systems that occur in nature involve complex phenomena, where computing exact or analytical solutions can be challenging. Consequently, in these cases, numerical [83] or semi-analytical [84] methods are proven to be better. Numerical methods calculate approximate solutions, but very precise, to mathematical problems through discretization of continuous processes. Thereby, the continuous space is separated into discrete pieces, called nodes, i.e., a spatial and temporal discretization is performed. Typically, in the various numerical methods, calculations are performed in an iterative manner until the desired accuracy is achieved.

It is essential to select the approach that best reproduces the phenomenon to be studied. For this purpose, depending on the type of mathematical problem, there will be several numerical techniques that can be used. These techniques are differentiated by their accuracy, the complexity of the necessary programming, and the length of calculations to be performed [85]. Hence, the development and application of numerical models depend on the accuracy of the numerical method selected and the algorithm implemented to find the respective solution.

Similarly, the accuracy of the computed solution is limited by the capabilities and efficiency of the available computer resources. The significant advance in computational power with fast electronic digital computers has enabled the resolution of complicated and repetitive calculations producing solutions in a very short time. This progress has contributed not only to the improvement in the cost-effectiveness of numerical procedures, but also a variety of software and programming techniques have been developed that provide efficient platforms for numerical solving [85], [86].

Therefore, for the analysis of complex natural phenomena from numerical simulations to be effective, it is necessary that both the physical modelling, the

mathematical formulation of numerical methods, and their implementation and execution by computer are properly addressed.

Nowadays, in numerical simulations, either mesh-based methods (such as Finite Element Method (FEM), Finite Volume Method (FVM), Finite Difference Method (FDM), Boundary Element Method (BEM)) or meshless methods are used [75]. Among the advanced discretization techniques, the FEM and meshless methods and their variants are the most widely used techniques in the analysis of engineering problems [42].

The application of numerical methods is a growing tool in biomedical research. In the long term, very reliable predictions will be expected to direct the field towards patient-specific simulations to improve diagnosis and personalized disease treatment planning [87].

In the present chapter, an introduction on the FEM is covered, followed by a more detailed presentation on the meshless methods formulation, particularly the Radial Point Interpolation Method (RPIM), reporting the different concepts associated with these numerical methods.

4.1. Finite Element Method

The finite element method (FEM) is the most widely found discretization technique in the literature, with several academic and industrial applications. It emerged in order to solve complex problems of elasticity and structural analysis in aeronautical and civil engineering. To this purpose, in 1941, Hrennikoff and Courant developed a mesh discretization methods [88], [89]. Subsequently, in the early 1960s, with the arrival of digital computers, the concept of the FEM was coined by Ray W. Clough in his infamous work entitled “The finite element method in plane stress analysis” [90]. It is a robust method for computing the displacements, stresses and strains in a structure subjected to a set of loads. Since this period, FEM had exponential growth and was quickly defined as a powerful approach to solving many problems in various fields.

The finite element can be defined as a small portion of a continuum (i.e., a structure), where the word “finite” differentiates such portion from the “infinitesimal” elements of a differential calculus. The geometry of the continuum is composed by assembling a set of non-overlapping domains with finite elements of simple geometry

[91]. Hence, the problem domain is discretized into a finite number of elements constructing a mesh, which allows the relations and connectivity between them to be established. The mesh consists of sets of elements with the corresponding ordered nodes. In several real cases with geometries that are not regular in a global domain Ω, the approach employed is based on the formation of polygons that cover this domain in a general manner and adaptively maintain the discretization densities [86].

The generic steps of the numerical procedure correspond firstly, to obtain the discretized mesh and the interpolation function, in order to provide an approximation of the unknown solution within an element. For this, polynomial functions (shape functions) are used. Simple shape functions (built over elements and constructed with basis functions (monomial, splines, etc.) of degree 1 or 2) are defined on the mesh such that the interpolation function has the largest value at node $\boldsymbol{x_i}$ [86]. In addition, the FEM shape functions possess the Kronecker delta function property. This is followed by the main step in the FEM, the formulation of the discrete equation system using the Galerkin method. Subsequently, the global equation system is obtained by combining the local element equations for all the elements used for discretization. Afterwards, the boundary conditions must be imposed and, finally, the global system of equations can be solved and the respective solution obtained [92].

In the discretization of a one-dimensional (1D) domain, the elements are often short line segments interconnected to form the original line (Figure 4.1(a)). For a two-dimensional (2D) domain, the elements are usually triangles (best suited for irregular regions) and quadrilaterals (Figure 4.1(b)). The three-dimensional (3D) domain can be subdivided into tetrahedrons, hexahedrons, or pentahedrons (Figure 4.1(c)). The tetrahedrons are the simplest and most suitable for arbitrary-volume domains.

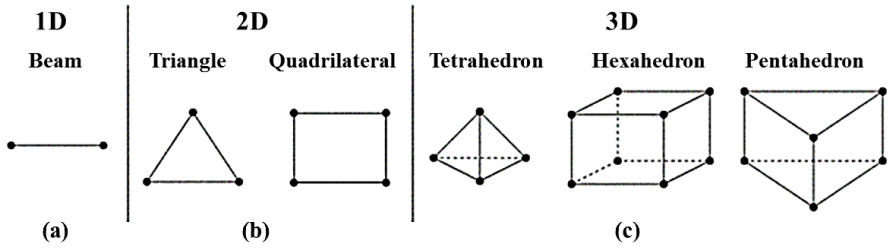

Figure 4.1- Basic finite elements for a (a) one-dimensional (1D), (b) two-dimensional (2D) and (c) three-dimensional (3D) domain discretization.

In addition, Figure 4.2. shows an example of a discretized mesh for the FEM of a 2D and 3D domain.

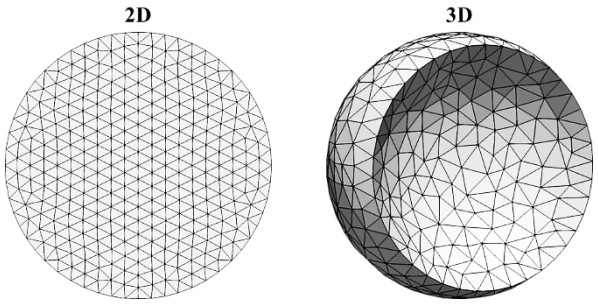

Figure 4.2- Examples of finite element discretization with triangular and tetrahedral elements.

Furthermore, it should be noted that the accuracy that can be obtained from any model is related to the finite element mesh that is used. As previously mentioned, there is a set of polynomial functions defined over each element and, as the mesh is refined where, for example, the elements become progressively smaller, the computed solution approaches the true solution. Therefore, the mesh refinement process is an essential step to validate any FE model and acquire reliability in the software, the model, and the results obtained.

In FEM, the desired accuracy can be reached using systematic refinement. A mesh can be constituted by its local size *h* and the solution on it by its order of approximation of *p* [93]. Therefore, the refinement can be performed by adding additional discretization nodes into the mesh, reducing the element size (h-refinement) or by using higher-order interpolating base functions (p-refinement) (Figure 4.3) [86]. The *h* method improves the results by obtaining a finer mesh of the same element type. In contrast, the *p* method despite, constituting the same mesh, increases the accuracy of the displacement field in each element [94].

Similarly, there are also global and local adaptive mesh refinement strategies (Figure 4.4). In the first, smaller elements are used in regions where the local error is significant, and the local error in the whole model is considered. In the second, the error is evaluated only in some subset of the entire model space. For example, it allows the

mesh to be refined such that the stresses in a particular region of interest are resolved more accurately [94].

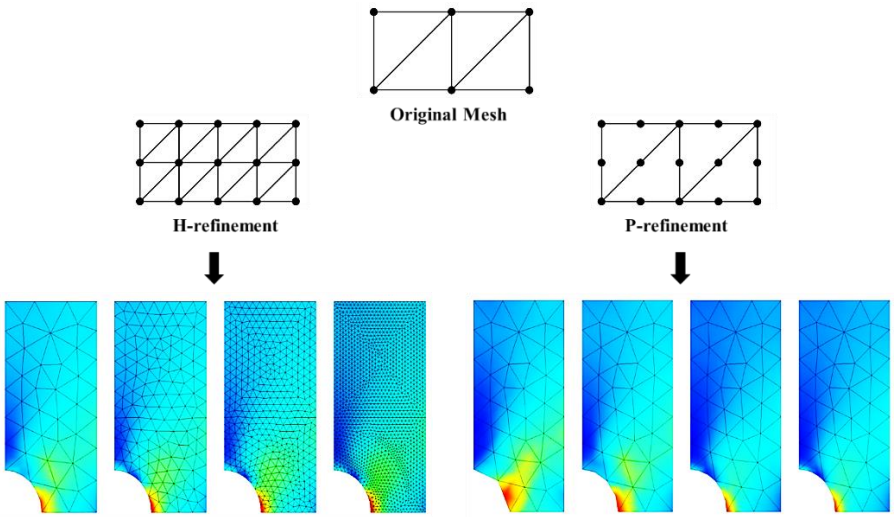

Figure 4.3- *H*- and *P*- refinement methods in 2D with an application example consisting of a finite element mesh of a plate with a hole and the corresponding stresses solved with different element sizes (left) and the same finite element mesh, but solved with different element orders (right). Adapted from [94].

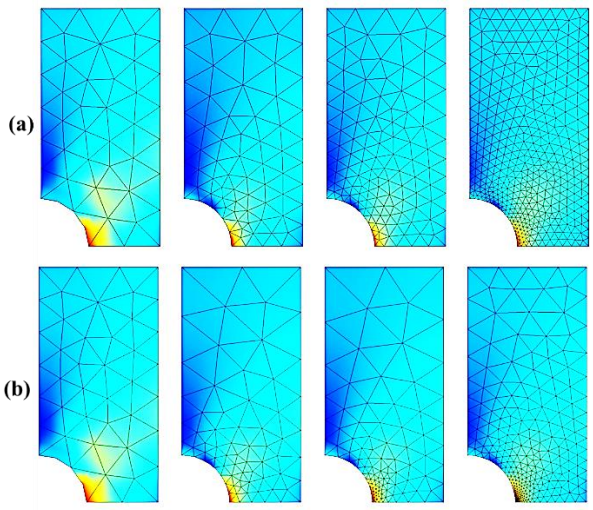

Figure 4.4- Adaptive mesh refinement strategies. Application example consisting of a finite element mesh of a plate with a hole with (a) global adaptive mesh refinement that changes the element sizes in a non-uniform manner and (b) local adaptive mesh refinement concerning stresses at a point [94].

Therefore, FEM represents a robust and extensively developed technique, which has been used with great success in many engineering fields. However, it is not exempt from limitations. Since FEM corresponds to a classical mesh-based method, it becomes a challenge to generate a good quality mesh according to the geometry and the specific requirements of a physical phenomenon. Moreover, this is even more complicated in problems with large deformations. Accuracy losses and higher errors can occur when the mesh elements become extremely skewed or distorted. It is also inadequate for problems containing discontinuities that do not coincide with the original mesh lines. Additionally, the mesh generation and refinement processes in FEM are usually computationally expensive [95], [96].

4.2. Meshless Methods

In the last fifteen years, there has been particular interest in numerous meshless methods for the numerical solution of partial differential equations (PDEs) [97], and have been developed and applied in various engineering fields and applied sciences. The studies of meshless methods attracted the attention of the computational mechanics community as a simulation methodology for scientific and engineering problems. Until recently, remarkable progress has been observed in wide-ranging problems [96].

Meshless methods were born with the aim of overcoming the limitations of the FEM associated with the dependence on a mesh to construct the approximation. These do not require mesh for the discretization of the domains, and thus, nodes can be distributed arbitrarily. In FEM, this domain corresponds to the “element”, and in the meshless methods, it is called the “influence-domain”, where the field functions are approximated only through a set of nodes within this influence-domain and no elements are required. Additionally, influence-domains may and must overlap each other, contrary to the statement of no-overlap between elements in FEM. A determination of the influence-domain is performed for each node within the nodal distribution allowing the problem domain to be discretised and, as a consequence, both the shape and size of the influence-domain will vary with the node considered. Similarly, the technique applied to determine the influence-domain varies with the meshless method employed [10], [96].

On the other hand, regarding the formulation, meshless methods can be grouped into two categories, based on the use or not of integration [98] or based on computational

modelling [99]. The first category, encompasses methods that do not require integration and, thus, rely on the strong forms of PDEs, which govern the studied physical phenomenon in order to obtain the solution. These include the smooth particle hydrodynamics (SPH) method [100], which was one of the first meshless methods created in this category. Additionally, the finite point method (FPM) [101], the hp-meshless cloud method [102], and the collocation method [103]. Some of the advantages that come from using the meshless strong form method concern the simplicity of implementation and computationally efficient and corresponds to truly meshless method, without any requirement to use a mesh for field variable approximation or integration. Thus, these meshless strong form methods have been successfully employed in computational mechanics, particularly in fluid mechanics problems. However, they also present some limitations such as being numerically unstable and less accurate, particularly for problems governed by PDEs with Neumann boundary conditions [96].

Alternatively, the second category of meshless methods includes methods based on the weak forms of PDEs, where a variational principle is applied to minimise the residual weight of the differential equations governing the phenomenon [10]. Thus, the residual can be obtained by replacing the exact solution by an approximate function affected by a test function [10]. The solution methods become dependent on the test function used [10]. These comprise the use of the global and local weak forms. Within the meshless methods based on the global weak form, the Diffuse Element Method (DEM) [104], the Element Free Galerkin Method (EFGM) [105], [106] and the Reproducing Kernel Particle Method (RKPM) [107] have been developed. In order to avoid global integration, local weak forms are employed to develop local meshless techniques, such as the Meshless Local Petrov-Galerkin (MLPG) method [108], [109].

Thus, the meshless methods based on the weak form are very prominent and have very appealing merits, being successfully applied in solid mechanics problems [96]. These have great stability and excellent accuracy [96]. Additionally, it is essential to remark that several differential equations governing real-world phenomena do not allow sufficiently smooth solutions and, therefore, the only way to solve such equations is through the weak formulation. Nevertheless, the methods described above employ approximation rather than interpolation functions, constituting some of the associated problems. The lack of the Kronecker delta property is the most relevant due to the difficulty in imposing the essential and natural boundary conditions [10].

Consequently, several new meshless interpolation methods have been developed in recent years, such as the Point Interpolation Method (PIM) [110], the Point Assembly Method [111], the Radial Point Interpolation Method (RPIM) [112], the Natural Neighbour Finite Element Method (NNFEM) [113], or Natural Element Method (NEM) [114] and the Meshless Finite Element Method (MFEM) [115]. The NEM in combination with RPIM originated the Natural Neighbour Radial Point Interpolation Method (NNRPIM) [10].

4.2.1. Meshless Generic Procedure

Similar to FEM and other numerical methods, most meshless approaches involve a generic procedure. First, the geometrical model of the problem is created, the solid domain and the contour are defined, and the essential and natural boundary conditions are identified (Figure 4.5(a)). Afterwards, the problem domain, including its boundary, is numerically discretized into a set of nodes following a regular or irregular distribution (Figure 4.5 (b) and (c)).

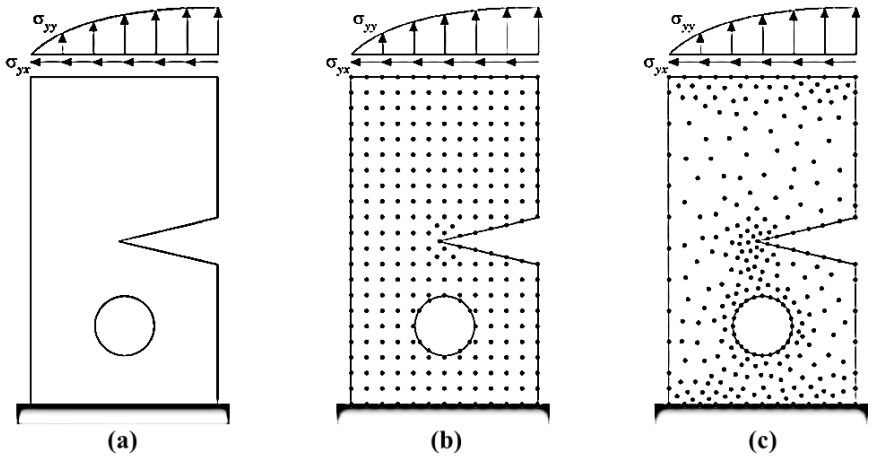

Figure 4.5- Representative examples of (a) solid domain definition, (b) regular nodal discretization, and (c) irregular nodal discretization [10].

This nodal distribution will not constitute a mesh since it is not necessary any previous information about the relation between each node in order to build the approximation (or interpolation) functions of the unknown variable field functions. The crucial aspect required by truly meshless methods concerns the spatial location of each

node discretizing the problem domain. The values of the field variables are calculated at these field nodes. Therefore, the nodal density of the discretization along with the nodal spatial distribution depends on the accuracy requirement. A higher node density generally returns more accurate results. Additionally, irregular nodal distributions have lower accuracy in contrast to regular distributions. In general, particular problems where stress concentrations are expected (fracture mechanics, specific boundary conditions, orifices, etc.) require higher nodal density to obtain better results, compared to locations where smooth stress distributions are predicted.

Subsequently, after performing the nodal discretization of the problem, in most meshless methods, a background integration mesh is constructed to numerically integrate the weak form equations that describe the physical phenomenon. This mesh can be nodal independent, as in the RPIM or nodal dependent, as in the NNRPIM. There is a variation of the size of the integration mesh, and it can have a size adapted or not to the problem domain (Figure 4.6) without significantly affecting the final results. The nodal independent integration meshes generally use the Gaussian integration method, which can be adjusted to the problem domain (Figure 4.6(a)), as it occurs in FEM. Moreover, background meshes larger than the problem domain are also viable (Figure 4.6(b)). Nevertheless, some of the meshless methods use the integration mesh not fitted to the domain where the nodal dependent integration meshes use nodal integration and concepts such as natural neighbours and Voronoï diagrams (Figure 4.6(c)) to integrate the weak form equations.

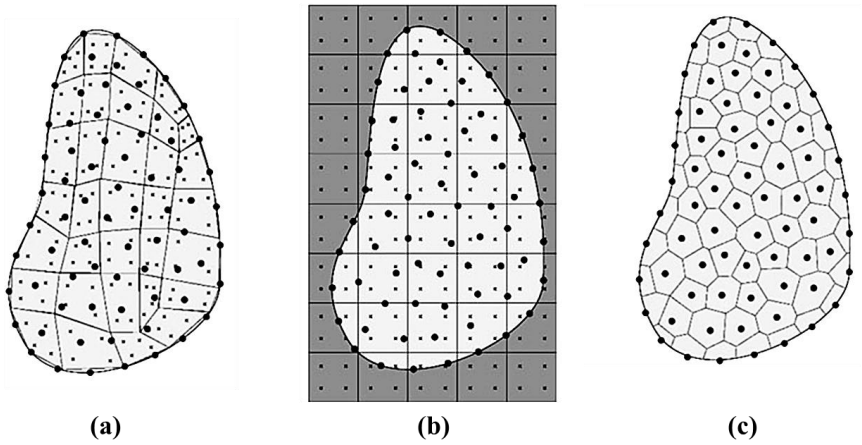

Figure 4.6- Integration meshes. (a) Fitted Gaussian integration mesh. (b) General Gaussian integration mesh. (c) Voronoï diagram for nodal integration [10].

The following step in the generic procedure of the meshless method encompasses the establishment of nodal connectivity. In the FEM, the finite element mesh ensures nodal connectivity, following the non-overlapping rule between elements. Whereas in meshless methods, since there are no elements, nodal connectivity is established from the superposition of areas (for 2D problems) or volumes (for 3D problems) around the nodes, constituting influence domains (RPIM) or influence cells (that result from the Voronoï diagrams in the NNRPIM).

Afterwards, the field variables under study are obtained through approximation or interpolation shape functions, based on the combination of radial basis functions (RBF) with polynomial basis functions. For instance, considering the displacement field $\boldsymbol{u}$ as the field variable, the displacement components $\boldsymbol{u_I} = (u, v, w)$ at a given interest point $\boldsymbol{x_I}$ within the problem domain are approximated using the nodal displacement of the nodes inside the influence-domain or the influence-cell of that interest point $\boldsymbol{x_I}$. Consequently, it is possible to establish the equation for the O_x component of the displacement,

$$\mathbf{u}(\mathbf{x_I}) = \sum_{j=1}^{n} \varphi_j(\mathbf{x_I})\, \mathbf{u}(\mathbf{x_i}) \qquad \text{Eq. (4.1)}$$

where n corresponds to the number of nodes within the influence-domain or influence-cell of the interest point $\boldsymbol{x_I}$; $\boldsymbol{u_I}$ is a vector with the displacement components of each node within the influence-domain or influence-cell and can be obtained from Eq. (4.1) for each degree of freedom: $\boldsymbol{u_I}$, $\boldsymbol{v_I}$ and $\boldsymbol{w_I}$ and, finally, $\varphi_j(\boldsymbol{x_I})$ is the approximation or interpolation function value at the *j*th node, considering the *n* nodes of the influence-domain or influence-cell.

Additionally, the interpolation shape functions have a relevant property, namely the Kronecker delta property, which entails that the function obtained passes through all scattered points in an influence-domain. Consequently, it becomes possible to apply the same simple techniques used in FEM to impose the essential boundary conditions.

In the final instance of the procedure, the discrete equation system based on the strong or weak form formulation is established. The resulting equations are then arranged

in a local nodal matrix form and assembled into a global equation system matrix. Ultimately, for static problems, the displacement field is obtained.

In summary, meshless methods encompass both the imposition of nodal connectivity and the construction of the numerical integration scheme and shape functions. Therefore, in the following sections, each of these steps in RPIM will be described.

4.2.2. Radial Point Interpolation Method

4.2.2.1. Influence-domains and Nodal Connectivity

In RPIM, nodal connectivity is guaranteed from the overlap of the influence-domain of each node. As mentioned above, the influence-domains are defined after the nodal discretization and the integration mesh. These are determined by searching for sufficient nodes within a certain area in 2D problems or volume in 3D problems and can have a fixed or variable size. Therefore, it is possible to obtain different nodal connectivity.

In the present work, 2D and 3D influence-domains are considered. Thus, for each interest point, the influence-domain can assume several shapes. For the two-dimensional case, these may constitute rectangular (Figure 4.7(a)) or circular (Figure 4.7(b)) areas. Similarly, in the three-dimensional case, volumes rather than areas are considered. Note that influence-domains containing a constant size and shape may cause a loss of accuracy in the numerical analysis, as it leads to influence-domains with a different number of nodes. Therefore, it is essential to consider using influence-domains with approximately the same number of nodes. Complementarily, the size and shape of the influence-domain will depend on the nodal density around the integration point. Regardless of the meshless technique applied, according to [112], the influence-domain should possess between n = 9 and n = 16 nodes. Hence, RPIM uses variable size influence-domains, with a constant number of nodes within the domain. Thus, a radial search is performed and using the interest point $\boldsymbol{x_I}$ as the centre, the n closest nodes are found. This procedure is illustrated in Figure 4.7(c), and it is evident the existence of a constant nodal connectivity that avoids the numerical problems identified previously and enables the construction of shape functions with the same level of complexity in the complete domain [10].

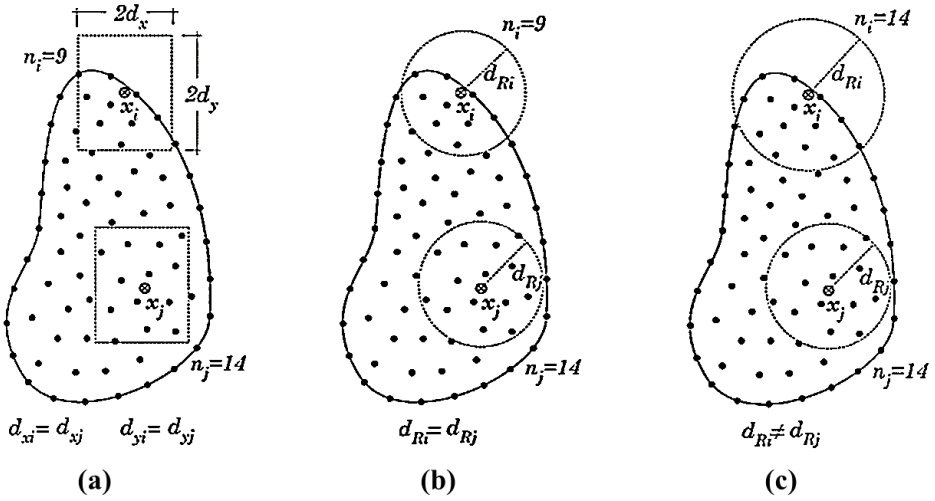

Figure 4.7- Representative examples of distinct types of influence-domains. **(**a) Fixed rectangular shaped influence-domains. (b) Fixed circular shaped influence-domains. (c) Flexible circular shaped influence-domains [10].

4.2.2.2. Numerical Integration

As previously mentioned, the numerical integration process allows the determination of the system of equations based on the integro-differential equations that govern the studied physical phenomenon. Thus, in numerical methods that apply the weak Galerkin formulation, the governing differential equation is converted to a corresponding weak form, and then solved by the numerical integration technique. The governing equations and boundary conditions are satisfied on average over a domain, as opposed to individual nodes, constituting a stable yet time-consuming approach to implement as it involves numerical integration [96]. This process represents a significant portion of the total computational cost of the analysis.

In meshless methods, the shape function degree is usually unknown, which makes it impossible to define a priori the background integration mesh. Therefore, for each distinct meshless approach, the optimal relationship between the density of the field nodes and the density of the background integration mesh must be established to obtain more accurate results.

For the numerical integration, RPIM uses the Gauss-Legendre quadrature integration method to integrate the Galerkin weak form differential equations. Therefore, it is necessary to create a background integration mesh. Applying Gauss-Legendre integration, the solid domain is divided in a regular grid, as depicted in Figure 4.8(a).

Subsequently, each grid-cell is filled with integration points, respecting the Gauss-Legendre quadrature rule. These cells can be triangular or quadrilateral. As illustrated in Figure 4.8(b), a grid-cell is selected (in this case it is quadrilateral) and then it is transformed in an isoparametric square. The integration points are distributed in that isoparametric square, which in this example assume a 2 x 2 quadrature.

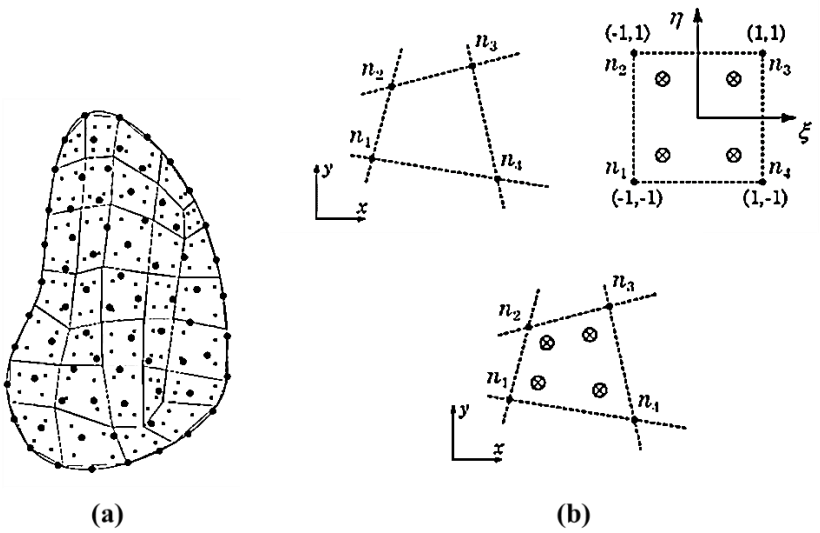

Figure 4.8- Representation of the Gaussian integration mesh and scheme. (a) Gaussian integration mesh. (b) Gaussian quadrature integration scheme with the transformation of the initial quadrilateral into an isoparametric square shape and application of the 2 x 2 quadrature point rule [10].

Subsequently, the Cartesian coordinates of the quadrature points, for quadrilaterals, can be obtained using the isoparametric interpolation functions, N_i, present in Eq. (4.2).

$$N_1(\xi,\eta) = \frac{1}{4}(1-\xi)(1-\eta)$$

$$N_2(\xi,\eta) = \frac{1}{4}(1-\xi)(1+\eta)$$

$$N_3(\xi,\eta) = \frac{1}{4}(1+\xi)(1+\eta)$$

$$N_4(\xi,\eta) = \frac{1}{4}(1+\xi)(1-\eta)$$

Eq. (4.2)

Or for triangles present in Eq. (4.3).

$$N_1(\xi, \eta) = 1 - \xi - \eta$$
$$N_2(\xi, \eta) = \eta \qquad \text{Eq. (4.3)}$$
$$N_3(\xi, \eta) = \xi$$

The Cartesian coordinates are given by,

$$x = \sum_{i=1}^{m} N_i(\xi, n) \cdot x_i$$
$$y = \sum_{i=1}^{m} N_i(\xi, n) \cdot y_i \qquad \text{Eq. (4.4)}$$

where *m* corresponds to the number of nodes inside the grid-cell and x_i and y_i represent the Cartesian coordinates of the cell nodes.

Afterwards, the integration weight of the quadrature point can be calculated by multiplying the isoparametric weight of the quadrature point by the inverse of the Jacobian matrix determinant of the respective grid-cell, according to Eq. (4.5).

$$\boldsymbol{J} = \begin{bmatrix} \frac{\partial x}{\partial \xi} & \frac{\partial x}{\partial \eta} \\ \frac{\partial y}{\partial \xi} & \frac{\partial y}{\partial \eta} \end{bmatrix} \qquad \text{Eq. (4.5)}$$

4.2.2.3. Interpolation Functions

Regarding the interpolation functions (shape functions), RPIM uses the Radial Point Interpolator (RPI) technique, which combines polynomial basis functions and radial basis functions (RBF) to construct the shape functions. In this process, a *d*-dimensional space $\mathbb{R}^d$ is discretized by a set of *n* nodes with coordinates $\boldsymbol{X} = \{\boldsymbol{x_1}, \boldsymbol{x_2}, \dots, \boldsymbol{x_n}\} \in \boldsymbol{\Omega} \wedge$

$\boldsymbol{x_i} \in \mathbb{R}^d$. Thus, it is assumed that only the nodes that are within the influence-domain of the interest point $\boldsymbol{x_I}$ will have an effect on the function $u(\boldsymbol{x})$. For the RPIM, the aforementioned function passes through all nodes using a RBF. The value of the function at the interest point, $u(\boldsymbol{x_I})$, is obtain by,

$$u(\boldsymbol{x_I}) = \sum_{i=1}^{n} R_i(\boldsymbol{x_I})\, a_i(\boldsymbol{x_I}) + \sum_{j=1}^{m} p_j(\boldsymbol{x_I})\, b_j(\boldsymbol{x_I}) = \boldsymbol{R}(\boldsymbol{x_I})^T\, \boldsymbol{a}(\boldsymbol{x_I}) + \boldsymbol{p}(\boldsymbol{x_I})^T\, \boldsymbol{b}(\boldsymbol{x_I}) \qquad \text{Eq. (4.6)}$$

in which $R_i(\boldsymbol{x_I})$ is the RBF, n corresponds to the number of nodes inside the influence-domain of the interest point $\boldsymbol{x_I}$, $p_j(\boldsymbol{x_I})$ defines the monomials of the polynomial basis, with m being the basis monomial number and $\boldsymbol{a_i}(\boldsymbol{x_I})$ and $b_j(\boldsymbol{x_I})$ are non-constant coefficients of $R_i(\boldsymbol{x_I})$ and $p_j(\boldsymbol{x_I})$, respectively. Therefore, Eq. (4.6) can be rewritten,

$$u(\boldsymbol{x_I}) = \{\boldsymbol{R}(\boldsymbol{x_I})^T, \boldsymbol{p}(\boldsymbol{x_I})^T\} \begin{Bmatrix} \boldsymbol{a}(\boldsymbol{x_I}) \\ \boldsymbol{b}(\boldsymbol{x_I}) \end{Bmatrix} \qquad \text{Eq. (4.7)}$$

Subsequently, the vectors of Eq. (4.6) are represented as,

$$\begin{aligned} \boldsymbol{R}(\boldsymbol{x_I}) &= \{R_1(\boldsymbol{x_I}), R_2(\boldsymbol{x_I}), \dots, R_n(\boldsymbol{x_I})\}^T \\ \boldsymbol{p}\,(\boldsymbol{x_I}) &= \{p_1(\boldsymbol{x_I}), p_2(\boldsymbol{x_I}), \dots, p_m(\boldsymbol{x_I})\}^T \\ \boldsymbol{a}\,(\boldsymbol{x_I}) &= \{a_1(\boldsymbol{x_I}), a_2(\boldsymbol{x_I}), \dots, a_n(\boldsymbol{x_I})\}^T \\ \boldsymbol{b}\,(\boldsymbol{x_I}) &= \{b_1(\boldsymbol{x_I}), b_2(\boldsymbol{x_I}), \dots, b_m(\boldsymbol{x_I})\}^T \end{aligned} \qquad \text{Eq. (4.8)}$$

Generally, in order to ensure a more stable function, the number of monomial m of the polynomial basis should be $m < n$.

For the construction of the shape function, the RPIM can incorporate several RBFs. However, the Multiquadratic Radial Basis Function (MQ-RBF) is the most efficient and commonly used. It was proposed initially by Hardy [116] and defined by Eq. (4.9).

$$R_i(\boldsymbol{x_I}) = \mathbf{s}(d_{iI}) = (d_{iI}^2 + c^2)^p \quad \text{Eq. (4.9)}$$

With c and p being the shape parameters of the MQ-RBF. These need to be optimized in order to maximize the performance of the method.

In previous works on the RPI [112], optimal values for the shape functions of $c = 1.42$ and $p = 1.03$ were given. However, these values are inaccurate and lack in stability and precision [117]–[119] . In meshless methods using RBFs, the variation of the shape parameters significantly affects the performance of the RBFs, and there are no standard or precise theoretical methods to obtain the optimal values of *c* and *p* [120]. Therefore, in a study conducted by Belinha et al. [120], an optimization was performed for the shape parameters establishing the values of $c = 0.0001$ and $p = 0.9999$ as the most suitable and, for this reason, are the ones that will be applied in the present work.

Complementarily, in the RBF, the variable is the Euclidean distance between the interest point $\boldsymbol{x_I}$ and node $\boldsymbol{x_i}$ that belongs to the influence-domain. For the 2D and 3D spaces, Eq. (4.10) and (4.11) can be established, respectively.

$$d_{iI} = \sqrt{(x_i - x_I)^2 + (y_i - y_I)^2} \quad \text{Eq. (4.10)}$$

$$d_{iI} = \sqrt{(x_i - x_I)^2 + (y_i - y_I)^2 + (z_i - z_I)^2} \quad \text{Eq. (4.11)}$$

Regarding the polynomial basis added to the RBF cannot be arbitrary. These depend on the chosen monomial number *m*. Generally, a low-degree polynomial basis is often added. Nevertheless, the polynomial basis functions exhibit the following sequences of terms, present in Eq. (4.12) and (4.13), for the 2D and 3D cases, respectively.

$$\begin{gathered}
\boldsymbol{p}^T(\boldsymbol{x}) = \{0\} \text{ (For null basis, } m = 0) \\
\boldsymbol{p}^T(\boldsymbol{x}) = \{1\} \text{ (For constant basis, } m = 1) \\
\boldsymbol{p}^T(\boldsymbol{x}) = \{1, x, y\} \text{ (For linear basis, } m = 3) \\
\boldsymbol{p}^T(\boldsymbol{x}) = \{1, x, y, x^2, xy, y^2\} \text{ (For quadratic basis, } m = 6)
\end{gathered} \quad \text{Eq. (4.12)}$$

$$\boldsymbol{p}^T(\boldsymbol{x}) = \{1\} \text{ (For constant basis, } m = 1)$$
$$\boldsymbol{p}^T(\boldsymbol{x}) = \{1, x, y, z\} \text{ (For linear basis, } m = 4) \quad \text{Eq. (4.13)}$$
$$\boldsymbol{p}^T(\boldsymbol{x}) = \{1, x, y, z, x^2, xy,\ y^2, yz,\ z^2, zx\} \text{ (For quadratic basis, } m = 10)$$

In this work, it is considered the case of a constant polynomial basis and, therefore, it satisfies an extra requirement in order to guarantee a unique solution, represented in Eq. (4.14).

$$\sum_{\mathrm{i}=1}^{n} p_j(\boldsymbol{x_i})\, a_i(\boldsymbol{x_i}) = 0 \iff \boldsymbol{p}^T(\boldsymbol{x_i})\, \boldsymbol{a}(\boldsymbol{x_i}) = 0 \quad \text{Eq. (4.14)}$$

Where $j = \{1,2, \dots, m\}$. Consequently, combining Eq. (4.6) with Eq. (4.14), a new equation matrix can be written,

$$\begin{Bmatrix} \boldsymbol{u_s} \\ 0 \end{Bmatrix} = \begin{bmatrix} \boldsymbol{R} & \boldsymbol{p} \\ \boldsymbol{p}^T & 0 \end{bmatrix} \begin{Bmatrix} \boldsymbol{a} \\ \boldsymbol{b} \end{Bmatrix} = \boldsymbol{G} \begin{Bmatrix} \boldsymbol{a} \\ \boldsymbol{b} \end{Bmatrix} \quad \text{Eq. (4.15)}$$

in which $\boldsymbol{u_s}$ is given by,

$$\boldsymbol{u_s} = \{u_1, u_2, \dots, u_n\}^T \quad \text{Eq. (4.16)}$$

the matrix **R** of the RBF, a $n \times n$, is obtained with,

$$\boldsymbol{R}_{[n\times n]} = \begin{bmatrix} R(r_{11}) & R(r_{12}) & \dots & R(r_{1n}) \\ R(r_{21}) & R(r_{22}) & \dots & R(r_{2n}) \\ \vdots & \vdots & \ddots & \vdots \\ R(r_{n1}) & R(r_{n2}) & \dots & R(r_{nn}) \end{bmatrix} \quad \text{Eq. (4.17)}$$

and the matrix **p** of the polynomial basis, a $n \times m$, is given by,

$$\boldsymbol{p}_{[n\times m]} = \begin{bmatrix} p_1(x_1) & p_2(x_1) & \dots & p_m(x_1) \\ p_1(x_2) & p_2(x_2) & \dots & p_m(x_2) \\ \vdots & \vdots & \ddots & \vdots \\ p_1(x_n) & p_2(x_n) & \dots & p_m(x_n) \end{bmatrix} \quad \text{Eq. (4.18)}$$

Thus, the linear polynomial basis is defined by,

$$\boldsymbol{P} = [\,1 \quad 1 \quad \ldots \quad 1]^{\boldsymbol{T}} \qquad \text{Eq. (4.19)}$$

with the linear polynomial basis for a 2D and 3D problem being represented by Eq. (4.20) and (4.21), respectively.

$$\boldsymbol{P} = \begin{bmatrix} 1 & 1 & \ldots & 1 \\ x_1 & x_2 & \ldots & x_n \\ y_1 & y_2 & \ldots & y_n \end{bmatrix}^{\boldsymbol{T}} \qquad \text{Eq. (4.20)}$$

$$\boldsymbol{P} = \begin{bmatrix} 1 & 1 & \ldots & 1 \\ x_1 & x_2 & \ldots & x_n \\ y_1 & y_2 & \ldots & y_n \\ z_1 & z_2 & \ldots & z_n \end{bmatrix}^{\boldsymbol{T}} \qquad \text{Eq. (4.21)}$$

It should be noted that the geometric matrix **G** corresponds to a symmetric matrix since the distance between the interest points and the nodes belonging to a given influence-domain are directional independent ($R(r_{ij}) = R(r_{ji})$). Thus, solving Eq. (4.15),

$$\begin{Bmatrix} \boldsymbol{a} \\ \boldsymbol{b} \end{Bmatrix} = \boldsymbol{G}^{-1} \begin{Bmatrix} \boldsymbol{u_s} \\ 0 \end{Bmatrix} \qquad \text{Eq. (4.22)}$$

It is possible to substitute Eq. (4.22) in Eq. (4.7) obtaining,

$$u(\boldsymbol{x_I}) = \{\boldsymbol{R}(\boldsymbol{x_I})^T, \boldsymbol{p}(\boldsymbol{x_I})^T\}\, \boldsymbol{G}^{-1} \begin{Bmatrix} \boldsymbol{u_s} \\ 0 \end{Bmatrix} = \varphi(\boldsymbol{x_I})\, \boldsymbol{u_s} \qquad \text{Eq. (4.23)}$$

The interpolation function of the interest point $\boldsymbol{x_I}$ is then defined by

$$\varphi(\boldsymbol{x_I}) = \{\boldsymbol{R}(\boldsymbol{x_I})^T, \boldsymbol{p}(\boldsymbol{x_I})^T\}\, \boldsymbol{G}^{-1} = \{\varphi_1(\boldsymbol{x_I}), \varphi_2(\boldsymbol{x_I}), \ldots, \varphi_n(\boldsymbol{x_I})\} \qquad \text{Eq. (4.24)}$$

The weak Galerkin form depends on the partial derivative of $\varphi(\boldsymbol{x_I})$. Thus, to be able to calculate the partial derivatives of the interpolated field function, it is necessary to obtain the respective RPI shape functions partial derivatives. Hence, for a 3D problem, the partial derivative of $\varphi(\boldsymbol{x_I})$ can be established as,

$$\varphi_{,x}(\boldsymbol{x_I}) = \{\boldsymbol{R}(\boldsymbol{x_I})^T \ \boldsymbol{p}(\boldsymbol{x_I})^T\}_{,x} \boldsymbol{G}^{-1} \quad \text{Eq. (4.25)}$$

$$\varphi_{,y}(\boldsymbol{x_I}) = \{\boldsymbol{R}(\boldsymbol{x_I})^T \ \boldsymbol{p}(\boldsymbol{x_I})^T\}_{,y} \boldsymbol{G}^{-1} \quad \text{Eq. (4.26)}$$

$$\varphi_{,z}(\boldsymbol{x_I}) = \{\boldsymbol{R}(\boldsymbol{x_I})^T \ \boldsymbol{p}(\boldsymbol{x_I})^T\}_{,z} \boldsymbol{G}^{-1} \quad \text{Eq. (4.27)}$$

Complementarily, for the same 3D problem, the first order partial derivative of the RBF vector is defined by,

$$\boldsymbol{R}(\boldsymbol{x_I})_{,x} = \{R_1(\boldsymbol{x_I})_{,x} \ R_2(\boldsymbol{x_I})_{,x} \ \ldots \ R_{\boldsymbol{n}}(\boldsymbol{x_I})_{,x}\}^T = \left\{\frac{\partial R_1(\boldsymbol{x_I})}{\partial x} \ \frac{\partial R_2(\boldsymbol{x_I})}{\partial x} \ \ldots \ \frac{\partial R_{\boldsymbol{n}}(\boldsymbol{x_I})}{\partial x}\right\}^T \quad \text{Eq. (4.28)}$$

$$\boldsymbol{R}(\boldsymbol{x_I})_{,y} = \{R_1(\boldsymbol{x_I})_{,y} \ R_2(\boldsymbol{x_I})_{,y} \ \ldots \ R_{\boldsymbol{n}}(\boldsymbol{x_I})_{,y}\}^T = \left\{\frac{\partial R_1(\boldsymbol{x_I})}{\partial y} \ \frac{\partial R_2(\boldsymbol{x_I})}{\partial y} \ \ldots \ \frac{\partial R_{\boldsymbol{n}}(\boldsymbol{x_I})}{\partial y}\right\}^T \quad \text{Eq. (4.29)}$$

$$\boldsymbol{R}(\boldsymbol{x_I})_{,z} = \{R_1(\boldsymbol{x_I})_{,z} \ R_2(\boldsymbol{x_I})_{,z} \ \ldots \ R_{\boldsymbol{n}}(\boldsymbol{x_I})_{,z}\}^T = \left\{\frac{\partial R_1(\boldsymbol{x_I})}{\partial z} \ \frac{\partial R_2(\boldsymbol{x_I})}{\partial z} \ \ldots \ \frac{\partial R_{\boldsymbol{n}}(\boldsymbol{x_I})}{\partial z}\right\}^T \quad \text{Eq. (4.30)}$$

where the partial derivates of the MQ-RBF in order to *x*, *y* and *z* are obtained by,

$$\frac{\partial R_i(x_I)}{\partial x} = -2\mathrm{p}\left({d_{iI}}^2 + c^2\right)^{p-1}(x_i - x_I) \quad \text{Eq. (4.31)}$$

$$\frac{\partial R_i(x_I)}{\partial y} = -2\mathrm{p}\left({d_{iI}}^2 + c^2\right)^{p-1}(y_i - y_I) \qquad \text{Eq. (4.32)}$$

$$\frac{\partial R_i(x_I)}{\partial z} = -2\mathrm{p}\left({d_{iI}}^2 + c^2\right)^{p-1}(z_i - z_I) \qquad \text{Eq. (4.33)}$$

The RPI functions are dependently related to the distribution of propagation nodes and are linearly independent in the influence-domain. Additionally, these correspond to interpolation functions that possess Kronecker delta property δ_{ij} (Eq. (4.34)) which enables the direct imposition of the essential boundary conditions in the stiffness matrix.

$$\varphi_i(\boldsymbol{x}_j) = \delta_{ij} = \begin{cases} 1\,(i = j) \\ 0\,(i \neq j) \end{cases} \quad i, j = 1, \ldots, n \qquad \text{Eq. (4.34)}$$

Furthermore, the partition of unity is satisfied

$$\sum_{\mathrm{i}=1}^{n} \varphi_i(\boldsymbol{x_i}) = 1 \qquad \text{Eq. (4.35)}$$

If the interpolation function $\varphi(\boldsymbol{x_I})$ possesses reproduction properties and the constant of the polynomial basis is further included, then it can be established

$$\sum_{\mathrm{i}=1}^{n} \varphi_i(\boldsymbol{x_i}) x_i = \boldsymbol{x} \qquad \text{Eq. (4.36)}$$

under condition that the first order monomial is added in the polynomial basis.

4.3. Solid Mechanics

The continuum mechanics corresponds to the cornerstone of nonlinear numerical analysis. Solids and structures that are subject to loads or forces are under stress. These stresses lead to strains, which consequently can be interpreted as deformations or relative displacements [10]. Within the framework of continuum solid mechanics, the basic theory is generally based on two foundations: (1) the basic laws of motion describing the equilibrium of a continuum body subject to external loadings and induced internal forces, being valid for all continuum bodies, and (2) a constitutive theory describing the mechanical behaviour of the materials used for the construction of a continuum body. Some of the material parameters that constitute the resulting equations can be determined from experiments [121].

In the present section, the mechanical fundamentals behind the numerical applications presented in this work are outlined. Initially, the applied continuum formulation is addressed, in which the solid kinematics and the constitutive equations used are demonstrated. Subsequently, the applied weak form and the consequent generated discrete equation system are presented.

4.3.1. Kinematics (Stress and Strain Fields, and Equilibrium Equations)

Solid mechanics involves a study of the principal relationships between stress and strain and stress and displacements in a given solid and boundary condition (external forces and displacement constraints). Thus, according to the structural configuration of each solid material and its characteristics, these can present distinct behaviours, depending on the respective stress-strain curve. Solids can be considered linear elastic, in which the relationship between stress and strain is assumed to be linear. In these materials, the deformation caused by loading disappears entirely after the total removal of that load, i.e., the solid returns to its initial shape. In contrast, in plastic materials occurs a residual deformation that remains even after the total removal of the applied load. Complementarily, materials can be classified as anisotropic and isotropic. In the first, the material property varies as a function of direction, and thus, the deformation caused by a load applied in a given direction does not correspond to the same deformation caused by the same load but in a different direction. In isotropic materials (which correspond to a

particular case of anisotropic materials), it is necessary to know about two independent material properties, Young's modulus (E) and Poisson's ratio (ν).

Therefore, when analysing a deformation that consequently causes a change in the body configuration, it is defined by the stress and strain terms. These terms allow to express the virtual work as an integral over the known body volume and thereby show the respective change in configuration. It is essential to ensure that both the stress tensor and the strain tensor refer to the same deformed state. In order to represent the stresses of the current configuration, the Cauchy stress tensor, $\mathbf{\Lambda}$, which corresponds to a symmetric tensor, is defined by Eq. (4.37) and (4.38), for the 2D and 3D cases, respectively.

$$\mathbf{\Lambda} = \begin{bmatrix} \sigma_{xx} & \sigma_{xy} \\ \sigma_{yx} & \sigma_{yy} \end{bmatrix} \quad \text{Eq. (4.37)}$$

$$\mathbf{\Lambda} = \begin{bmatrix} \sigma_{xx} & \sigma_{xy} & \sigma_{xz} \\ \sigma_{yx} & \sigma_{yy} & \sigma_{yz} \\ \sigma_{zx} & \sigma_{zy} & \sigma_{zz} \end{bmatrix} \quad \text{Eq. (4.38)}$$

Employing the Voigt notation, it is possible to obtain a reduced representation of the stress tensor, $\boldsymbol{\sigma}$, expressing tensors in column vectors, represented in Eq. (4.39) and (4.40), for the 2D and 3D cases, respectively.

$$\boldsymbol{\sigma} = \{\sigma_{xx} \quad \sigma_{yy} \quad \sigma_{xy}\}^T \quad \text{Eq. (4.39)}$$

$$\boldsymbol{\sigma} = \{\sigma_{xx} \quad \sigma_{yy} \quad \sigma_{zz} \quad \sigma_{xy} \quad \sigma_{yz} \quad \sigma_{zx}\}^T \quad \text{Eq. (4.40)}$$

Additionally, the strain tensor $\boldsymbol{E}$ to the strain vector $\boldsymbol{\varepsilon}$, is established in Eq. (4.41) and (4.42), for the 2D and 3D cases, respectively.

$$\boldsymbol{\varepsilon} = \{\varepsilon_{xx} \quad \varepsilon_{yy} \quad \varepsilon_{xy}\}^T \quad \text{Eq. (4.41)}$$

$$\boldsymbol{\varepsilon} = \{\varepsilon_{xx} \quad \varepsilon_{yy} \quad \varepsilon_{zz} \quad \varepsilon_{xy} \quad \varepsilon_{yz} \quad \varepsilon_{zx}\}^T \qquad \text{Eq. (4.42)}$$

In this work, only linear elastic isotropic materials are considered. Therefore, the relation between stress and strain in the solid domain is provided by the constitutive equation, known as Hooke's Law,

$$\boldsymbol{\sigma} = \mathbf{c}\,\boldsymbol{\varepsilon} \qquad \text{Eq. (4.43)}$$

where **c** corresponds to the constitutive matrix, given by $\boldsymbol{c} = \boldsymbol{s}^{-1}$, with $\boldsymbol{s}$ being the compliance elasticity matrix, containing the material characteristics where the elements on matrix $\boldsymbol{s}$ are obtained through experimental tests. For a 3D anisotropic material case, matrix $\boldsymbol{s}$ can be defined by,

$$\mathbf{s} = \begin{bmatrix} \frac{1}{E_{xx}} & -\frac{\nu_{yx}}{E_{yy}} & -\frac{\nu_{zx}}{E_{zz}} & 0 & 0 & 0 \\ -\frac{\nu_{xy}}{E_{xx}} & \frac{1}{E_{yy}} & -\frac{\nu_{zy}}{E_{zz}} & 0 & 0 & 0 \\ -\frac{\nu_{xz}}{E_{xx}} & -\frac{\nu_{yz}}{E_{yy}} & \frac{1}{E_{zz}} & 0 & 0 & 0 \\ 0 & 0 & 0 & \frac{1}{G_{xy}} & 0 & 0 \\ 0 & 0 & 0 & 0 & \frac{1}{G_{yz}} & 0 \\ 0 & 0 & 0 & 0 & 0 & \frac{1}{G_{zx}} \end{bmatrix} \qquad \text{Eq. (4.44)}$$

in which E_{ii} is the Young's modulus in direction I, ν_{ij} corresponds to the Poisson ratio that characterizes the deformation rate in direction j when a force is applied in direction i and G_{ij} is the shear modulus that characterizes the variation angle between directions i and j. However, due to the symmetry, the following relation can be established,

$$E_i\,\nu_{ji} = E_j\,\nu_{ij} \qquad \text{Eq. (4.45)}$$

Complementarily, for the 2D case, considering the plane stress assumptions (where $\sigma_{zx} = \sigma_{zy} = \sigma_{zz} = 0$) and the plane strain deformation theory (where $\varepsilon_{zx} = \varepsilon_{zy} = \varepsilon_{zz} = 0$), matrix $\boldsymbol{s}$ is obtained by Eq. (4.46) and (4.47), respectively.

$$\mathbf{s}_{\,plane\ stress} = \begin{bmatrix} \frac{1}{E_{xx}} & -\frac{\nu_{yx}}{E_{yy}} & 0 \\ -\frac{\nu_{xy}}{E_{xx}} & \frac{1}{E_{yy}} & 0 \\ 0 & 0 & \frac{1}{G_{xy}} \end{bmatrix} \qquad \text{Eq. (4.46)}$$

$$\mathbf{s}_{\,plane\ strain} = \begin{bmatrix} \frac{1}{E_{xx}} - \frac{\nu_{zx}\nu_{xz}}{E_{xx}} & -\frac{\nu_{yx}}{E_{yy}} - \frac{\nu_{zx}\nu_{yz}}{E_{yy}} & 0 \\ -\frac{\nu_{xy}}{E_{xx}} - \frac{\nu_{zy}\nu_{xz}}{E_{xx}} & \frac{1}{E_{yy}} - \frac{\nu_{zy}\nu_{yz}}{E_{yy}} & 0 \\ 0 & 0 & \frac{1}{G_{xy}} \end{bmatrix} \qquad \text{Eq. (4.47)}$$

Regarding the displacement field in the 3D case, consisting of $\boldsymbol{u} = \{u, v, w\}$, the strain components can be obtained from the derivatives of the displacement field, according to the following equations,

$$\begin{aligned} \varepsilon_{xx} &= \frac{\partial u}{\partial x} \\ \varepsilon_{yy} &= \frac{\partial v}{\partial y} \\ \varepsilon_{zz} &= \frac{\partial w}{\partial z} \\ \varepsilon_{xy} &= \frac{\partial u}{\partial y} + \frac{\partial v}{\partial x} \\ \varepsilon_{xz} &= \frac{\partial u}{\partial z} + \frac{\partial w}{\partial x} \\ \varepsilon_{yz} &= \frac{\partial v}{\partial z} + \frac{\partial w}{\partial y} \end{aligned} \qquad \text{Eq. (4.48)}$$

Thus, the strain vector can be obtained by combining a partial differential operator, $\boldsymbol{L}$, and the displacement field, $\boldsymbol{u}$,

$$\boldsymbol{\varepsilon} = \boldsymbol{L}\,\boldsymbol{u} \qquad \text{Eq. (4.49)}$$

with $\boldsymbol{L}$ being,

$$\boldsymbol{L} = \begin{bmatrix} \frac{\partial}{\partial x} & 0 & 0 & \frac{\partial}{\partial y} & 0 & \frac{\partial}{\partial z} \\ 0 & \frac{\partial}{\partial y} & 0 & \frac{\partial}{\partial x} & \frac{\partial}{\partial z} & 0 \\ 0 & 0 & \frac{\partial}{\partial z} & 0 & \frac{\partial}{\partial y} & \frac{\partial}{\partial x} \end{bmatrix}^T \qquad \text{Eq. (4.50)}$$

Ultimately, for an infinitesimal element, the equilibrium equations for a 3D example can be defined as,

$$\begin{aligned} \frac{\partial \sigma_{xx}}{\partial x} + \frac{\partial \sigma_{xy}}{\partial y} + \frac{\partial \sigma_{xz}}{\partial z} + F_x = 0 \\ \frac{\partial \sigma_{xy}}{\partial x} + \frac{\partial \sigma_{yy}}{\partial y} + \frac{\partial \sigma_{yz}}{\partial z} + F_y = 0 \\ \frac{\partial \sigma_{xz}}{\partial x} + \frac{\partial \sigma_{yz}}{\partial y} + \frac{\partial \sigma_{zz}}{\partial z} + F_z = 0 \end{aligned} \qquad \text{Eq. (4.51)}$$

in which F_x, F_y, F_z are the body forces applied to the element along the Cartesian axis.

4.3.2. Weak Form

The strong form consists of the partial differential system equations governing the studied physic phenomenon and the boundary conditions. By applying this formulation, the exact solution is always obtained. However, it becomes difficult to impose the essential boundary conditions, since the governing equation is satisfied at all the nodes in

the internal domain and the boundary condition is satisfied at every boundary node [96]. Therefore, this approach becomes very rigid and sometimes is not workable during execution, especially in complex practical engineering problems [96]. On the other hand, formulations based on weak forms produce stable algebraic systems of equations and can give a discretized system of equations in order to obtain the approximate solution of the problem. The discrete equation system is established for each integration point, meaning that the precision and accuracy of the obtained solution depend on the number of nodes in which the problem domain is discretised. Additionally, it becomes easier to impose the boundary conditions by applying them directly at the nodes [10].

4.3.2.1. Galerkin Weak Form

The Galerkin weak form is used to convert the differential equations into a discrete equation system. This corresponds to a variational formulation based on energy minimization. Therefore, considering a solid body represented in Figure 4.9, characterized by a domain $\Omega \in \mathbb{R}^2$ and bounded by Γ, in which $\Gamma \in \Omega$: $\Gamma_u \cup \Gamma_t = \Gamma \wedge \Gamma_u \cap \Gamma_t = \emptyset$, being Γ_u the essential boundary and Γ_t the natural boundary, the equilibrium equations governing the linear elasto-static problem can be established by,

$$\nabla \boldsymbol{\Lambda} + \boldsymbol{b} = 0 \qquad \text{Eq. (4.52)}$$

where ∇ is the divergence operator, $\boldsymbol{b}$ corresponds to the body force per unit volume and $\boldsymbol{\Lambda}$ the Cauchy stress tensor, as defined previously. The natural boundary respects the condition $\boldsymbol{\Lambda}\,\boldsymbol{n} = \bar{\boldsymbol{t}}$ on Γ_t, where $\boldsymbol{n}$ is the unit outward normal to the boundary of domain Ω and $\bar{\boldsymbol{t}}$ the traction on the natural boundary Γ_t. Whereas the essential boundary condition is $\boldsymbol{u} = \bar{\boldsymbol{u}}$, being $\bar{\boldsymbol{u}}$ the prescribed displacement on the essential boundary Γ_u.

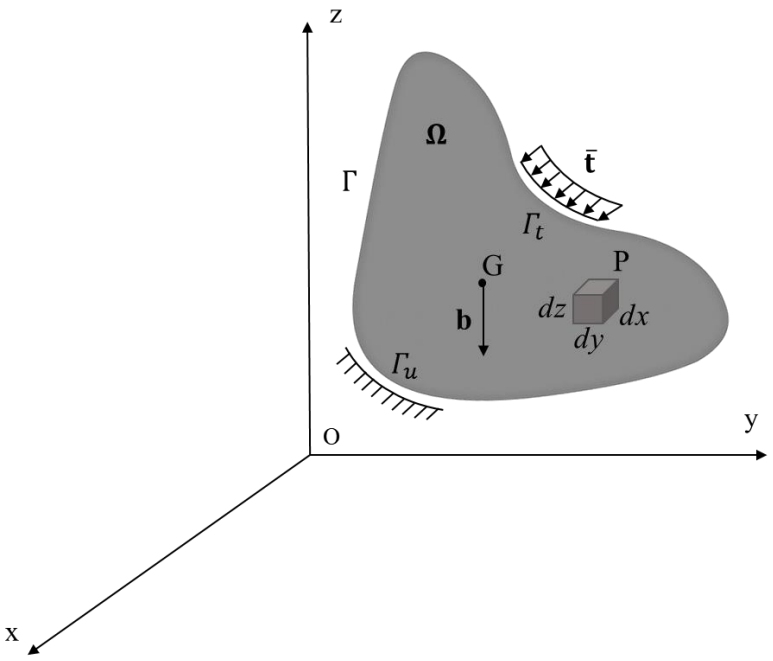

Figure 4.9- Continuous solid subjected to volume forces and external forces. Adapted from [10].

Employing the Galerkin weak form, the real solution is the one that minimizes the Lagrangian functional, L, established by,

$$L = T - U + W_f \qquad \text{Eq. (4.53)}$$

in which T is the kinetic energy, U is the strain energy and W_f is the work performed by external forces. The Lagrangian functional, L, possesses all the physical information concerning the system and the forces acting on it.

The energy terms of Eq. (4.53) are obtained by,

$$T = \frac{1}{2}\int_{\Omega} \rho\, \dot{\boldsymbol{u}}^T \dot{\boldsymbol{u}}\; d\Omega \qquad \text{Eq. (4.54)}$$

$$U = \frac{1}{2}\int_{\Omega} \boldsymbol{\varepsilon}^T \boldsymbol{\sigma}\, d\Omega \qquad \text{Eq. (4.55)}$$

$$W_f = \int_{\Omega} \boldsymbol{u}^T \boldsymbol{b}\, d\Omega + \int_{\Gamma_t} \boldsymbol{u}^T\, \bar{\boldsymbol{t}}\, d\Gamma_t \qquad \text{Eq. (4.56)}$$

where the solid volume is defined by Ω, $\dot{\boldsymbol{u}}$ is the displacement first derivative with respect to time, ρ is the solid mass density, $\boldsymbol{\varepsilon}$ and $\boldsymbol{\sigma}$ are the strain and stress vectors, respectively, $\boldsymbol{u}$ is the displacement, $\boldsymbol{b}$ the body forces and Γ_t the traction boundary where the external forces $\bar{\boldsymbol{t}}$ are applied.

Consequently, the Galerkin weak form can be obtained by substituting Eq. (4.54), (4.55) and (4.56) in Eq. (4.53) as follows,

$$L = \frac{1}{2} \int_{\Omega} \rho\, \dot{\boldsymbol{u}}^T \dot{\boldsymbol{u}}\; d\Omega - \frac{1}{2} \int_{\Omega} \boldsymbol{\varepsilon}^T \boldsymbol{\sigma}\, d\Omega + \int_{\Omega} \boldsymbol{u}^T \boldsymbol{b}\, d\Omega + \int_{\Gamma_t} \boldsymbol{u}^T\, \bar{\boldsymbol{t}}\, d\Gamma_t \qquad \text{Eq. (4.57)}$$

The equation (4.57) was subsequently minimized,

$$\delta \int_{t_1}^{t_2} \left[\frac{1}{2} \int_{\Omega} \rho\, \dot{\boldsymbol{u}}^T \dot{\boldsymbol{u}}\; d\Omega - \frac{1}{2} \int_{\Omega} \boldsymbol{\varepsilon}^T \boldsymbol{\sigma}\, d\Omega + \int_{\Omega} \boldsymbol{u}^T \boldsymbol{b}\, d\Omega + \int_{\Gamma_t} \boldsymbol{u}^T\, \bar{\boldsymbol{t}}\, d\Gamma_t \right] dt = 0 \qquad \text{Eq. (4.58)}$$

The present work, as it encompasses only static problems, the dynamic part, i.e., the kinetic variation of energy, can be neglected. Moreover, the expression can be further simplified by moving the variation operator δ into each integral, such that,

$$\int_{t_1}^{t_2} \left[-\frac{1}{2} \int_{\Omega} \delta\, \boldsymbol{\varepsilon}^T \boldsymbol{\sigma}\, d\Omega + \int_{\Omega} \delta\, \boldsymbol{u}^T \boldsymbol{b}\, d\Omega + \int_{\Gamma_t} \delta\, \boldsymbol{u}^T\, \bar{\boldsymbol{t}}\, d\Gamma_t \right] dt = 0 \qquad \text{Eq. (4.59)}$$

Therefore, the integrand function in the first integral term can be rewritten as,

$$\delta\, (\boldsymbol{\varepsilon}^T \boldsymbol{\sigma}) = \delta \boldsymbol{\varepsilon}^T \boldsymbol{\sigma} + \boldsymbol{\varepsilon}^T \delta \boldsymbol{\sigma} \qquad \text{Eq. (4.60)}$$

with $\boldsymbol{\varepsilon}^T \delta\boldsymbol{\sigma} = (\boldsymbol{\varepsilon}^T \delta\boldsymbol{\sigma})^T = \delta\boldsymbol{\sigma}^T \boldsymbol{\varepsilon}$. Employing the constitute equation (Hooke's Law), $\boldsymbol{\sigma} = \boldsymbol{c}\,\boldsymbol{\varepsilon}$, and the symmetric property of the material matrix, $\boldsymbol{c}^T = \boldsymbol{c}$, it is possible to establish,

$$\delta\boldsymbol{\sigma}^T \boldsymbol{\varepsilon} = \delta(\boldsymbol{c}\,\boldsymbol{\varepsilon})^T \boldsymbol{\varepsilon} = \delta\boldsymbol{\varepsilon}^T \boldsymbol{c}^T \boldsymbol{\varepsilon} = \delta\boldsymbol{\varepsilon}^T \boldsymbol{c}\,\boldsymbol{\varepsilon} = \delta\boldsymbol{\varepsilon}^T \boldsymbol{\sigma} \qquad \text{Eq. (4.61)}$$

Consequently, Eq. (4.60) becomes,

$$\delta\,(\boldsymbol{\varepsilon}^T \boldsymbol{\sigma}) = 2\delta\boldsymbol{\varepsilon}^T \boldsymbol{\sigma} \qquad \text{Eq. (4.62)}$$

Using Equation (4.59), it can be established,

$$-\int_{\Omega} \delta\,\boldsymbol{\varepsilon}^T \boldsymbol{\sigma}\, d\Omega + \int_{\Omega} \delta\,\boldsymbol{u}^T \boldsymbol{b}\, d\Omega + \int_{\Gamma_t} \delta\,\boldsymbol{u}^T\,\bar{\boldsymbol{t}}\, d\Gamma_t = 0 \qquad \text{Eq. (4.63)}$$

Additionally, considering the stress-strain relation, $\boldsymbol{\sigma} = \boldsymbol{c}\,\boldsymbol{\varepsilon}$, and the stress-displacement relation, $\boldsymbol{\varepsilon} = \boldsymbol{L}\,\boldsymbol{u}$, the expression of Eq. (4.63) can be rearranged as follows,

$$\int_{\Omega} (\delta\boldsymbol{L}\boldsymbol{u})^T\, \boldsymbol{c}(\boldsymbol{L}\boldsymbol{u})\, d\Omega - \int_{\Omega} \delta\,\boldsymbol{u}^T \boldsymbol{b}\, d\Omega - \int_{\Gamma_t} \delta\,\boldsymbol{u}^T\,\bar{\boldsymbol{t}}\, d\Gamma_t = 0 \qquad \text{Eq. (4.64)}$$

which corresponds to the generic Galerkin weak form written in terms of displacement, applied to static problems.

4.3.3. Discrete Equation System

The discrete equation system for meshless methods can be determined based on the principle of virtual work, using the meshless shape functions as trial and test functions. For this, the Galerkin weak form, which is established in Eq. (4.64), combined with the interpolation functions, can be applied. Recalling Eq. (4.1),

$$\boldsymbol{u}(\boldsymbol{x_I}) = \sum_{j=1}^{n} \varphi_j(\boldsymbol{x}_I)\, \boldsymbol{u}(\boldsymbol{x_i}) \qquad \text{Eq. (4.65)}$$

Therefore, the virtual displacements of the nodes inside the influence-domains in RPIM of an interest point $\mathbf{x_I}$, will cause a virtual displacement of the integration point, which can be interpolated or approximated considering,

$$\delta\boldsymbol{u}(\boldsymbol{x_I}) = \sum_{j=1}^{n} \varphi_j(\boldsymbol{x}_I)\, \delta\boldsymbol{u}_j \qquad \text{Eq. (4.66)}$$

Combining Eq. (4.1) and Eq. (4.64) with Eq. (4.66), it can be defined,

$$-\int_{\Omega}\left(\sum_{j=1}^{n}\varphi_j(\boldsymbol{x}_I)\,\delta\boldsymbol{u}_j\right)^{T}\boldsymbol{L}^{T}\,\boldsymbol{c}\,\boldsymbol{L}\left(\sum_{j=1}^{n}\varphi_j(\boldsymbol{x}_I)\,\boldsymbol{u}_j\right)d\Omega + \int_{\Omega}\left(\sum_{j=1}^{n}\varphi_j(\boldsymbol{x}_I)\,\delta\boldsymbol{u}_j\right)^{T}\boldsymbol{b}\,d\Omega + \int_{\Gamma_t}\left(\sum_{j=1}^{n}\varphi_j(\boldsymbol{x}_I)\,\delta\boldsymbol{u}_j\right)^{T}\bar{\boldsymbol{t}}\;d\Gamma_t = 0 \qquad \text{Eq. (4.67)}$$

The previous equation can be rewritten in matrix form by eliminating the summations. Thus, for the 3D case, the matrix of approximation/interpolation functions for the interest point $\boldsymbol{x_I}$, is established by,

$$\varphi(\boldsymbol{x_I}) = \begin{bmatrix} \varphi_1(\boldsymbol{x_I}) & 0 & 0 & \varphi_2(\boldsymbol{x_I}) & 0 & 0 & \dots \varphi_n(\boldsymbol{x_I}) & 0 & 0 \\ 0 & \varphi_1(\boldsymbol{x_I}) & 0 & 0 & \varphi_2(\boldsymbol{x_I}) & 0 & \dots & 0 & \varphi_n(\boldsymbol{x_I}) & 0 \\ 0 & 0 & \varphi_1(\boldsymbol{x_I}) & 0 & 0 & \varphi_2(\boldsymbol{x_I}) & \dots & 0 & 0 & \varphi_n(\boldsymbol{x_I}) \end{bmatrix} \quad \text{Eq. (4.68)}$$

Eq. (4.66) can be rewritten as follows,

$$\delta \boldsymbol{u}^T \int_\Omega [(\varphi(\boldsymbol{x_I}))^T \boldsymbol{L}^T]\, \boldsymbol{c}[\boldsymbol{L}\varphi(\boldsymbol{x_I})]\, d\Omega \boldsymbol{u} - \delta \boldsymbol{u}^T \int_\Omega \left(\varphi_j(\boldsymbol{x_I})\right)^T \boldsymbol{b}\, d\Omega - \delta \boldsymbol{u}^T \int_{\Gamma_t} \left(\varphi_j(\boldsymbol{x_I})\right)^T \bar{\boldsymbol{t}}\, d\Gamma_t = 0 \quad \text{Eq. (4.69)}$$

where $\boldsymbol{u}$ represents the nodal displacement vector of all n nodes within the influence-domain, which can be expressed as,

$$\boldsymbol{u} = \{u_1, v_1, w_1, u_2, v_2, w_2, \dots, u_n, v_n, w_n\}^T \quad \text{Eq. (4.70)}$$

Recalling the partial differential operator matrix, $\boldsymbol{L}$, the deformability matrix, $\boldsymbol{B}$, for the interest point $\mathbf{x_I}$, can be defined as the multiplication between $\boldsymbol{L}$ and $\varphi(\boldsymbol{x_I})$,

$$\boldsymbol{B}(\boldsymbol{x_I}) = \boldsymbol{L}\varphi(\boldsymbol{x_I}) = \begin{bmatrix} \frac{\partial \varphi_j(\boldsymbol{x_I})}{\partial x} & 0 & 0 & \frac{\partial \varphi_j(\boldsymbol{x_I})}{\partial y} & 0 & \frac{\partial \varphi_j(\boldsymbol{x_I})}{\partial z} \\ 0 & \frac{\partial \varphi_j(\boldsymbol{x_I})}{\partial y} & 0 & \frac{\partial \varphi_j(\boldsymbol{x_I})}{\partial x} & \frac{\partial \varphi_j(\boldsymbol{x_I})}{\partial z} & 0 \\ 0 & 0 & \frac{\partial \varphi_j(\boldsymbol{x_I})}{\partial z} & 0 & \frac{\partial \varphi_j(\boldsymbol{x_I})}{\partial y} & \frac{\partial \varphi_j(\boldsymbol{x_I})}{\partial x} \end{bmatrix}_j^T \quad \text{Eq. (4.71)}$$

being $= 1,2,3, \dots, n,$, for the order of nodes constituting the influence-domain.

Thus, the matrix $\boldsymbol{B}(\boldsymbol{x_I})$ is composed of all n matrices, $\boldsymbol{B_j}(\boldsymbol{x_I})$, one for each node in the influence-domain.

Finally, Eq. (4.69) is redefined by replacing $\boldsymbol{L}\varphi(\boldsymbol{x_I})$ by $\boldsymbol{B}(\boldsymbol{x_I})$,

$$\delta \boldsymbol{u}^T \left[\int_\Omega \left(\boldsymbol{B}(\boldsymbol{x_I})\right)^T \boldsymbol{c}\boldsymbol{B}(\boldsymbol{x_I})\, d\Omega \mathbf{u} - \int_\Omega \left(\varphi_j(\boldsymbol{x_I})\right)^T \boldsymbol{b}\, d\Omega - \int_{\Gamma_t} \left(\varphi_j(\boldsymbol{x_I})\right)^T \bar{\boldsymbol{t}}\, d\Gamma_t \right] = 0 \quad \text{Eq. (4.72)}$$

Resulting in,

$$\underbrace{\int_{\Omega} \left(\boldsymbol{B}(\boldsymbol{x_I})\right)^T \boldsymbol{c}\boldsymbol{B}(\boldsymbol{x_I})\, d\Omega \boldsymbol{u}}_{\mathbf{K}} - \underbrace{\int_{\Omega} \left(\varphi_j(\boldsymbol{x_I})\right)^T \boldsymbol{b}\, d\Omega}_{\boldsymbol{f_b}} - \underbrace{\int_{\Gamma_t} \left(\varphi_j(\boldsymbol{x_I})\right)^T \bar{\boldsymbol{t}}\, d\Gamma_t\, x}_{\boldsymbol{f_t}} = 0 \qquad \text{Eq. (4.73)}$$

which gives the global static equilibrium equation, $\boldsymbol{K}\,\boldsymbol{u} = \boldsymbol{f_b} + \boldsymbol{f_t}$. The first integral of Eq. (4.73) corresponds to the global stiffness matrix, $\boldsymbol{K}$, the other two integrals correspond to the body forces vector, $\boldsymbol{f_b}$ and the external forces vector, $\boldsymbol{f_t}$, respectively, and can be assembled into the global force vector, $\boldsymbol{f} = \boldsymbol{f_b} + \boldsymbol{f_t}$. After assembly, the global discrete equation system is obtained,

$$\boldsymbol{K}\,\boldsymbol{u} = \boldsymbol{f} \;\Rightarrow\; \boldsymbol{u} = \boldsymbol{K}^{-1}\,\boldsymbol{f} \qquad \text{Eq. (4.74)}$$

being $\boldsymbol{u}$ the displacement field.

Thenceforward, several variable fields can be determined. The strain, $\boldsymbol{\varepsilon}(\boldsymbol{x_I})$, in an interest point $\boldsymbol{x_I} \in \Omega$ can be obtained using Eq. (4.49). Subsequently, employing Hooke's Law present in Eq. (4.43), the stress field, $\boldsymbol{\sigma}(\boldsymbol{x_I})$, can be obtained.

Considering both the strain and the stress fields, the strain energy density (SED) for an interest point $\boldsymbol{x_I}$ and a specific load case can be determined by,

$$U(\boldsymbol{x_I}) = \frac{1}{2}\int_{\boldsymbol{\Omega_I}} \boldsymbol{\sigma}(\boldsymbol{x_I})^T\, \boldsymbol{\varepsilon}(\boldsymbol{x_I})\, d\Omega_I \qquad \text{Eq. (4.75)}$$

The principal stresses $\boldsymbol{\sigma}(\boldsymbol{x_I})$ for the interest point $\boldsymbol{x_I}$ are determined from the Cauchy stress tensor $\boldsymbol{\Lambda}(\boldsymbol{x_I})$ employing the following expression,

$$det\left(\begin{bmatrix}\sigma_{xx} & \sigma_{xy} & \sigma_{xz}\\ \sigma_{yx} & \sigma_{yy} & \sigma_{yz}\\ \sigma_{zx} & \sigma_{zy} & \sigma_{zz}\end{bmatrix} - \boldsymbol{\sigma}(\boldsymbol{x_I})\begin{bmatrix}1 & 0 & 0\\ 0 & 1 & 0\\ 0 & 0 & 1\end{bmatrix}\right) = 0 \qquad \text{Eq. (4.76)}$$

and the principal directions $\boldsymbol{n}((\boldsymbol{x_I})_i) = \left\{n_x((\boldsymbol{x_I})_i), n_y((\boldsymbol{x_I})_i)\right\}^T$ can be obtained with,

$$\left(\begin{bmatrix}\sigma_{xx} & \sigma_{xy} & \sigma_{xz}\\ \sigma_{yx} & \sigma_{yy} & \sigma_{yz}\\ \sigma_{zx} & \sigma_{zy} & \sigma_{zz}\end{bmatrix} - \boldsymbol{\sigma}(\boldsymbol{x_I})\begin{bmatrix}1 & 0 & 0\\ 0 & 1 & 0\\ 0 & 0 & 1\end{bmatrix}\right)\begin{Bmatrix}n_x(\boldsymbol{x_I})_i\\ n_y(\boldsymbol{x_I})_i\\ n_z(\boldsymbol{x_I})_i\end{Bmatrix} = 0 \qquad \text{Eq. (4.77)}$$

Hence, the von Mises effective stress for each interest point $\boldsymbol{x_I}$ is obtained from the three principal stresses according to the following expression,

$$\bar{\sigma}(\boldsymbol{x_I}) = \sqrt{\frac{1}{2}\left((\boldsymbol{\sigma}(\boldsymbol{x_I})_1 - \boldsymbol{\sigma}(\boldsymbol{x_I})_2)^2 + (\boldsymbol{\sigma}(\boldsymbol{x_I})_2 - \boldsymbol{\sigma}(\boldsymbol{x_I})_3)^2 + (\boldsymbol{\sigma}(\boldsymbol{x_I})_3 - \boldsymbol{\sigma}(\boldsymbol{x_I})_1)^2\right.} \qquad \text{Eq. (4.78)}$$

4.4. Bone Remodelling Algorithm

Over time, several mathematical models have been proposed and developed which assume that the mechanical stimulus, described by stress and/or strain measures, acts as the main driving force in the bone remodelling process. Thus, these mathematical formulations encompass the relationship between bone functional adaptation and the induced stress (or strain), considering bone as a local adaptive material. However, experimental studies have shown that functional adaptation in response to mechanical stimulation is a complex process and that, consequently, a detailed description of these processes is ambitious. Nevertheless, several investigators have developed models in order to numerically predict the local remodelling reactions observed in experiments using appropriate bone growth laws, such as those presented in section 2.3.

Thus, the bone remodelling algorithm adopted in the present work was developed by Belinha and co-workers [10] and is an adaptation for meshless methods of the model proposed by Carter [122]. Therefore, in this section, the respective iterative remodelling algorithm is presented, in which the bone tissue is assumed to be an isotropic material, but the algorithm also supports orthotropic materials.

4.4.1. Model Description

The remodelling model uses a bone remodelling nonlinear equation adapted to work with the FEM and meshless methods, namely RPIM and NNRPIM. The expression can be presented as a differential equation, where a temporal-spatial based functional, $\rho_{app}(x,t)$: $\mathbb{R}^{d+1} \longmapsto \mathbb{R}$, discretized along the temporal one-dimension and the spatial d-dimensions, is minimized with respect to time,

$$\frac{\partial \rho_{app}(x,t)}{\partial t} \cong \frac{\Delta \rho_{app}(x,t)}{\Delta t} = \left(\rho_{app}^{model}\right)_{t_j} - \left(\rho_{app}^{model}\right)_{t_{j+1}} = 0 \qquad \text{Eq. (4.79)}$$

Any problem analysed must be discretised in space and time. Therefore, it can be assumed that the d-dimensional spatial domain is discretized into N nodes: $\boldsymbol{X} = \{\boldsymbol{x}_1, \boldsymbol{x}_2, \dots, \boldsymbol{x}_N\} \in \Omega$, leading to Q interest points: $\boldsymbol{Q} = \{\boldsymbol{x}_1, \boldsymbol{x}_2, \dots, \boldsymbol{x}_Q\} \in \Omega$ being $\boldsymbol{x_i} \in \mathbb{R}^d$ and $\boldsymbol{Q} \cap \boldsymbol{X} = \emptyset$. The temporal domain is discretised in iterative fictitious time steps $t_j \in \mathbb{N}$, with $j \in \mathbb{N}$. Thus, the medium apparent density for the complete model domain is established by $\left(\rho_{app}^{model}\right)_{t_j}$ at a fictitious time t_j. Consequently, within the same iterative step, the medium apparent density of the model ρ_{app}^{model}, can be obtained by,

$$\rho_{app}^{model} = Q^{-1} \sum_{i=1}^{Q} \left(\rho_{app}\right)_i \qquad \text{Eq. (4.80)}$$

being $\left(\rho_{app}\right)_i$ the infinitesimal apparent density on the interest point $\boldsymbol{x}_I$ defined by $\rho_I = g(\sigma_I)$. Since in the present work, the material's behaviour was assumed isotropic, following the algorithm proposed by Belinha and co-workers [10], the value of ρ_I is established according to the ultimate compression stress in the axial direction, σ_{axial}^{c}. On the other hand, the apparent density can be determined according to the von Mises effective stress, $\bar{\sigma}(\boldsymbol{x_I})$, for each interest point $\boldsymbol{x_I}$, instead of considering the σ_{axial}^{c}. Hence, for Lotz's material law, Eq. (2.5) can be rewritten as

$$\bar{\sigma}_i = a_3 \cdot (\rho_{app})^{a_4} \quad \text{Eq. (4.81)}$$

where the values of the coefficients a_3 and a_4 are present in Table 2.1 depending on the type of bone i under analysis. Similarly, for Belinha's material law, Eq. (2.9) is redefined such that,

$$\bar{\sigma} = \sum_{j=0}^{3} d_j \cdot \rho^j \quad \text{Eq. (4.82)}$$

in which the value of the coefficient d_j is present in Table 2.2.

However, considering that the remodelling process will not occur in all the interest points $\boldsymbol{x_I}$, but only in the interest points that contain the SED values belonging to the interval expressed in Eq. (4.83). Therefore, these are selected by the algorithm and subjected to the density remodelling process, while all the other interest points maintain the previous density.

$$U(\boldsymbol{x_I}) \in [U_{min}, U_{min} + \alpha \cdot \Delta U[\cup]U_{max} - \beta \cdot \Delta U, U_{max}], \quad \forall U(\boldsymbol{x_I}) \in \mathbb{R} \quad \text{Eq. (4.83)}$$

where $U_{min} = \min(U)$, $U_{max} = \max(U)$ and $\Delta U = U_{max} - U_{min}$, and the parameters α and β define the growth rate and the decay rate of the apparent density, respectively, varying with the problem under analysis. Given that Eq. (4.82) corresponds to a third order equation, it returns three different solutions, ρ_1, ρ_2 and ρ_3. Thus, if the interest points belong to the decay apparent density interval, the apparent density at the interest point $\boldsymbol{x_I}$ is defined by $\rho_I = \max(\rho_1, \rho_2, \rho_3)$.

Ultimately, the remodelling equilibrium is achieved when,

$$\frac{\Delta\rho}{\Delta t} = 0 \quad \vee \quad \left(\rho_{app}^{model}\right)_{t_j} = \rho_{app}^{control} \quad \text{Eq. (4.84)}$$

4.4.2. Remodelling Procedure

In the present section, the bone remodelling algorithm used in this work is described in detail. For the implementation of the iterative remodelling process, a forward Euler scheme was designed, as illustrated in Figure 4.10.

In a first instance, the algorithm is initialized with the pre-processing of the available medical images. Subsequently, the problem domain is discretized into an unstructured nodal mesh $\boldsymbol{X} \in \boldsymbol{\Omega}$, the nodal connectivity is established, and the background integration mesh is constructed, according to the numerical method chosen by the user (the FEM, the RPIM or the NNRPIM). Then, the initial material properties are allocated to the respective domain areas, being these isotropic, as mentioned above. Thus, it is possible to determine the shape functions for each integration point, $\varphi(\boldsymbol{x}_I)$, following the process explained in the previous sections. Additionally, the essential and natural boundary conditions are also imposed.

From this moment, the iterative remodelling algorithm is initiated. In the first step of the iterative loop, an elasto-static analysis of the problem is performed in order to determine the principal directions of the stress field. Thus, it is possible to align the material constitutive matrix $\boldsymbol{c}$ of each interest point $\boldsymbol{x}_I$ with the principal direction $\boldsymbol{n}((\boldsymbol{x}_I)_1)$ of the respective maximum principal stress $\sigma(\boldsymbol{x}_I)_1$ obtained in each interest point.

Subsequently, at each iterative step, a mechanical analysis is always performed for each fictitious time instant t_j. In addition, all load cases l ($k = 1, 2, \ldots, l$) are sequentially and separately analysed. Using the deformation matrix $\boldsymbol{B}(\boldsymbol{x}_I)$ and the constitutive material matrix $\boldsymbol{c}(\boldsymbol{x}_I)$, the local stiffness matrix, $\boldsymbol{K}_I$, is established for each integration point $\boldsymbol{x}_I$. At the end of this process, all the constructed local stiffness matrices $\boldsymbol{K}_I$ are further assembled into a global stiffness matrix, $\boldsymbol{K}$. Additionally, the presented remodelling algorithm allows the simultaneous application of several load cases. Thus, the essential boundaries corresponding to the load case k are imposed in the stiffness matrix, $\boldsymbol{K}_j^k$, and the force vectors of each load case k are considered, $\boldsymbol{f}_j^k$, allowing to build the equation system, $\boldsymbol{K}_j^k \, \boldsymbol{u}_j^k = \boldsymbol{f}_j^k$. Through the obtained displacement field, $\boldsymbol{u}_j^k$, the stress, $\boldsymbol{\sigma}_j^k$, and strain, $\boldsymbol{\varepsilon}_j^k$, fields can be determined. Moreover, the SED (strain energy density), $\boldsymbol{U}_j^k$, the von Mises effective stress, $\bar{\boldsymbol{\sigma}}_j^k$, fields, and the principal stresses and

directions, $\boldsymbol{\sigma}(\boldsymbol{n})_j^k$ and $\boldsymbol{n}_j^k$, can be derived from the stress and strain fields, for any interest point $\boldsymbol{x}_I$. Therefore, the variable fields obtained for each load case can be established using Eq. (4.85).

$$\{\boldsymbol{u}_j, \boldsymbol{\varepsilon}_j, \boldsymbol{\sigma}_j, \boldsymbol{\sigma}(\boldsymbol{n})_j, \boldsymbol{n}_j, \bar{\boldsymbol{\sigma}}_j, \boldsymbol{U}_j\} \sum_{\mathrm{k=1}}^{l} \frac{m^{(k)}\{\boldsymbol{u}_j, \boldsymbol{\varepsilon}_j, \boldsymbol{\sigma}_j, \boldsymbol{\sigma}(\boldsymbol{n})_j, \boldsymbol{n}_j, \bar{\boldsymbol{\sigma}}_j, \boldsymbol{U}_j\}}{\sum_{\mathrm{s=1}}^{l} m^{(s)}} \qquad \text{Eq. (4.85)}$$

According to Eq. (4.85), the final weighted variable field of step j is obtained with the superposition of the number of relevant discrete load cases, l, weighted in agreement with the corresponding number of load cycles, m.

Thus, each mechanical analysis is followed by bone tissue remodelling. The algorithm after selecting the integration points with SED values that belong to the interval expressed in Eq. (4.83), these are subjected to a density remodelling process, while all the other points maintain the previous density.

Then, considering the weighted effective stress field, the following iterative step involves an update of the apparent density of the selected interest points and consequently the material properties, using the material law chosen by the user (Lotz's or Belinha's laws, described in section 2.3). After establishing the new apparent density, the algorithm proceeds to the next iteration step.

Subsequently, the material constitutive matrix at each interest point is transformed, using a rotation matrix, considering the principal directions obtained in the previous iteration step. This procedure enables to align iteratively the material properties with the updated load path.

The algorithm continues to run until the condition present in Eq. (4.84), defined as the stop criterion, is achieved.

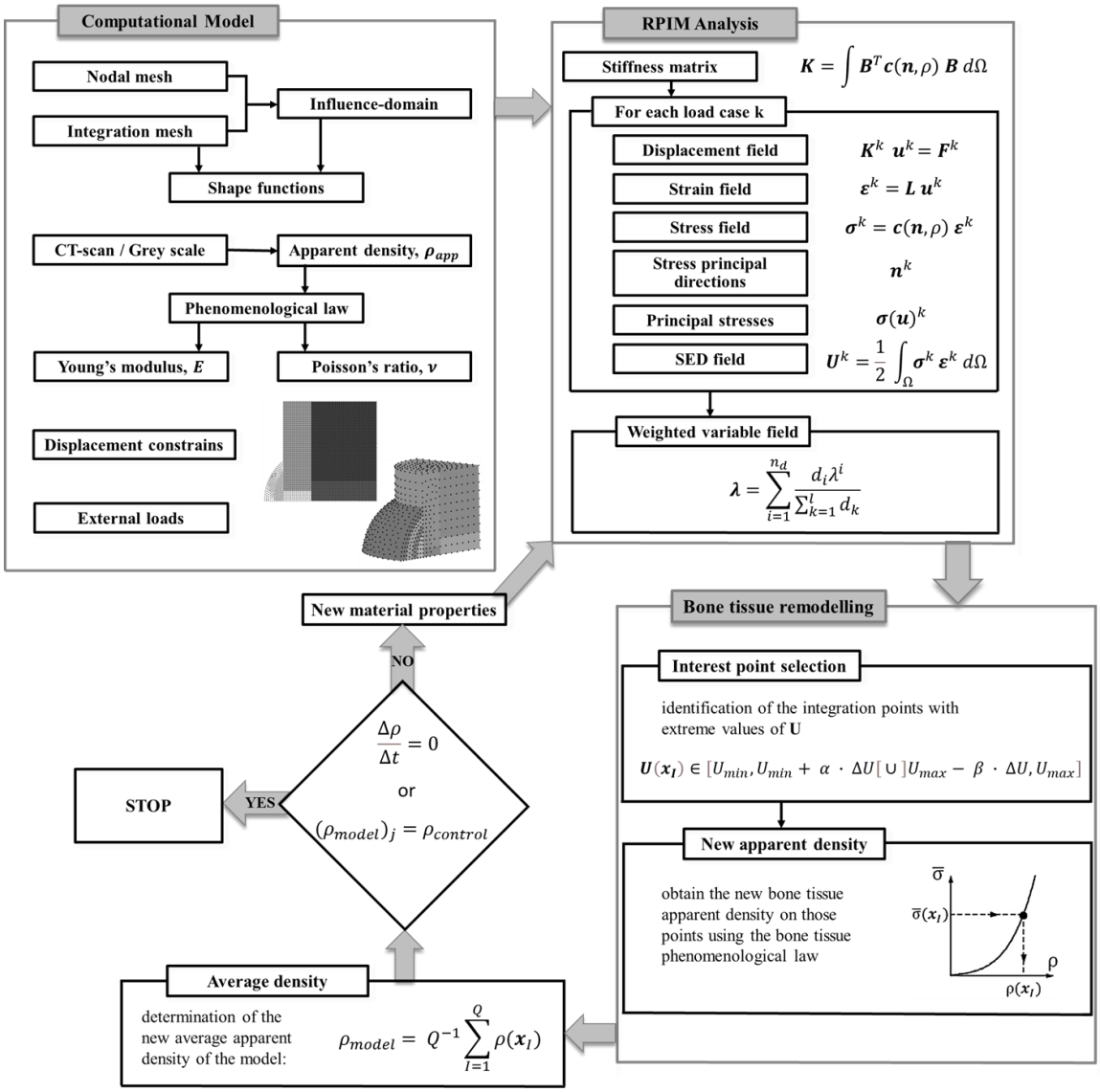

Figure 4.10- Bone remodelling algorithm.

The numerical examples in this work are presented as grey tone isomaps depicting the evolution of trabecular architecture, where the white colour represents the maximum apparent density, $\rho_0 = 2.1\ g/cm^3$, and the dark-grey colour represents the minimum apparent density, $\rho_0 = 0.1\ g/cm^3$. All the remaining intermediate grey tones represent transitional apparent densities, following a linear colour grey-scale gradient. To construct these maps, both the initial nodal mesh discretizing the problem and the respective integration mesh are used. As a consequence, the level of detail of these isomaps can be improved by increasing the mesh density, containing more nodes. However, the computational cost increases with the discretization level, and this algorithm is not

optimized for fast performances and therefore, in this work, medium dense nodal meshes are used.

CHAPTER 5 – MECHANOBIOLOGICAL MODELS OF BONE FRACTURE HEALING

5. Mechanobiological Models of Bone Fracture Healing

Mechanobiology is a new interdisciplinary area of scientific research that has recently emerged from the intersection of engineering and biology, exploring the influence of mechanical loads in regulating biological processes through signalling to cells. It is possible to observed tissue adaptation in response to changing mechanical stimulation in different tissue types and anatomical locations.

Since mechanobiology entails cell-driven responses by tissues and organs to loading, it is an inherently multiscale field of study, required translation of loading that occurs at the entire organ scale to the mechanical stimulation of individual cells. Similarly, this stimulation of cells is a combination of solid and fluid stimulation, since biological tissues contain and are surrounded by interstitial fluid. At the core of mechanobiology comes a response of cells within the tissue due to mechanical forces. In fact, it has been proven that in basic cellular functions like mitosis and migration, the forces that eukaryotic cells exert on their surrounding tissues are fundamental, even in the absence of any external mechanical stimulus [123]–[125]. Thus, it has been proposed that all cells are mechanosensitive, through the use of specific molecule or protein complexes known as mechanosensors, broadly organised into three types: attachments between individual cells, such as stretch-activated gap junctions; structures on the cell membrane that can deform under fluid flow, such as primary cilia and, attachments between the membrane and the extracellular matrix, such as focal adhesions [123], [126]. In these particular cases, a mechanical stimulus is transmitted from the whole bone level to an external cellular feature and, therefore, to the cytoskeleton or cytoplasm to induce a biochemical cascade. This process is known as mechanotransduction, or the way by which the cells sense and respond to mechanical forces, adapting their macroscale biological structures and processes [127].

In a particular way, the study of mechanobiology is quite significant in bone, which is an adaptive material that employs a complex biological system of remodelling in response to mechanical stimulation. Although the bone healing process has been studied experimentally for several decades [65], [128]–[130], experimental work involves real scenarios and requires very controlled conditions, state-of-the-art equipment, high precision and cost, and is often confounded by other factors, such as unknown subjects' backgrounds, comorbidities, and genetic variation [131].

Thus, due to the complexity of bone fracture healing and the limitations mentioned above, purely experimental approaches are incapable of fully describe the underlying biochemical and biomechanical mechanisms leading to fracture healing [4]. Therefore, given the nature and difficulty of experimental work to investigate and predict bone adaptation, researchers have turned to computational models to clarify the stimulation that these cells are subjected to *in vivo* and to determine mechanobiological rules for these adaptive responses. Computational modelling has increasingly grown in bone mechanobiology, stimulating the development of this field, and is recognised as a powerful tool in terms of mechanical interactions at the cellular scale, as well as for the prediction of important resulting tissue-level phenomena, such as cell proliferation and differentiation, tissue growth, adaptation, and maintenance [132]. These models can be an important tool for the design, optimisation and prediction of final outcomes in future treatment strategies.

More recently mechanobiological models have been used to investigate the role of various mechanical and biological factors in fracture healing [4], [133]. Modelling in mechanobiology is based on local mechanical variables that stimulate cellular expression for the regulation of tissue composition, density or structure, including force application at the boundary, force transmission through the tissue matrix, mechanosensation and transduction by cells, and transformation of extracellular matrix characteristics. These variables can be combined and represented by parameters and mathematical relationships in a finite element (FE) model. Additionally, some can be known or then measured, e.g., morphology, mechanical tissue properties, external loading characteristics, while others have to be estimated. Mechanical factors such as stress, strain, pressure, stability, and fluid velocity are important parameters that act as stimuli for tissue formation during bone healing. In these models, mechanical factors at fracture sites are mostly estimated using FE analysis. Thus, mechanical stimulus, biological factors, and chemical stimulus will influence biological processes and cellular activities, such as MSC, tissue differentiation, angiogenesis, and growth factor secretion, which in turn influence and regulate the bone healing process [133]. Using FE models with models describing these activities, the processes are simulated adaptively (Figure 5.1).

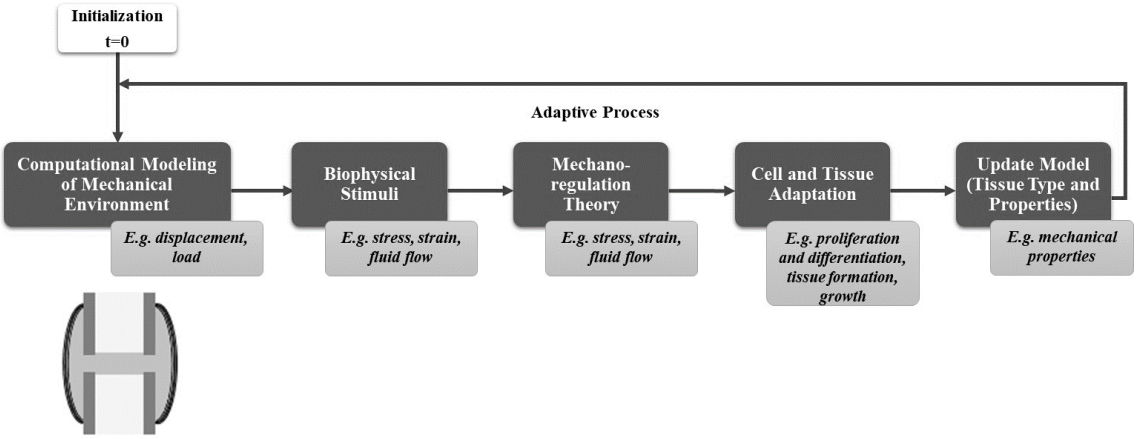

Figure 5.1 – Schematic representation of a general adaptive mechanobiological model of bone healing.

Typically, *in silico* bone mechanobiology has adopted two-pronged investigations: the first related to mechanoregulation algorithms to predict mechanobiological changes in bone tissue, and the second to models investigating cell mechanobiology. The mechanoregulation algorithms are constituted at the macroscale level of loading and do not consider the mechanosensitivity of the bone cells themselves and, therefore, some of the limitations of modelling cell mechanobiology correspond to both the experimental and imaging techniques, as well as the small scales involved. However, *in silico* modelling makes it possible to gather new information that comes from experimental work.

5.1. Tissue Differentiation Models

5.1.1. Early Theories

Theories on the relationship between mechanics and biology were originally proposed in relation to fracture healing [134]. In particular, like all musculoskeletal tissues, bone originates from MSCs through the process of tissue differentiation. In this regard, these theories later evolved into "mechanobioregulatory algorithms", which encompass a finite set of rules governing the effects of mechanical loading on stem cells and tissues [134]. An essential aspect in these algorithms is the modelling of cellular processes such as cell dispersion, proliferation, apoptosis, etc.

In 1960, Friedrich Pauwels pioneered mechanobiological thinking in the context of bone healing, developing the first theory to propose differentiation into various tissues based on mechanical stimulation, through mechanical tissue deformation [1]. Taking into consideration the different mechanical performance of tissues formed during healing, Pauwels suggested that tissues maintained distinct mechanical stressing. Cartilage would form under conditions of hydrostatic pressure, as it resists volume changes. In contrast, fibrous tissues are more suited to resist shape changes and would form under shear stresses. Therefore, primary bone formation requires a stable, low-stress mechanical environment and will proceed only after a soft tissue has stabilised the environment, allowing MSCs to differentiate into osteoblasts, leading to bone formation (Figure 5.2(a)). Pauwels' theory was based on clinical observation and logic, however there were no means to measure or calculate the tissue stresses or strains in detail.

Subsequently, the “Interfragmentary Strain Theory” was developed by Perren and Cordey from a qualitative analysis of clinical results of fracture healing [65]. A model was proposed based on the premise that only tissues that can withstand the strain in the gap without failure can be formed in the fracture gap, i.e., based on the upper limits of interfragmentary strain to predict fracture gap closure. Consequently, there is a gradual stiffening of the fracture callus, reducing the strain in the callus, with the formation of stiffer tissues with higher strain tolerance. Perren showed that lamellar bone would rupture under a strain of 2%, cartilage would rupture for a strain of about 10%, while granulation tissue can resist strains up to 100% (Figure 5.2(b)). Bone healing occurs by a progressive tissue differentiation from the initial granulation tissue, to fibrous tissue, cartilaginous tissue and then bony tissue. Therefore, there is a feedback between a stiffening of the callus and a lowering of the strain, resulting a hard callus made of bone, which undergoes remodelling during the final stage of healing.

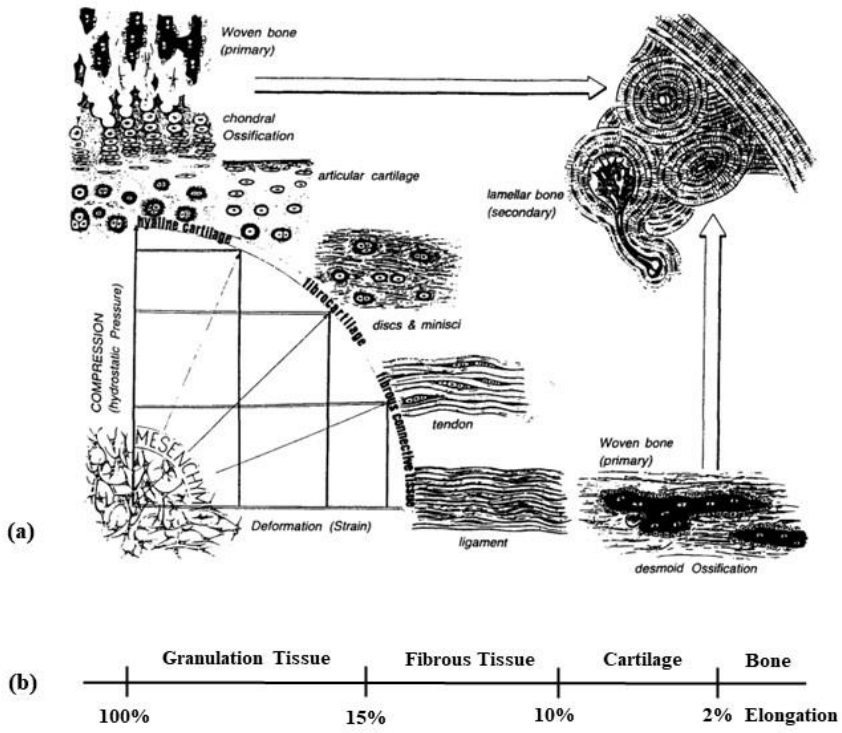

Figure 5.2 – Schematic representation of the first two mechano-regulatory models. (a) Model developed by Pauwels, showing the hypothesised influence of biophysical stimuli on tissue phenotype. On the x axis is represented the shape deformation (i.e., shear) and on the y axis the hydrostatic pressure. The combination of these biophysical stimulus, shear and hydrostatic pressure, will act on the mesenchymal cells leading to either hyaline cartilage, fibrocartilage or fibrous connective tissue as represented on the perimeter of the quadrant. The larger arrows indicate that, as time passes, ossification of these soft tissues occurs, provided that the soft tissue has stabilised the environment. (b) Perren and Cordey's idea related to the elongation that each tissue type can tolerate. Adapted from [65], [135].

Additionally, Goodship and Kenwright, suggested that interfragmentary motion could accelerate healing, through experimental evidence [136], leading to a large body of research to delineate the effects of different types of interfragmentary loading [137].

5.1.2. Single Phase Models

Based on the work carried out by Pauwels, Carter et al. [138], [139], proposed a model to explain how mechanical loading guides cell differentiation in a fracture callus, more particularly the influence of cyclic multiaxial stresses on endochondral growth and ossification, expanding the concepts related to tissue differentiation to mechanical load over time. Through the developed work it was possible to realize that: (i) a history of compressive hydrostatic stress guides the formation of cartilaginous matrix components;

(ii) a history of tensile strain guides connective tissue cells in their production and turnover of fibrous matrix components; (iii) fibrocartilage is formed when a history of tissue loading consists of a combination of high levels of hydrostatic compressive stress and high levels of tensile strain; (iv) direct bone formation is allowed in regions not exposed to neither significant compressive hydrostatic stress nor significant tensile strain, provided there is an adequate blood supply and, finally, pre-osseous tissue can be diverted down a chondrogenic pathway in regions of low oxygen tension [134].

Carter et al. were the first to employ FEA to explore the relationships between local stress/strain levels and differentiated tissue types. By applying this model, they modelled the tissue in the callus as a single solid (linear elastic) phase, investigating endochondral ossification during fracture healing, as well as a developing joint and tissue differentiation around orthopaedic implants (Figure 5.3(a)) [139]. The model predicted realistic tissue patterns consistent with biological observations, but without quantification of the magnitude of mechanical stimulus with tissue formation. Also, Carter's studies highlighted the importance of a good blood supply for bone formation, since a poor blood supply promotes cartilaginous tissue formation. The mechanobiological model has been used to study oblique fractures [140], pseudoarthrosis formation [141], asymmetric fractures [142] and distraction osteogenesis [143]. However, none of the studies predicted tissue differentiation as an adaptive process over time.

On the other hand, Claes and Heigele established certain thresholds for the local stress and strain magnitudes to determine whether endochondral or intramembranous ossification takes place [144]. An interdisciplinary study was conducted comparing data from animal experiments, cell cultures and FEA to assess the influence of gap size and interfragmentary strain on bone healing [7], [145]. The developed FE model properly predicted tissue differentiation in the callus at three phases of the healing process, through the validation by histological images from *in vivo* experiments. Intramembranous ossification was assigned for strains less than $\pm 5\%$ and hydrostatic pressures less than ± 0.15 MPa and for endochondral bone formation for strains less than $\pm 15\%$ and compressive pressures greater than -0.15 MPa (Figure 5.3(b)). It is possible to form connective and fibrous tissues with larger mechanical stimuli. This algorithm was also combined with other rules of bone healing, applying an iterative FE model controlled by ‘fuzzy logic’ to investigate bone fracture healing [146]. In order to successfully simulate the main healing fracture patterns, the rules were based on cell culture experiments and

histological investigations, specifically incorporating vascularity. Additionally, were also used by Simon et al. [147] to investigate differences between shear and axial stimulation, and by Shefelbine et al. [148] to study trabecular bone fracture healing.

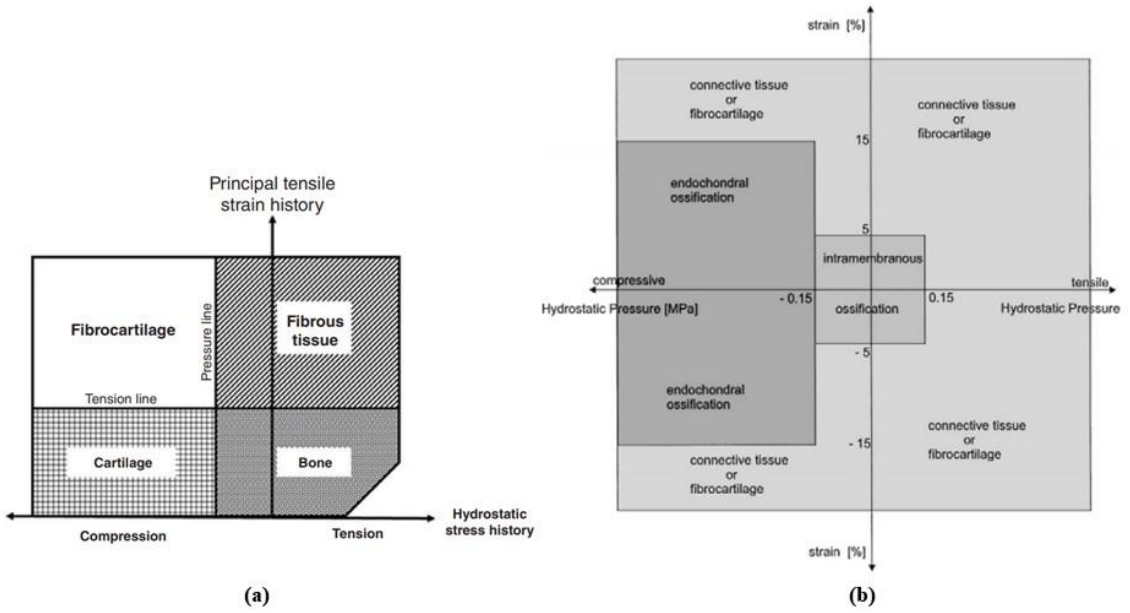

Figure 5.3 – Schematic representation of (a) mechanobiological model based on tensile strain and hydrostatic pressure as proposed by Carter et al. and (b) fracture healing model proposed by Claes and Heigele, including threshold values for when each tissue type will form. Reprinted from [139], [144].

5.1.3. Biphasic and Adaptive Models

A few years ago, biphasic and poroelastic FE formulations became available for modelling fluid-saturated solid materials. Since external loading is resisted by the linear combination of stress in the solid matrix and pressure of the fluid, the solid matrix deforms according to its elastic modulus and fluid flows at a rate proportional to the pressure gradient and the permeability, according to Darcy's Law. The solid and fluid components can be assumed to be incompressible, depending on the theoretical implementation, such that the rate of change of solid volume and fluid volume are equal, or the solid can be compressible while the fluid is incompressible. Thus, this type of formulation leads to a time-dependent behaviour of the material, as the fluid is extruded and redistributed within the solid matrix. The poroelastic formulation was originally proposed to model soil mechanics [149], and the biphasic formulation was proposed by

Mow to model cartilage behaviour [150]. Despite the slight differences have been shown similarly in outcomes [151].

As previously mentioned, tissue consists of cells and extracellular matrix, which is formed by fluid and fibres and has a time-dependent, viscous material behaviour. Thus, fluid flow is only created by dynamic loading [152]. Bone adaptation due to fluid velocity only occurs in response to dynamic, but not to static load [153].

Prendergast et al., developed a FE model to understand tissue differentiation around an orthopaedic implant and explore the influence of mechanical loading on cell differentiation [154], [155]. With this model it was possible to show that the biophysical stimulus experienced by the tissue at the implant interface were generated by both the tissue matrix and the drag force of the interstitial fluid flow. This indicated the need for dynamically loaded, biphasic models, because these effects could not be examined with static or linear elastic representations. Therefore, a biphasic FE model of poroelastic connective tissues was developed composed of two biophysical stimuli: octahedral shear strain in the solid phase (derived from the deviatoric part, contributes to shape distortion) and fluid velocity in the interstitial fluid phase as the mechanotransduction variables, where high magnitudes of either, favours fibrous tissue, and only when both stimuli are low enough, can ossification occur (Figure 5.4(a)).

Later, Isaksson et al. compared the mechanobiological models of Carter, Claes and Heigele, and Prendergast in a fracture healing study, and concluded that the concept based on shear strain and fluid velocity as stimuli correlated best with experimental results [156].

Therefore, over the last two decades, computational models have evolved from simple tools capable of analysing fracture healing at only one time point to current models that can predict tissue differentiation and remodelling over time.

Prendergast's model was adapted by Lacroix [157], [158] to describe fracture healing in a time-dependent manner in a 2D axisymmetric and 3D FE model. Their adaptive poroelastic model was able to simulate direct periosteal bone formation, endochondral ossification in the external callus, stabilisation when bridging of the external callus occurs, and resorption of the external callus (Figure 5.4(b)). This work involved the first biological reproductions, representing stem cell concentrations initially at the external boundaries and using a diffusive mechanism to collectively simulate cell

migration, proliferation and differentiation. Actual tissue differentiation depended on resulting cell concentration and stimulus. It was subsequently used for successful predictions of tissue differentiation in a rabbit bone chamber [159] and during osteochondral defects healing [160].

Although diffusion is not the mechanism of cell migration and proliferation, Lacroix's theory has contributed to many researchers to include cell activities in their mechano-regulatory algorithms.

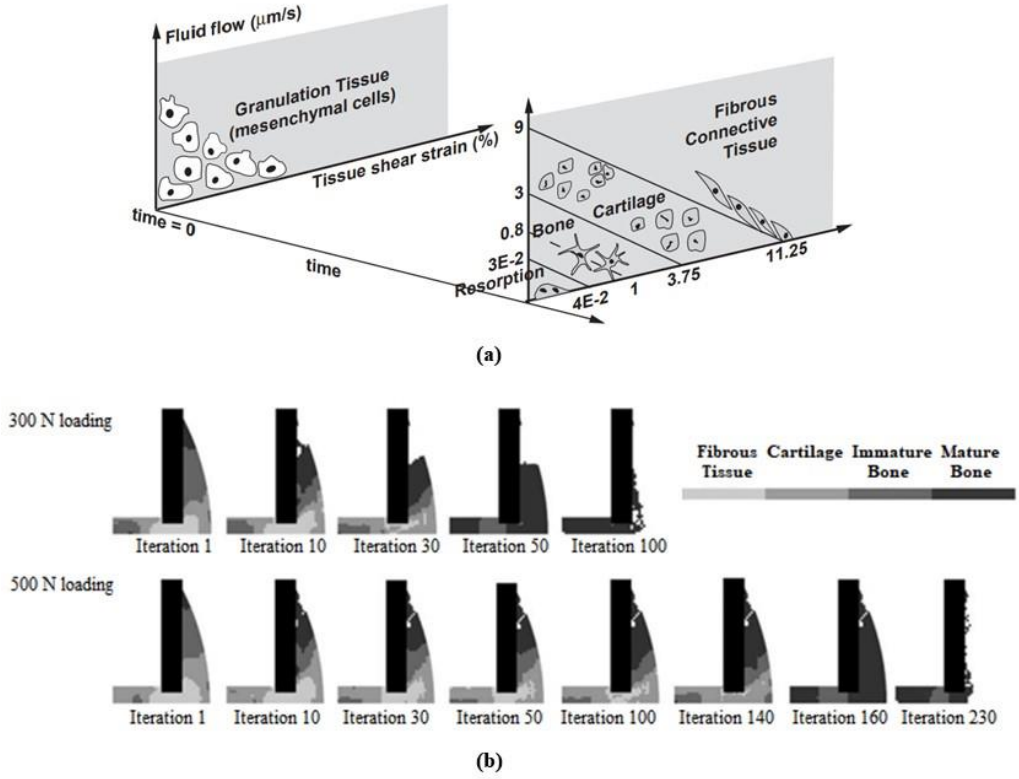

Figure 5.4 – Representation of (a) the tissue differentiation scheme proposed by Prendergast and Huiskes, where mesenchymal stem cells differentiate depending on the magnitudes of fluid velocity and tissue shear strain and (b) Lacroix and Prendergast implemented their model to predicted healing in a fracture callus. Both reprinted from Lacroix and Prendergast [154], [155], [157].

5.2. Tissue Growth/Morphology Models

Recently, the focus has been directed towards incorporating a more accurate description of cellular processes into the models. During the differentiation process, there is an adaptation of the musculoskeletal tissues and, particularly, the bone callus not only

changes in stiffness and cell density, but also tends to change shape. Overall, in bone healing simulations, either all or a subset of the four phases of the bone healing process (i.e., inflammation, soft callus, hard callus and remodelling) can be considered. However, some studies have focused on modelling only the soft callus or hard callus, using a predefined, fixed callus geometry in their simulation [161]–[164]. Additionally, callus resorption in the remodelling phase of the bone healing simulation is included in other studies, where they consider that there will be bone resorption and eventual callus resorption at the end of the bone healing simulation if the level of loading falls below a certain threshold [148], [157], [165], [166]. Therefore, this remodelling simulation algorithm does not include structure remodelling or directional mechanical properties in the bone, covering only the geometry.

Moreover, simulations of the early stages of bone healing and callus development are not frequently modelled [156], [167], [168], partly due to biological and chemical factors being much more significant at this stage than mechanical factors [4], [62]. Bone callus in its development has a transient nature, from the inflammatory phase to the soft callus formation phase, and has often been simulated through a volume expansion.

Almost all the studies described previously do not consider volumetric tissue growth, and there are few studies on bone growth in response to mechanical loading. In fact, the work developed by Isaksson et al. [156] was the first to include volumetric growth of individual tissue types into an adaptive FE model of distraction osteogenesis, expanding the algorithm of Prendergast et al. [155]. In this model, temporal and spatial tissue distributions during distraction osteogenesis, as well as known perturbations due to changes in distraction rate and frequency, were accurately predicted. Thus, the modelling of volumetric growth involved matrix production of each tissue type, and this was simulated based on the biphasic swelling model by Wilson et al. [169], with the application of a swelling pressure to the growing element and consequent volume expansion, reflecting an increase in matrix [156]. The predicted growth was similar to that observed experimentally.

On the other hand, in a more complex model, Garcia-Aznar et al. [170], simulated the process of tissue regulation and callus volumetric growth adaptively, considering different cellular events, such as mesenchymal-cell migration, and MSCs, chondrocyte, fibroblast, and osteoblast proliferation, differentiation and cell death, during the fracture healing process over time (Figure 5.5). Additionally, variables for matrix synthesis and

degradation were included, as well as for tissue damage, calcification, and remodelling, allowing an analysis of the main components that form the matrix of the different tissues (collagen types, proteoglycans, minerals and water) and, subsequently, determination of mechanical properties and permeability of the tissue. The stimulus they considered to regulate the process of tissue differentiation was the second invariant of the deviatoric strain tensor, and volumetric growth was modelled separately through a FE model based on thermal expansion and controlled by taking into account the amount of tissue production. The model predicted the increase in callus size with increasing interfragmentary movements.

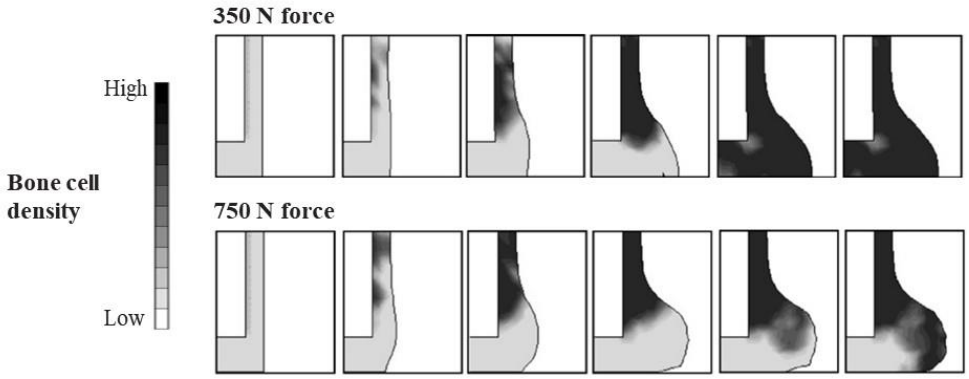

Figure 5.5 – Mechanoregulation model of callus growth developed by Garcia-Aznar et al., with the respective changes in shape and size in time for two load patterns. Adapted from [170].

5.3. Modelling of Biological Aspects

Computational mechanobiology has emerged to address tissue adaptation in response to loading, but accounting for the biological factors involved is still a challenge. In fact, vascularisation, nutrient supply and cellular proliferation are essential for bone regeneration. However, the mechanisms involving these processes to mechanical stimulation are still poorly understood.

Apart from the models described in the context of tissue growth, the studies mentioned above included a very limited description of cellular mechanisms. Lacroix and Prendergast [157], were the first to attempt to model these factors using a diffusion mechanism and, it was identified that the cell diffusion rate was the most critical to healing speed. Kelly and Prendergast [160], refined this model to include multiple cell

phenotypes, enabling individual elements to represent multiple tissue types. In this work, a FE model of a knee osteochondral defect was used to simulate the process of spontaneous repair. Therefore, bone formation was predicted through both endochondral and direct intramembranous ossification in the base of the defect, cartilage formation in the centre of the defect and fibrous tissue formation superficially. However, it is essential to emphasise that there are many cell and tissue types involved during bone healing, so the corresponding actual rates will vary for each modelled activity. Thus, despite the multiple mechanoregulation algorithms that have emerged trying to model bone regeneration, a better characterisation of these rates *in vivo* is still required in order to incorporate them into the models [165], [171].

5.3.1. Models Based on Biochemical Factors

Considering that biological modelling involves the regulation by biological and biochemical factors (such as growth factors, chemotaxis, or haptotaxis) of cellular activity and matrix synthesis, temporal and spatial systems of nonlinear partial differential equations (PDE) will enable a description of the change in the concentration and density of cells, ECMs, and growth factors [172], [173].

In fact, a mathematical study by Bailon-Plaza and van der Meulen emerged to explore the effects of growth factors, i.e., biochemical signals that are sent by cells in response to mechanical stimulation during fracture healing [172]. Using finite difference methods, sequential tissue regulation and cellular events were simulated by osteogenic and chondrogenic growth factors instead of mechanical loading, allowing a quantification of changes in both cell and matrix density, growth factor concentrations and characterisation of matrix synthesis and growth factor diffusion. Additionally, only the effects of haptotaxis on cell migration were considered.

On the other hand, Geris et al. expanded this formulation by adding chemotactic effects on cell activities and migration. In the simulation, it was shown that these effects and those of haptotaxis, improved bone healing and bone density distribution [173].

5.3.2. Models with Cell-phenotype Specific Activities

In 2008, to obtain more mechanistic modelling of cellular activities in bone healing, Isaksson et al. [174] developed the first model that directly links cellular phenotype to mechanical stimulation and also included four distinct cell types, such as MSCs, fibroblasts, chondrocytes, and osteoblasts. Thus, mechanical modulation of cell phenotype and skeletal tissue-type specific activities and rates was added, with the description of the corresponding spatial and temporal distributions of fibrous tissue, cartilage, and bone, regulated by the four cell types. These cells were able to migrate, proliferate, differentiate, or die, depending on both mechanical stimulation and the behaviour of adjacent cells at each time and location. This model enabled a correct prediction of the normal fracture healing process and experimentally delayed or non-union situations due to excessive loading or pathology, such as changes caused by periosteal stripping or impaired effects of cartilage remodelling during endochondral ossification (Figure 5.6) [174].

The parametric data used in this study were taken from the literature and, a factorial analysis was also performed in order to determine the most important cellular characteristics and their magnitudes in the bone healing process [175]. These were related to bone formation, cartilage production and degradation, which concerned the processes suggested as crucial biological steps in bone healing. The analyses revealed that healing was sensitive to parameters related to fibrous tissue and cartilage formation, indicating that some amounts of soft tissue production favour the healing process but too much of either tissue delayed bone formation [175]. It should be noted that two important processes during bone healing were not included in this work, such as biochemical signalling and vascularisation. The model only included angiogenesis implicitly in the regulatory function of cartilage degradation and endochondral replacement and, bone growth, i.e., the change in tissue volume, was neglected. Additionally, the modelling of cell activities was carried out on an element basis, and anisotropy in cell movement was not considered.

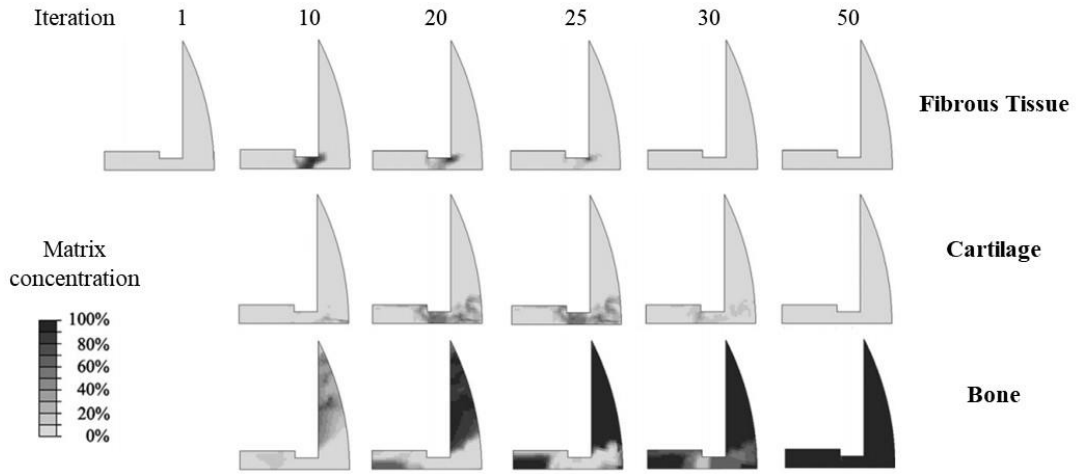

Figure 5.6 – Isaksson et al. model which incorporates cell-phenotype specific activities, simulating normal fracture healing with the spatial and temporal tissue densities of fibrous tissue, cartilage and bone. Adapted from [174].

5.3.3. Stochastic Cell Modelling

In previous studies, cell proliferation/migration has been modelled by considering it a diffusion mechanism, such as the models by Lacroix and Prendergast [157] and Bailon-Plaza and van der Meulen [161]. However, cells will disperse by crawling or proliferation, or are transported in a moving fluid, and therefore, diffusion does not represent the mechanism of cell dispersion [176]. Thus, using this model to simulate cell dispersal indicates that proliferation and migration tend to create a smooth variation in cell density, but such a restriction is not physiological [176].

Consequently, a new 2D FE lattice model representing both cells and extracellular matrix in the callus was developed by Perez and Prendergast [176]. A "random walk" model was included to represent cell migration both with and without a preferred direction, which implies anisotropic proliferation and migration of cells. The study involved a 2D simulation of a bone-implant interface using the stochastic cell model and the mechano-regulatory model by Prendergast et al. [155], in order to improve predictions and include a more irregular distribution of the tissue at the bone-implant interface. Furthermore, it was compared with the results of the diffusion model for cell migration, where the "random walk" model was able to predict a heterogeneous distribution, in contrast to the diffusion model, which showed a continuous one during tissue differentiation (Figure 5.7).

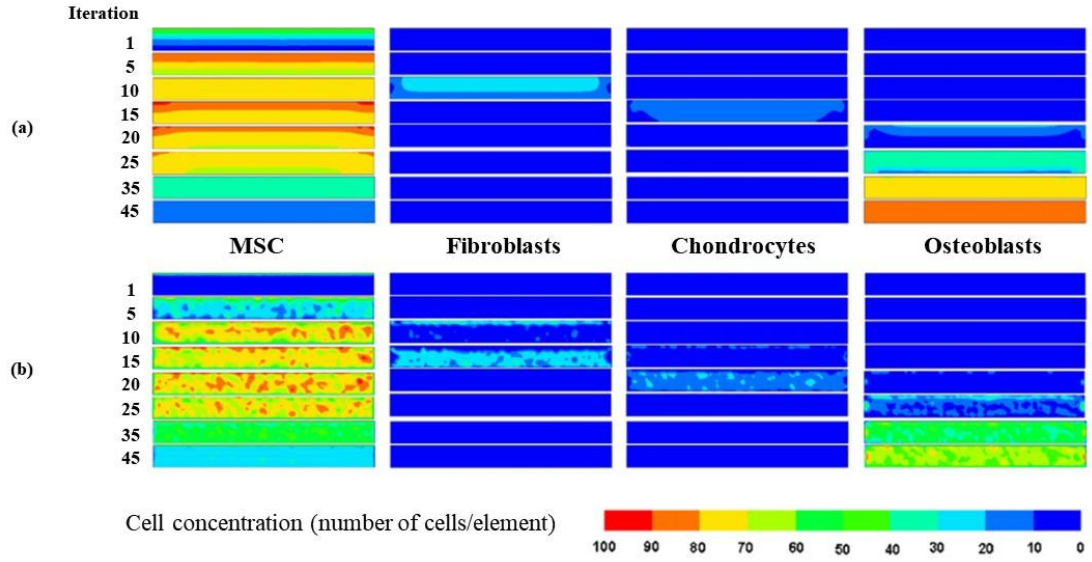

Figure 5.7 – Perez and Prendergast model with the predicted cell distribution at the bone/implant interface. (a) diffusion analysis and (b) "random walk" model. Adapted from [176].

Byrne et al. [158] adapted this model into 3D and later implemented it experimentally in fracture healing of a human tibia under muscle loading, predicting healing beyond the repair phase (Figure 5.8).

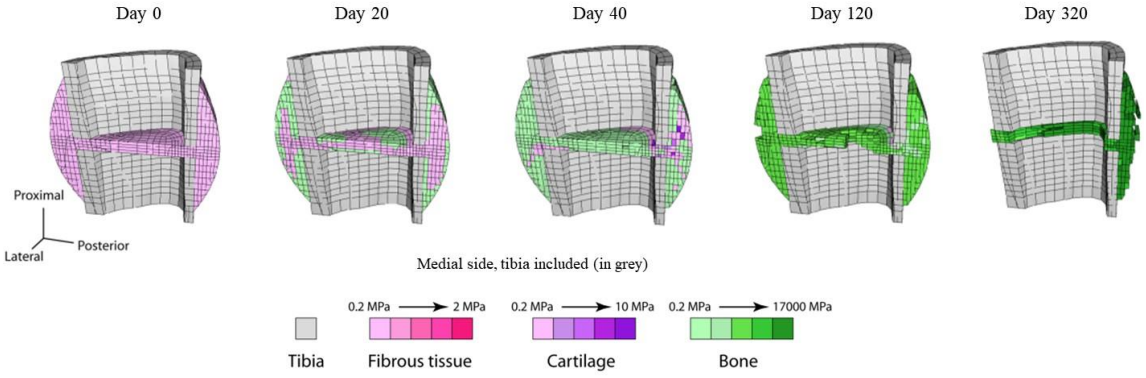

Figure 5.8 – Cross-sectional view of the healing patterns predicted over time in the Byrne et al. model, simulated in 3D based on stochastic cell modelling by Pérez and Prendergast. Adapted from [158].

5.3.4. Angiogenesis and Vascularization of the Tissue

Vascular supply is essential to provide nutrients and oxygen to bone cells, and therefore, angiogenesis, related to the in-growth of new blood vessels, is a critical factor

for bone healing. Local vascularity at the fracture site is one of the most considerable parameters influencing the bone healing process [177]. Angiogenesis has a central role in endochondral ossification, in which avascular cartilaginous tissue is gradually replaced by vascular bone tissue. A low oxygen environment favours cartilage formation, whereas bone formation is only possible in high oxygen environments [177].

Geris et al. [173], [178] expanded the bioregulatory model of bone regeneration by Bailon-Plaza and van der Meulen [172] in order to include angiogenesis. This process was simulated through the regulation of a growth factor and was compared with experimentally obtained results of normal fracture healing. However, oxygen diffusion was found to be restricted to a few hundred micrometres from the capillaries, showing the importance of the new vascular network morphology in the healing process. This work also allowed to simulate compromised healing situations related to impaired angiogenesis, from the reduction in vascular growth factor production by hypertrophic chondrocytes during fracture healing (Figure 5.9).

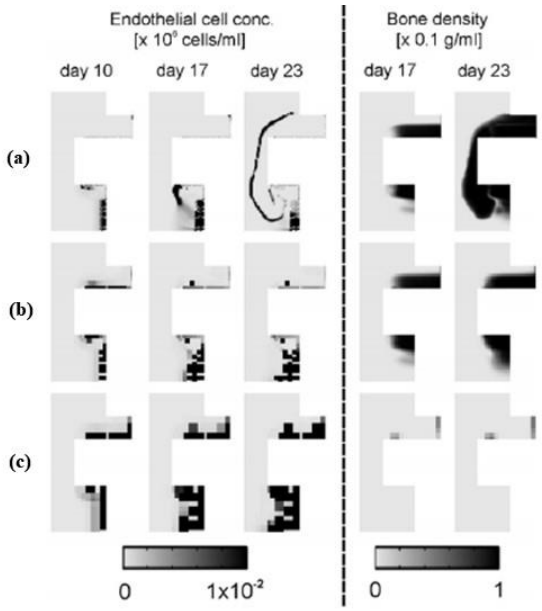

Figure 5.9 – Model by Geris et al. showing the influence of angiogenesis on fracture healing, represented by predicted endothelial cell concentration (left) and bone density (right) at several days post-fracture. (a) Reduced production (10% of the reference value) of vascular growth factor by hypertrophic chondrocytes will cause a very slow invasion of the cartilage matrix by endothelial cells and intramembranous ossification is not affected. After 5 weeks healing was successful through endochondral ossification, with bridging occurring simultaneously in the periosteal and endosteal callus zone. (b) Further reduction in the production (1% of the reference value) of vascular growth factor by hypertrophic chondrocytes. No endochondral ossification occurs, constituting a non-union. (c) Removal of vascular growth factor in callus on day 0. It was verified an absence of healing response. Adapted from [173].

In order to overcome some limitations of the previously work, the models that included the regulation of cell diffusion and growth factors alone for angiogenesis were extended to include mechanical stimulation and then compared favourably with data obtained from fracture healing experimentally.

Shefelbine et al. [148] presented a fuzzy logic model based on local mechanical factors, as described by Claes et al. [145] and local vascularity, to simulate trabecular fracture healing. For the determination of tissue differentiation over time it was used a fuzzy logic controller composed of a set of twenty-one linguistic rules. This model allowed a linear elastic simulation of the main events of bone regeneration, determining that nutrient supply is essential in bone development, since bone formation only occurs with vascular supply.

Checa and Prendergast [162] used the stochastic cell model of Pérez and Prendergast [176], incorporating angiogenesis in the modulation of cell phenotype. This model allowed a simulation of cellular activity (migration, proliferation, differentiation, apoptosis, and angiogenesis) and capillary network formation included the mechanoregulation of vessel growth (Figure 5.10). The work predicted capillary networks similar to those observed experimentally when subjected to shear loading in a bone-implant interface model. Consequently, tissue differentiation patterns were more heterogeneous. Additionally, the model demonstrated that higher loads caused slower vascular development, resulting in delayed bone tissue formation.

The model was further applied to analyse the effect of cell seeding and mechanical loading on scaffolds, highlighting the possibilities of such modelling in the field of tissue engineering [179].

Subsequently, a study was also developed to understand the discrepancy in bone healing dynamics between large and small animals, where small animals showed faster healing when compared to larger animals [180]. A histological comparison was made with computer simulations (Figure 5.11), concluding that size differences between species do not explain the difference observed experimentally during secondary bone healing between these animals. Additionally, it was not possible to discern whether the discrepancies are due to differences in cell behaviour, material properties, or mechanosensitivity.

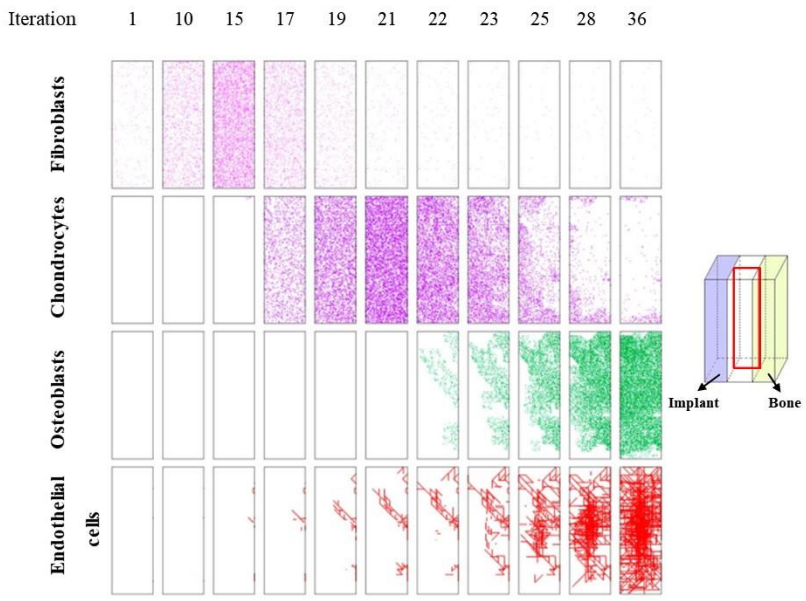

Figure 5.10 – Model by Checa and Prendergast (2009) showing the distribution of different cell phenotypes in a cross-section through the middle of the regenerating tissue under shear force condition. The presented distributions of endothelial cells include all endothelial cells within 100 μm (oxygen diffusion distance) from the selected section. Each dot represents a cell occupying a lattice point. Adapted from [162].

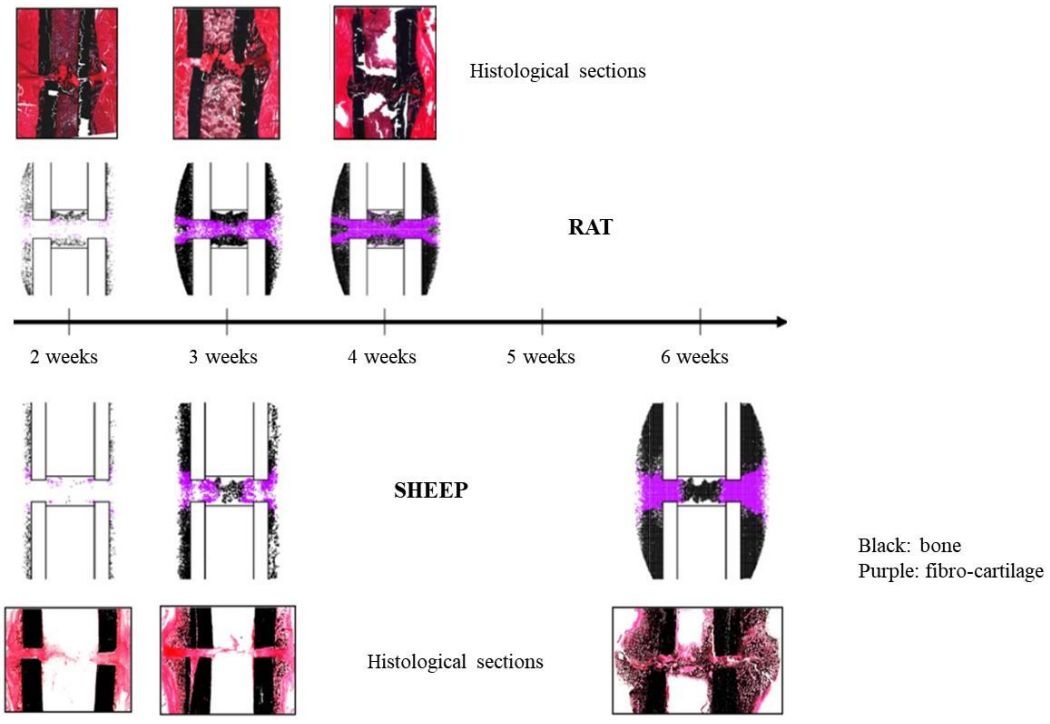

Figure 5.11 – Model by Checa and Prendergast (2011) with the predictions of bone healing and the histological sections in the rat (top) and sheep (bottom) models under axial compression load. The rat model shows initial endosteal and periosteal bone formation, which agrees with histology. However, no bone bridging was observed after four weeks. The sheep model showed no bridging after six weeks but early bone formation in the central gap region, which is not in accordance with the histology. Adapted from [180].

More recent work has modelled the effect of vasculature and indirect loading, i.e., instead of considering mechanical signals that will act directly on stem cells determining their differentiation pathway, it has been postulated that to regulate angiogenesis these act indirectly and, therefore, partially determine the local oxygen environment within a regenerating tissue [181]. Moreover, the model developed by Burke and Kelly extended the methods of Lacroix and Prendergast [157] to encompass the oxygen tension due to vascular diffusion that occurs in areas where the deviatoric strain is lower than 6% [181], [182]. This work predicted the main stages of repair, including cartilaginous bridging, endosteal and periosteal bony bridging and, bone remodelling. Local oxygen tension and surrounding tissue stiffness led to tissue differentiation, showing consistency with experimental results in fracture repair [182]. However, the modelling of angiogenesis was performed as a diffusive process, not considering the discrete nature of the vascular tree. Additionally, the model is limited to oxygen-dependent differentiation of MSCs, whereas experimental evidence reports that multiple cellular processes are regulated by oxygen.

Therefore, to make the representations of angiogenesis more realistic, the model developed in 2015 by Carlier et al. [183] introduced oxygen in simulations of bone healing, allowed to improve the effects of angiogenesis and to understand its influence. Thus, cell differentiation, endochondral ossification, cell proliferation, oxygen consumption, growth factor production, and cell death correspond to oxygen-dependent cellular activities. In this study, the spatiotemporal fractions of bone, cartilage and fibrous tissue in the oxygen model were predicted and are in agreement with experimental and *in silico* results (Figure 5.12). In addition, this model, when applied to a critical size defect, correctly predicted the establishment of a clinical non-union due to slow ingrowth of new blood vessels leading to hypoxic conditions and, subsequent, cell death in the central region of the fracture callus (Figure 5.13) [183].

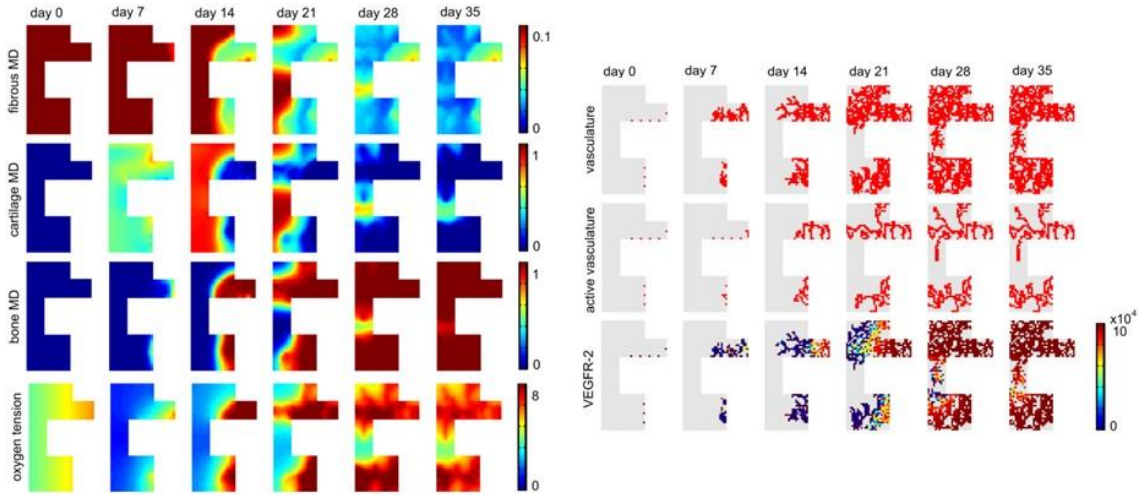

Figure 5.12 – Model by Carlier et al. with the spatio-temporal evolution of fibrous, cartilage and bone, oxygen tension, vasculature, active vasculature and VEGFR-2 levels on the endothelial cell during "normal" fracture healing in a small defect (0.5 mm). Adapted from [183].

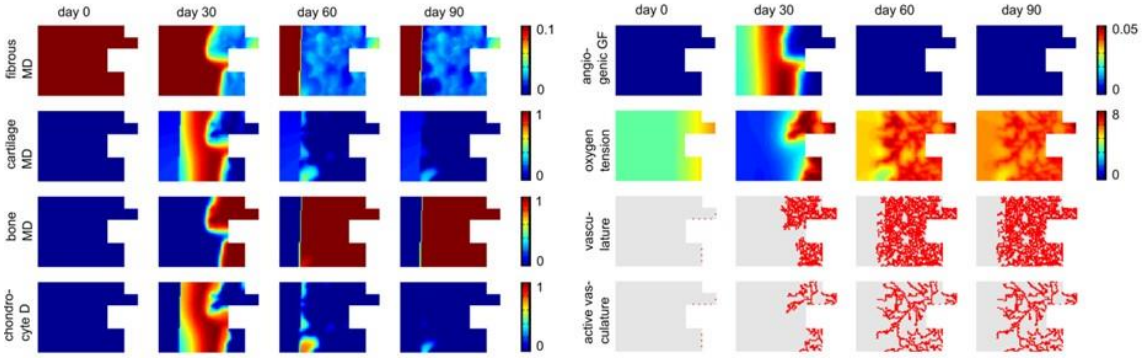

Figure 5.13 – Model by Carlier et al. with the spatio-temporal evolution of fibrous tissue matrix density, cartilage and bone, chondrocyte density, angiogenic growth factor concentration, oxygen tension, vasculature, active vasculature during impaired fracture healing in a large defect (3 mm). Adapted from [183].

CHAPTER 6 – NUMERICAL WORK

6. Numerical Work

The morphology of bone healing is characterized by the tissue types and regenerative processes involved. In this process, there is a sequential differentiation from one tissue type to another, and these are sensitive to the local mechanical environment. In this context, it becomes essential to understand the correlation of the mechanical conditions during this process and how these can influence the final outcome. Computational advances allow directing the focus towards the determination of the mechanical and biological parameters that influence the processes of bone regeneration and remodelling through mathematical modelling.

In the present chapter, a study is conducted using numerical methods on a three-dimensional tibial fracture model to estimate the mechanical conditions of a healing callus. Therefore, the numerical model is presented with the respective description and geometry based on an experimental work. It is represented by a progressive temporal variation of the callus shape and mechanical properties during bone healing. Subsequently, the linear elasto-static analyses are presented in which distinct numerical methods are used in order to evaluate and compare the results obtained by each one of them. Furthermore, a remodelling algorithm was applied to a two-and three-dimensional model in the final stage of bone healing in order to reproduce the respective bone distributions and compare them with an *in vivo* study.

6.1. Time-Dependent Mechanical Study of Bone Fracture Healing

6.1.1. Model Geometry and Description

Initially, a three-dimensional finite-element (FE) model was designed, whose geometry and mesh creation were carried out using the Finite Element Modelling And Post-processing software (FEMAP©), student edition (version 2020.2), developed by Siemens. It is an advanced software that provides CAD import, modelling and meshing tools to create a FE model. Additionally, it contains post-processing functionality, allowing the interpretation of analysis results.

The geometry and dimensions given to the model (Figure 6.1(a) and 6.1(b)) were based on previous studies [5], [157], [165], [184]. During the healing process, a large

callus is formed outside the bone featuring a periosteal formation, as well as a smaller callus that forms a bridge inside the medullary cavity within the bone, corresponding to an endosteal formation [185]. Therefore, it was established that the periosteal callus has a thickness of 4 mm and the transverse fracture gap corresponds to 2 mm. The 2 mm fracture gap was defined from the literature since a size between 2 mm or less is filled by more than 50% with bone and cartilage and, therefore, achieve much greater stability, in contrast to larger gaps that present only 20% [7], [186]. It should be noted that the mesh was refined in the bone callus area, and after the model discretization, it was obtained a model composed of a mesh with 3071 nodes and 11859 tetrahedral elements (Figure 6.1(c)).

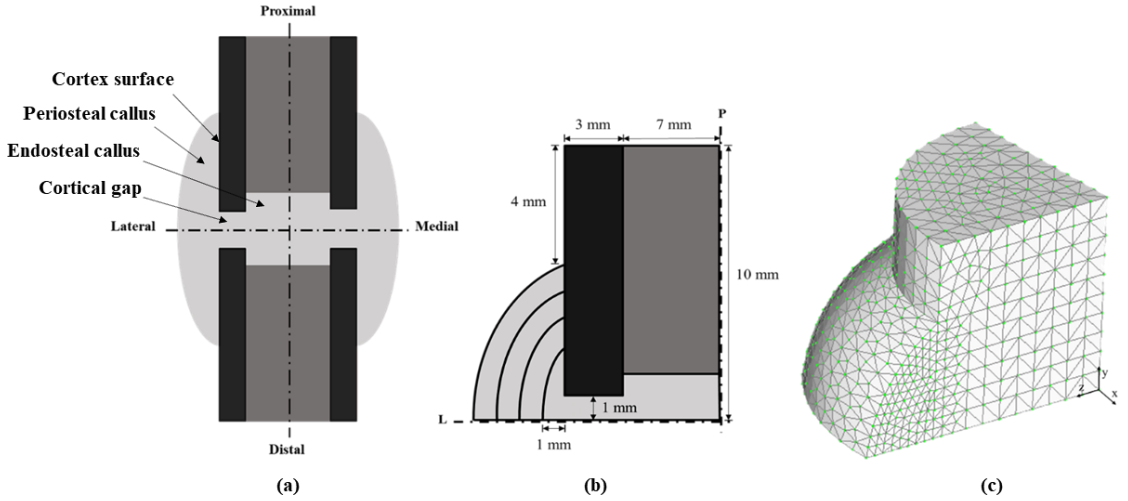

Figure 6.1- Representation of the tibial model with callus in bone healing. (a) Two-dimensional model geometry of a fractured tibia with callus and identification of the different callus regions, (b) two-dimensional quarter model, (c) three-dimensional quarter model composed of a mesh with 3071 nodes and 11859 tetrahedral elements.

The corresponding mesh was imported to the Finite Element and Meshless Methods Analysis Software (FEMAS) (cmech.webs.com), an academic freeware implemented in MATLAB© (Mathworks, version 9.6) with a graphical user interface (GUI), as can be depicted in Figure 6.2. FEMAS is a structural analysis software that permits to conduct linear and non-linear analysis using the FEM or meshless methods. It also allows the analysis of 2D and 3D problems and provides greater control in the design of numerical models as well as the location of essential and natural boundary conditions. It offers the possibility to import geometries from other CAD software. The

computational framework employs the plane stress and plane strain two-dimensional deformation theory and the three-dimensional deformation theory in the analysis. In the analyses performed, the workflow is divided into three phases: pre-process, process and post-process.

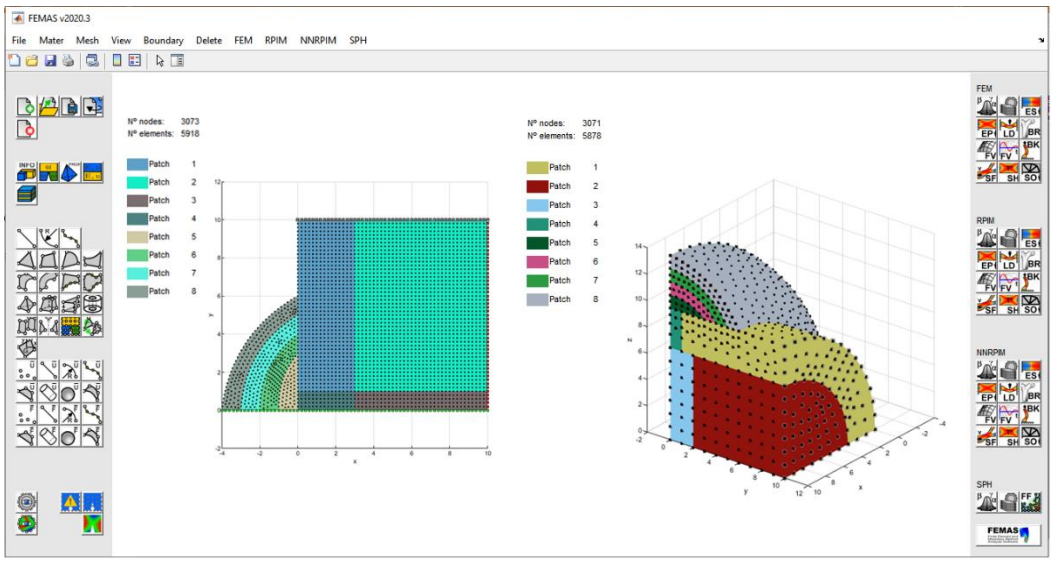

Figure 6.2- FEMAS graphical user interface.

The progression of healing is described by a complex pattern of the temporal evolution of distinct tissue types in the fracture callus. Therefore, the constructed model was adapted based on histological images of the fracture sites obtained in an experimental study performed on 64 sheep with a 3 mm tibial mid-shaft osteotomy stabilized with an external fixator [5], [187]. Through this experimental work, bone fracture samples consisting of callus and adjacent bone were obtained with the respective bone healing at time points after two, three, six and nine weeks. At two weeks, it is possible to observe, on the periosteal surface of the cortical bone, the beginning of woven bone formation by intramembranous ossification. However, it is absent both in the intercortical zone and endosteum. The remaining soft callus is filled with fibrous tissue (Figure 6.3(a)). After three weeks, the periosteal callus visibly increases in size with continuous formation of woven bone. Certain regions of the advancing ossification fronts are constituted by cartilage. In addition, some of the bone components begin to approach and fill the fracture gap. The remaining space in the fracture site is filled by fibrous tissue (Figure 6.3(b)). At six weeks, a complete bridging of the periosteal callus is visible. Additionally, at the outer

border of the periosteal callus, a significant increase in the presence of osteoclasts can be observed. There is also a progression in the endosteal bony bridging (Figure 6.3(c)). Finally, at nine weeks, significant remodelling changes in the cortical bone due to osteoclastic activity were observed. Moreover, the outermost regions of the periosteal callus were resorbed, exhibiting a decreased size. The intercortical bony bridging was also complete and, resorption of the endosteal callus was ongoing (Figure 6.3(d)).

Figure 6.3- Light microscopical images of the histological sections stained with Safranin-Orange/von Kossa in four different time points of fracture healing, (a) two weeks, (b) three weeks, (c) six weeks and (d) nine weeks (red: soft tissue, black: mineralized tissue). Adapted from [5], [187].

Additionally, with these longitudinal histological sections and an image analysis (through an averaging procedure) performed, six successive tissue type patterns were identified in the callus corresponding to healing phases along with the progression of "normal" bone healing [188]. This analysis distinguished between several tissue types in the callus, such as fibrous tissue, cartilage, cortical bone and newly formed bone (woven bone). Therefore, following the literature [189] and the topological criteria established by Vetter et al. [188] with the corresponding six healing stages (Table 6.1), the model was developed to represent the respective characteristics from the first to the ninth week of healing.

Table 6.1- Topological criteria and the respective consolidation phase [188].

Healing Stage	Topological Criteria	Classification According to Healing Phases
Stage I	Remnants of hematoma still present in the callus	Late inflammatory phase
Stage II	No remnants of hematoma left; cartilage not yet formed	Early reparative phase
Stage III	Bridging via cartilage in the outer osteotomy zone, but no bony bridging of the osteotomy gap	Reparative phase
Stage IV	Formation of a periosteal bony bridge between the proximal and distal parts of the callus	Late reparative phase
Stage V	Formation of an endosteal bony bridge between medial and lateral parts of the callus	Early remodelling phase
Stage VI	Reduced size of the hard callus, resorption of the endosteal bony	Remodelling phase

Consequently, each week's model was associated to a healing stage. Accordingly, the first and second weeks correspond to the first stage, the third week to the second stage, the fourth and fifth weeks to the third stage, the sixth week to the fourth stage, the seventh and eighth weeks to the fifth stage and, finally, the ninth week to the sixth stage.

6.1.2. Material Properties and Boundary Conditions

The bone healing process involves the development of a fracture callus that modifies both the mechanical properties and the geometry of the fracture site in order to provide optimal biological conditions for healing. Throughout this process, a successive stiffening of the callus occurs, which mechanically stabilises the bone fracture fragments. This progressive change occurs at three distinct hierarchical levels in the callus structure. Regarding the macroscopic level, there is an increase in bending stiffness due to the deposition of new material distant to the long bone axis caused by callus growth. On the mesoscopic level, besides the formation of new material within the callus, such as fibrous tissue, cartilage, and bone, the trabecular network becomes denser. Additionally, at the microscopic level, the material properties of the tissues change over time through, for example, the integration of higher mineral content in the newly formed bone. Consequently, it becomes relevant to consider the heterogeneity of the material properties

and the distribution of tissues in the callus, as these influence the stresses and strains in the fracture area.

Therefore, assuming mechanical isotropy, the Young's modulus of the hard callus at the mesoscopic scale is given by two portions of two distinct levels of the hierarchical structure. The first corresponds to the bone area fraction, given by the ratio of bone area (BA) over tissue area (TA), at the architectural level and, the second consists of the Young's modulus of the hard callus material, E_{mat} , at the material level. Thus, the (bulk) Young's modulus (E) of the hard callus is given by the equation of Gibson-Ashby [78],

$$E = E_{mat}\left(\frac{BA}{TA}\right)^{\kappa} \qquad \text{Eq. (6.1)}$$

where E_{mat} denotes the Young's modulus of the bone material and BA/TA represents the bone area fraction. A value of 1.83 was used for the exponent κ [190].

Additionally, the hard callus densification or the increase in bone area fraction, was obtained by image analysis performed on the histological sections presented previously (Figure 6.4(a)).

On the other hand, the Young's modulus of the bone material was obtained from an experimental nanoindentation study (about 1,000 indents per sample), along the course of bone healing (Figure 6.4(b)) [191]. A Scanning Nanoindenter with a Berkovich diamond indenter tip was used for the measurements, using the method of Oliver and Pharr in order to obtain the indentation modulus (E_r). Thus, to calculate the Young's modulus (E_{mat}) the following equation was used,

$$\frac{1}{E_r} = \frac{1-\nu^2}{E} + \frac{1-{\nu_i}^2}{E_i} \qquad \text{Eq. (6.2)}$$

where E_i is the Young's modulus of the Berkovich diamond indenter, which corresponds to 1140 GPa. ν_i denotes the Poisson's ratio of the Berkovich diamond indenter, given by 0.07. E and ν correspond to the Young's modulus and Poisson's ratio of the bone, respectively.

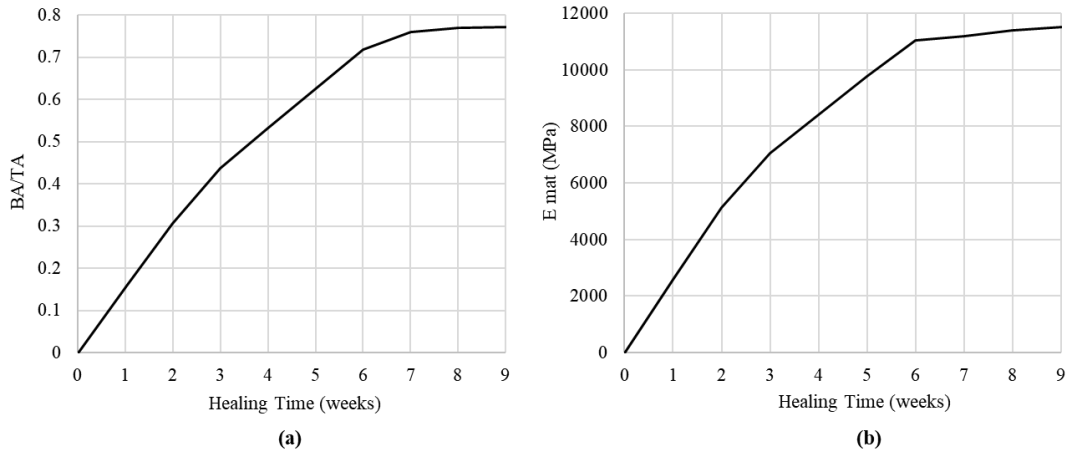

Figure 6.4- Graphical representations of the experimental data of newly formed hard callus in sheep. (a) Time evolution of the bone fraction area (BA/TA). (b) Time evolution of the Young's modulus of bone material obtained experimentally by nanoindentation. Adapted from [188] [191].

Hence, using the Gibson-Ashby equation (Eq. (6.1)), the Young's modulus of the hard callus over the nine weeks of consolidation was obtained, as depicted in Figure 6.5.

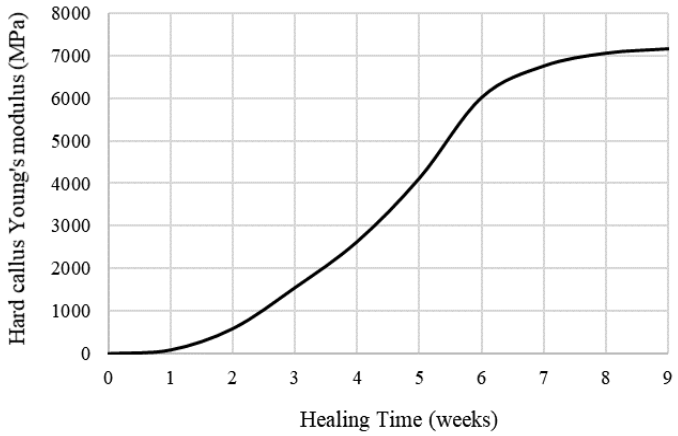

Figure 6.5- Graphical representation of the time course of Young's modulus of hard callus during bone fracture healing.

Subsequently, the mechanical properties of the tissues are presented in Table 6.2. Both Young's modulus (E) and Poisson's ratio (ν) were obtained from the literature.

Table 6.2- Mechanical properties of the different tissue types present in the model.

Type of Material	Young's modulus (MPa)	Poisson's ratio	Reference
Fibrous Tissue	2	0.4999	[80]
Cartilage	10	0.4999	[165]
Woven Bone (hard callus)	Time dependent	0.4999	[191]
Trabecular Bone	1100	0.3	[165]
Cortical Bone	20000	0.3	[77]

Furthermore, the model is composed of eight materials (Figure 6.6) and the Young's modulus defined for each material during the weeks of bone healing are represented in Table 6.3.

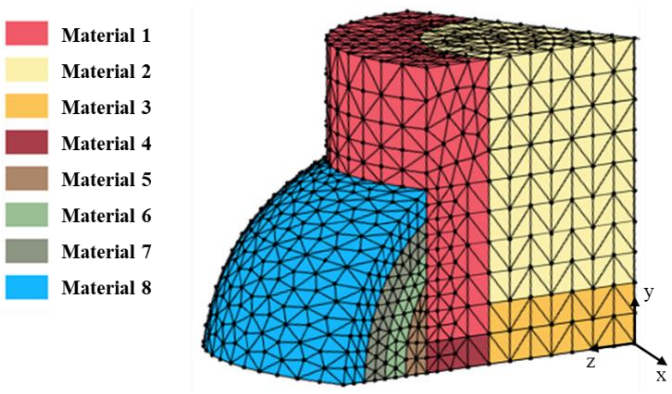

Figure 6.6- Representation of the materials that constitute the model.

Material 1 and 2 correspond to cortical and trabecular bone, respectively. On the other hand, material 3 until the fifth week consists of fibrous tissue and the remaining weeks of woven bone. Similarly, material 4 up to the third week presents fibrous tissue and cartilage in the fourth week and woven bone in the remaining weeks. Finally, materials 5 to 8 correspond to woven bone. Note that the appearance of woven bone and the consequent change in mechanical properties vary over time during the bone healing process.

Table 6.3- Young's modulus of each material over the bone healing time.

		Healing Time (weeks)								
		Week 1	Week 2	Week 3	Week 4	Week 5	Week 6	Week 7	Week 8	Week 9
Young's modulus of each material (MPa)	M1	20000	20000	20000	20000	20000	20000	20000	20000	20000
	M2	1100	1100	1100	1100	1100	1100	1100	1100	1100
	M3	2	2	2	2	2	87	589	589	589
	M4	2	2	2	10	87	589	1555	2640	4134
	M5	87	589	1555	2640	4134	6033	6770	7070	7172
	M6	-	-	87	589	1555	2640	4134	6033	6770
	M7	-	-	-	87	589	1555	2640	4134	-
	M8	-	-	-	-	-	87	-	-	-

Regarding the boundary conditions, the nodes displacement was constrained in the *Ozy* plane in the *x* direction, in the *Oxz* plane in the *y* direction and in the *Oxy* plane in the *z* direction. Additionally, a vertical displacement of 0.01 mm was applied at the top of the model.

6.1.3. Elasto-Static Analysis

With the experimental data providing quantitative information regarding the development of the callus geometry, the tissue arrangements with the callus, and the mechanical properties of the bone material over time, a more detailed mechanical study of the bone healing process can be conducted. Thus, with the developed callus model and using the input data referred to in the previous section for the FEM and RPIM computations, the stresses and strains within the model at the six bone healing stages are obtained.

6.1.3.1. Initial Conditions

The 3D model was analysed considering the classic deformation theory. Using two distinct numerical methods, FEM and RPIM, it is possible to determine the stress and

strain fields in the callus region. Therefore, the bone callus was mechanically modelled in terms of linear elasticity and the materials were considered to be isotropic.

As mentioned in chapter 4, the calculation accuracy of the meshless method is affected by several factors, mainly the nodal distribution and influence-domains. In FEM, the nodal connectivity is ensured by the predefined finite element mesh, whereby nodes belonging to the same element interact directly with each other and with the boundary nodes of neighbouring finite elements. In contrast, in meshless methods, nodal connectivity is achieved by overlapping the influence-domain of each node. Thus, throughout the model domain, the variation of the size of the influence-domain will directly affect the solution of the meshless method and, consequently, the quality of the results [10]. Hence, different sizes of influence-domains were considered in the RPIM analyses, being composed of 32, 16, 9 and 4 nodes. Regarding the RPI shape functions, the shape parameters of $c = 0.0001$, $p = 0.9999$ and a constant polynomial basis were assumed. Additionally, a Gauss quadrature of 0 was also used.

6.1.3.2. Results and Discussion

6.1.3.2.1. Stress and Strain Fields

In this section, the results obtained from the numerical simulations in the different healing stages are presented. The FEM and the RPIM were used to analyse the model through the FEMAS© software implemented in MATLAB© in order to evaluate and compare the results of each of the methods applied.

Therefore, it was possible to obtain several important parameters to study the model's behaviour and how these change with callus maturation during the bone healing process, such as the von Mises effective stress, principal stresses, equivalent effective strain and, lastly, principal strains.

The qualitative analysis of the colour maps enables to discriminate the differences in the distribution of the values, for both the stress and strain fields, along the weeks of bone healing. The results obtained are depicted in Figures 6.7 to 6.15 concerning the numerical method used and the corresponding week of healing.

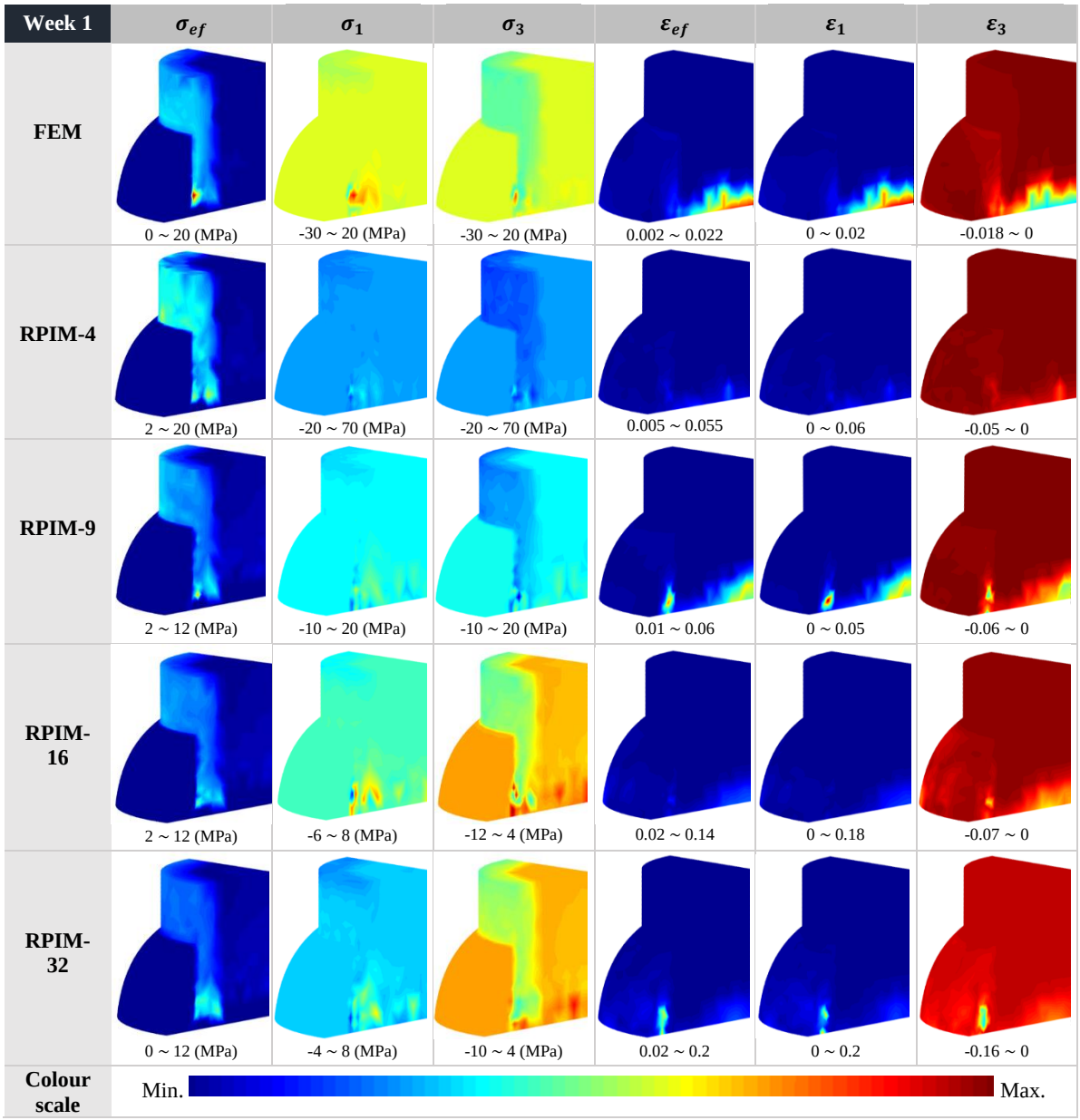

Figure 6.7- FEM, RPIM-4, RPIM-9, RPIM-16 and RPIM-32 solutions for week 1 of the first bone healing stage with the respective stress and strain maps: von Mises effective stress (σ_{ef}) and principal stresses (σ_1 and σ_3), equivalent effective strain (ε_{ef}) and principal strains (ε_1 and ε_3).

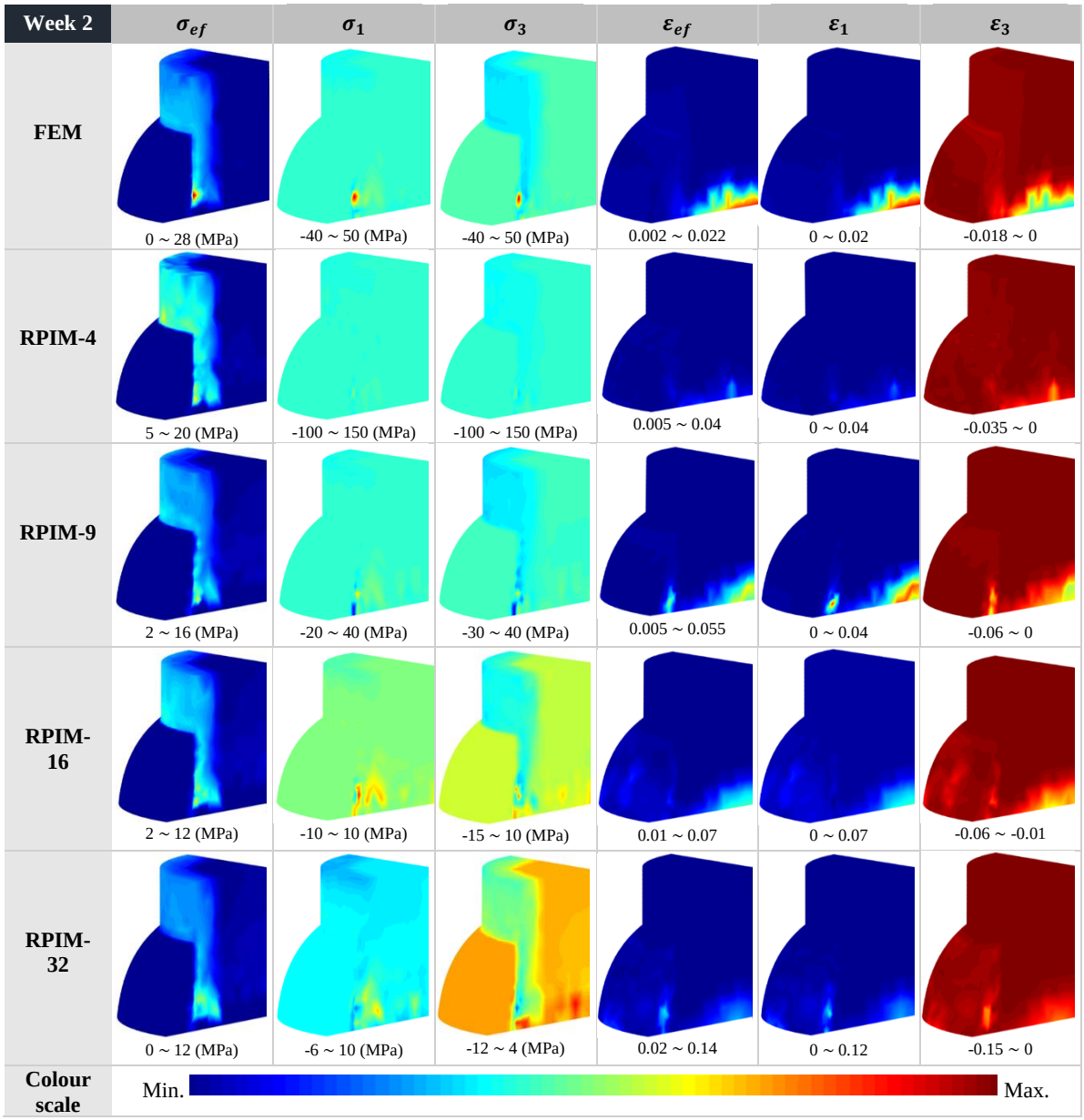

Figure 6.8- FEM, RPIM-4, RPIM-9, RPIM-16 and RPIM-32 solutions for week 2 of the first bone healing stage with the respective stress and strain maps: von Mises effective stress (σ_{ef}) and principal stresses (σ_1 and σ_3), equivalent effective strain (ε_{ef}) and principal strains (ε_1 and ε_3).

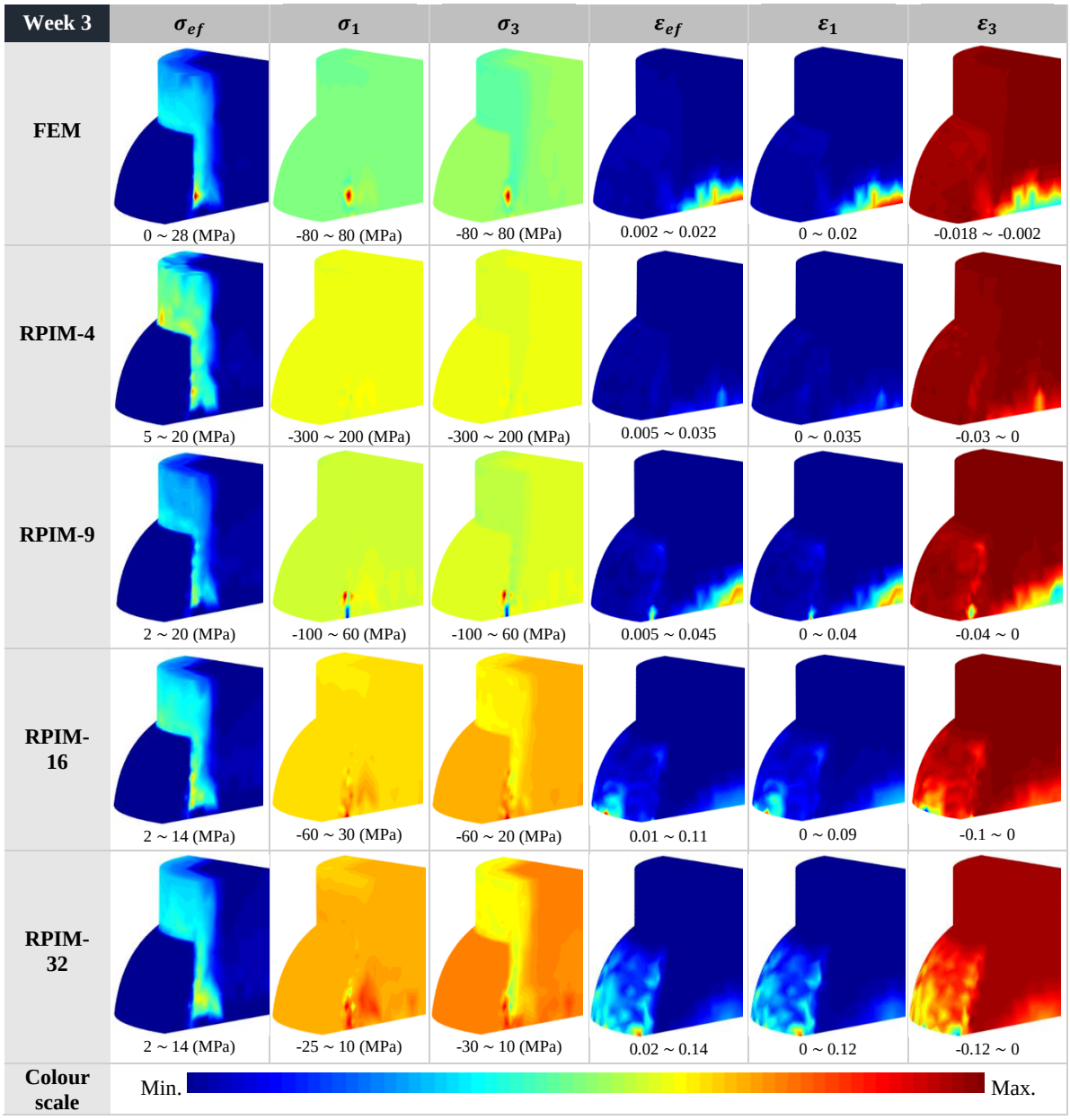

Figure 6.9- FEM, RPIM-4, RPIM-9, RPIM-16 and RPIM-32 solutions for week 3 of the second bone healing stage with the respective stress and strain maps: von Mises effective stress (σ_{ef}) and principal stresses (σ_1 and σ_3), equivalent effective strain (ε_{ef}) and principal strains (ε_1 and ε_3).

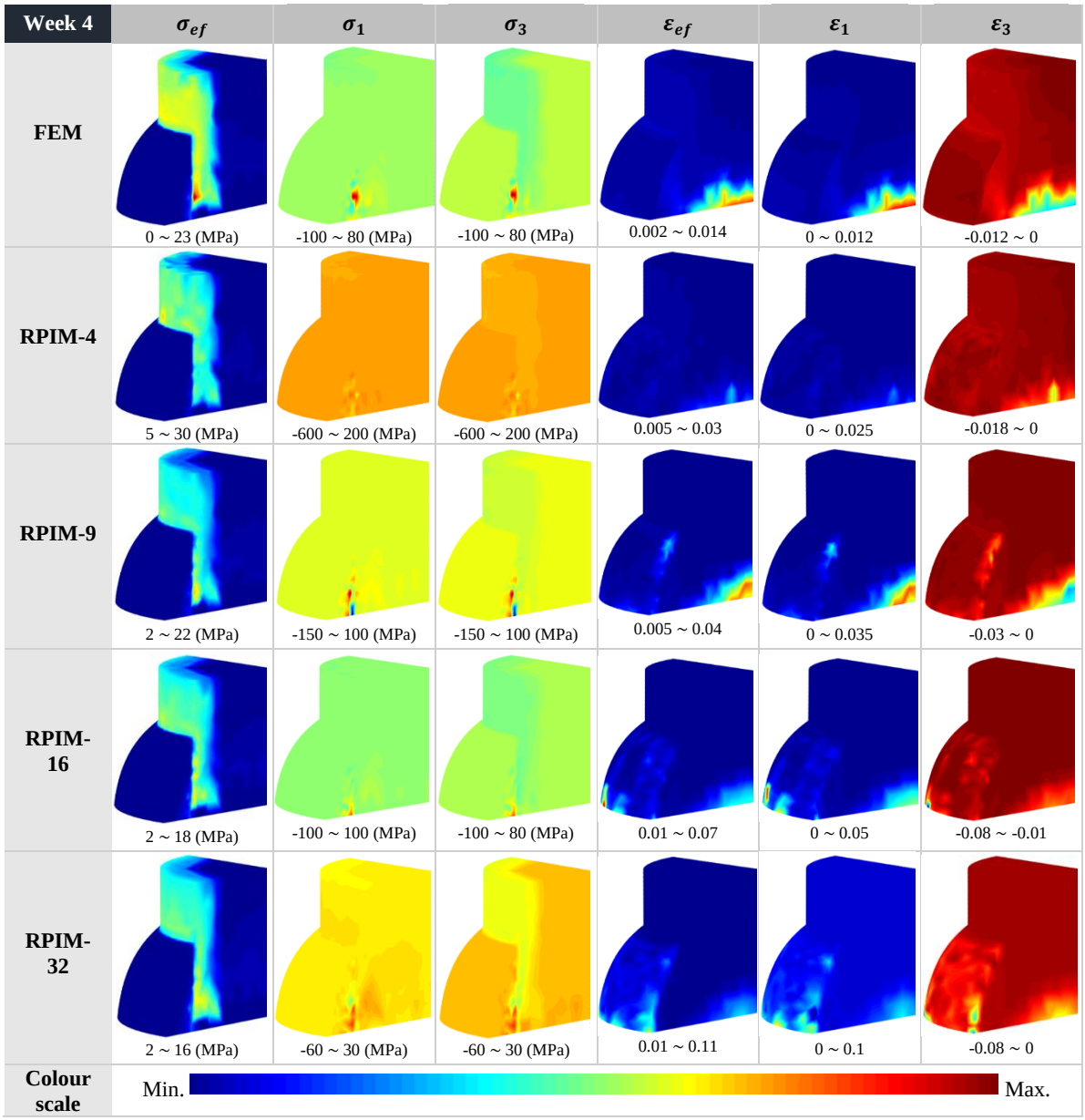

Figure 6.10- FEM, RPIM-4, RPIM-9, RPIM-16 and RPIM-32 solutions for week 4 of the third bone healing stage with the respective stress and strain maps: von Mises effective stress (σ_{ef}) and principal stresses (σ_1 and σ_3), equivalent effective strain (ε_{ef}) and principal strains (ε_1 and ε_3).

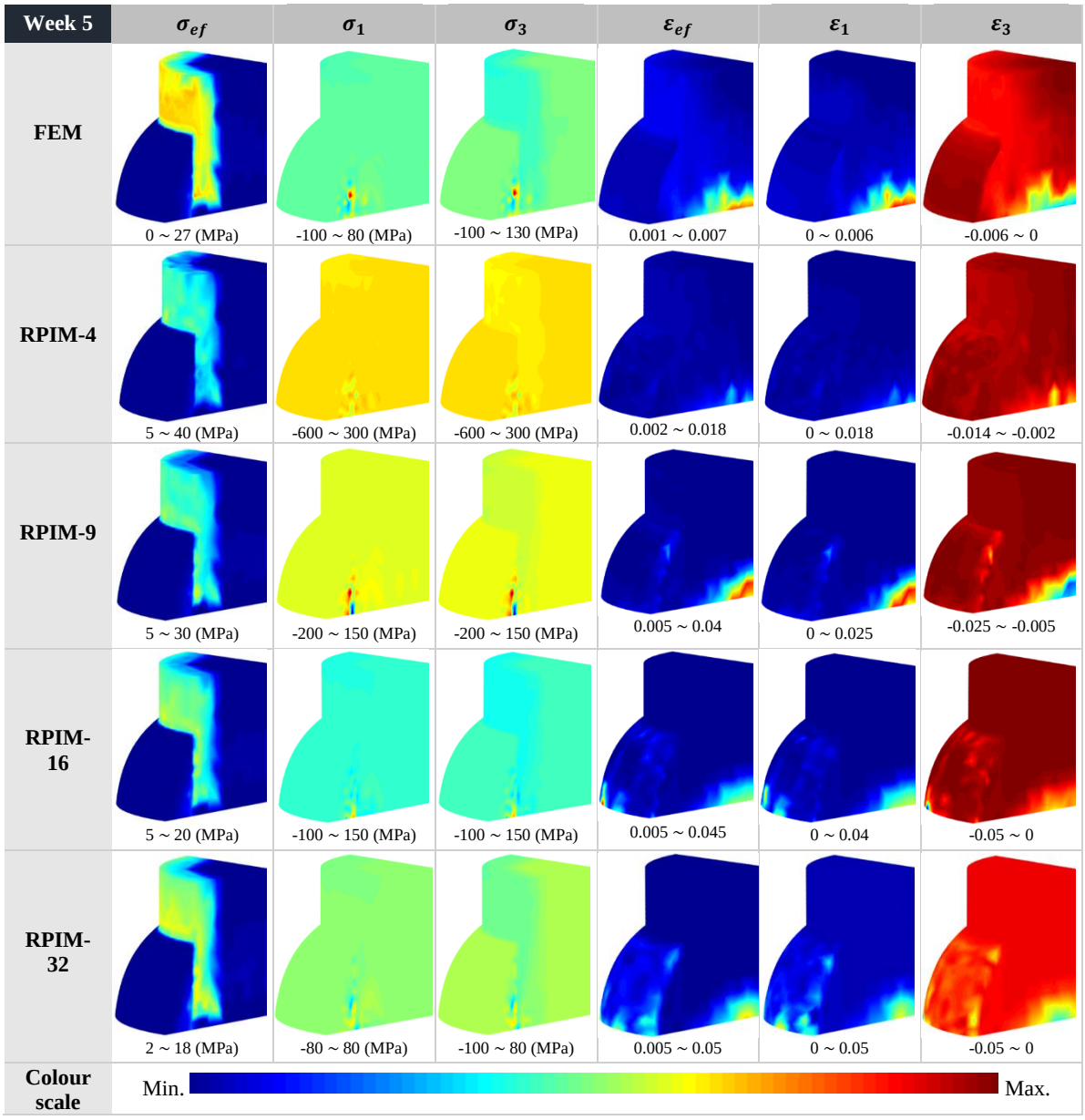

Figure 6.11- FEM, RPIM-4, RPIM-9, RPIM-16 and RPIM-32 solutions for week 5 of the third bone healing stage with the respective stress and strain maps: von Mises effective stress (σ_{ef}) and principal stresses (σ_1 and σ_3), equivalent effective strain (ε_{ef}) and principal strains (ε_1 and ε_3).

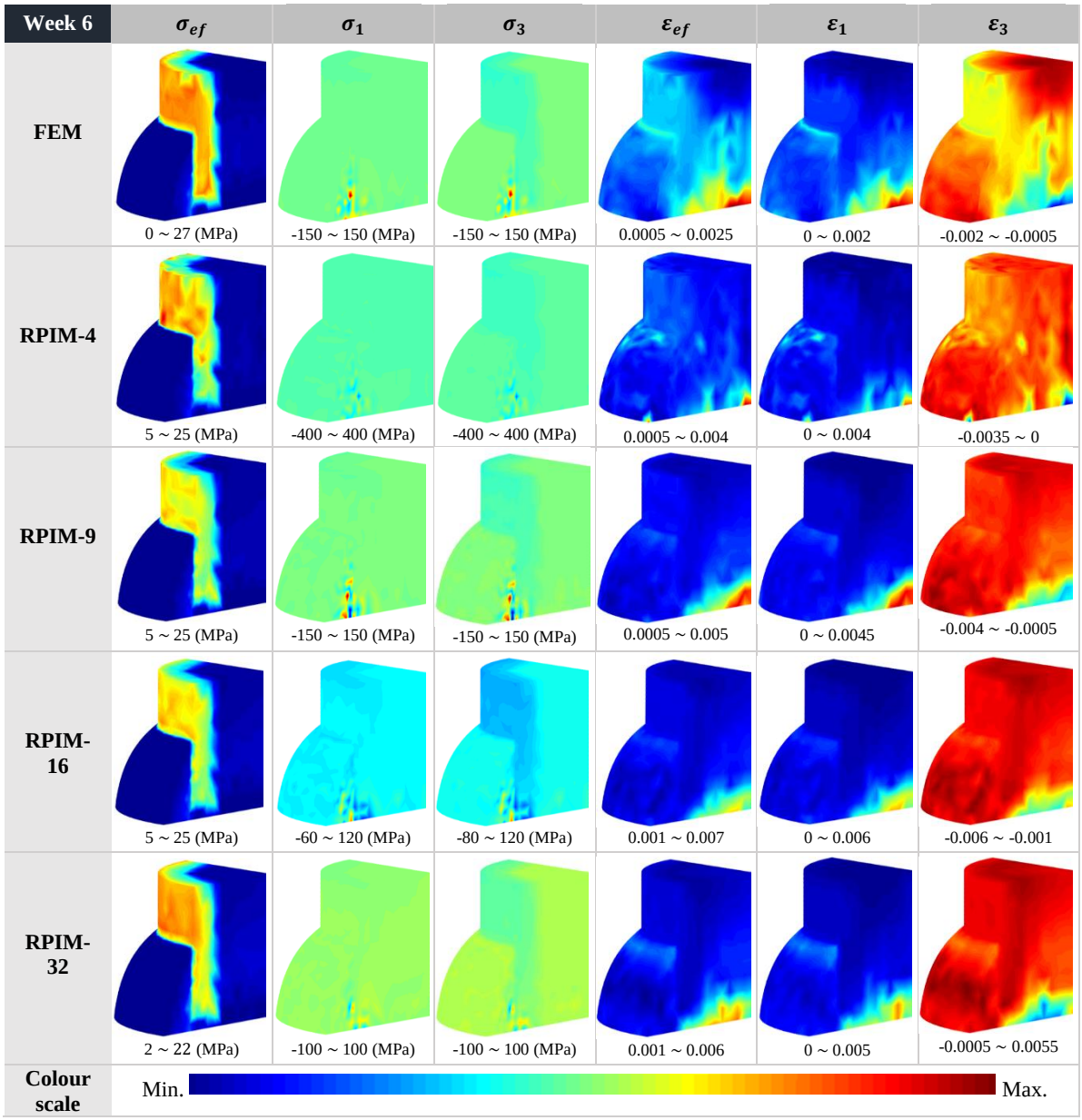

Figure 6.12- FEM, RPIM-4, RPIM-9, RPIM-16 and RPIM-32 solutions for week 6 of the fourth bone healing stage with the respective stress and strain maps: von Mises effective stress (σ_{ef}) and principal stresses (σ_1 and σ_3), equivalent effective strain (ε_{ef}) and principal strains (ε_1 and ε_3).

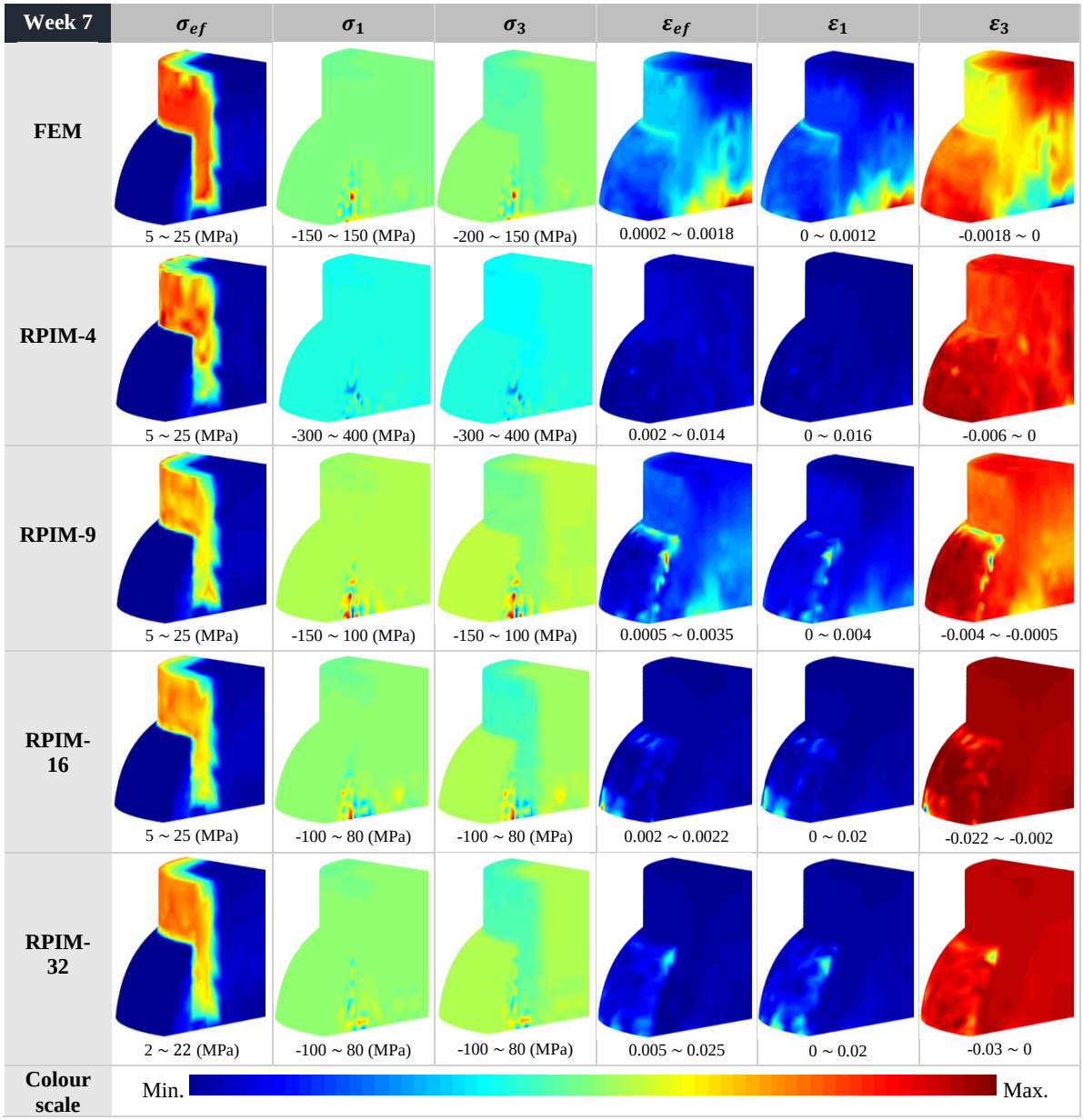

Figure 6.13- FEM, RPIM-4, RPIM-9, RPIM-16 and RPIM-32 solutions for week 7 of the fifth bone healing stage with the respective stress and strain maps: von Mises effective stress (σ_{ef}) and principal stresses (σ_1 and σ_3), equivalent effective strain (ε_{ef}) and principal strains (ε_1 and ε_3).

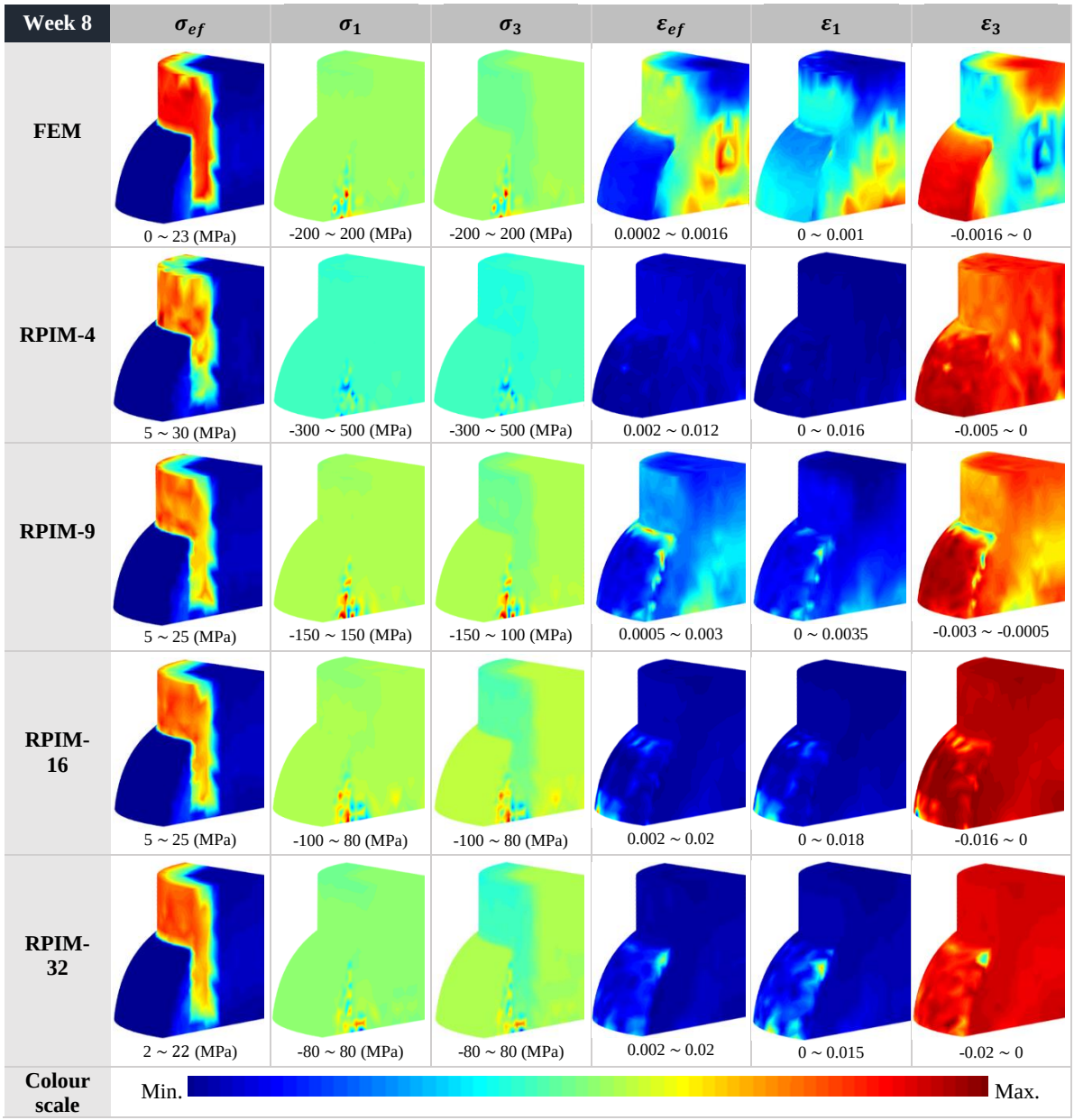

Figure 6.14- FEM, RPIM-4, RPIM-9, RPIM-16 and RPIM-32 solutions for week 8 of the fifth bone healing stage with the respective stress and strain maps: von Mises effective stress (σ_{ef}) and principal stresses (σ_1 and σ_3), equivalent effective strain (ε_{ef}) and principal strains (ε_1 and ε_3).

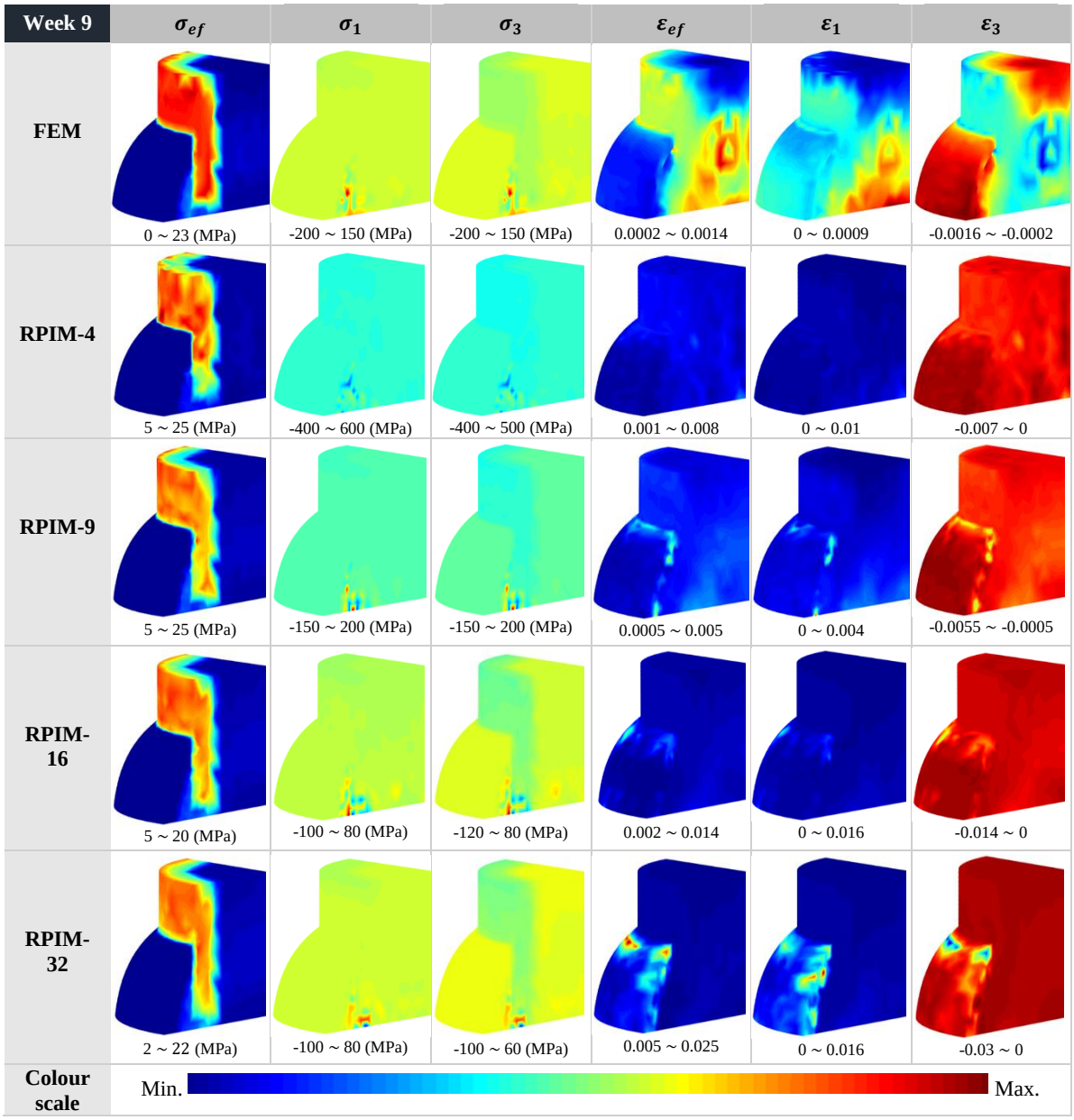

Figure 6.15- FEM, RPIM-4, RPIM-9, RPIM-16 and RPIM-32 solutions for week 9 of the sixth bone healing stage with the respective stress and strain maps: von Mises effective stress (σ_{ef}) and principal stresses (σ_1 and σ_3), equivalent effective strain (ε_{ef}) and principal strains (ε_1 and ε_3).

Due to the fact that the model presents distinct types of materials to represent the regeneration phases over time, the sizes defined for the influence-domains in RPIM can directly affect the results. Some differences are visible in the qualitative maps presented for the domains 32, 16, 9 and 4, where the last one is closer to the FEM formulation. Larger influence-domains aggregate more distant nodes that may belong to another

adjacent material, smoothing its inherent mechanical properties, in contrast to smaller influence-domains.

Overall, in the colour dispersion maps, when comparing the FEM and RPIM analyses, both show that cortical bone is subject to greater von Mises effective stress (σ_{ef}) than trabecular bone and bone callus due to the high Young's modulus relative to the other tissues. Since cortical bone forms the dense outer shell (cortex) of long bones, has greater volume and mass, it corresponds to the main load-bearing structure in bone, which allows it to sustain large loads. Complementarily, the presence of the inner core of trabecular bone directs the stresses towards the cortical bone [192].

Regarding the principal stresses (σ_1 and σ_3), these allow the analysis of the types of stresses, tensile or compression, present in the different regions of the model over the weeks of healing. The highest positive values of σ_1 represent the highest tensile stresses, and the highest negative values (absolute values) of σ_3 correspond to the highest compressive stresses. Therefore, the highest tensile stresses are mostly found in the periosteal callus near the fracture gap and along the cortex, from the first to the last week of regeneration. On the other hand, it can be observed that the cortical bone is subjected to higher compressive stresses than the trabecular bone and the bone callus over the weeks. In fact, cortical bone has higher compressive strength, approximately 100-200 MPa, than trabecular bone, approximately 0-20 MPa [193]. Additionally, there is a marked influence of compressive stresses on the entire periosteal and endosteal callus from the first to the last week of regeneration. It is reported that intramembranous ossification is driven by tensile stresses, whereas endochondral ossification is driven by compressive stresses [194]. Furthermore, the mineralised constituent of bone is highly resistant to compressive stress, contrary to tensile stress.

Concerning the equivalent effective strain (ε_{ef}), through direct observation of the colour maps, it is possible to notice that in the first weeks of regeneration, strains are higher at the fracture site, and with the consequent maturation of both periosteal and endosteal callus, these are gradually distributed in the adjacent tissues.

Similarly, considering the principal strains (ε_1 and ε_3), tensile and compressive strains, respectively, tensile strains are higher in the endosteal callus near the medullary cavity at nine weeks of regeneration, decreasing its preponderance as the bone callus matures. The regions at the fractured extremity and along the fracture gap are subject to

higher compressive strains than the other regions up to seven weeks. These decrease progressively as the stability of the bone callus increases through the formation of the periosteal and endosteal bony bridge. In an experimental study, it was found that in the early weeks, the callus experiences compressive strains over a wider area extending outwards from the fracture gap and into the periosteal callus. In addition, the tensile strains were not concentrated at the cortex edges [195]. On the other hand, in the last two weeks, which characterise the remodelling stage, compressive strains are distributed both across the cortical and trabecular bone and the endosteal and periosteal callus. The compressive strains experienced by immature tissues can initiate both anabolic (tissue formation) and catabolic (tissue resorption) processes [196].

There are particular differences between the applied numerical methods, namely RPIM with the different influence-domains and FEM, given the intrinsic formulations of each method. However, RPIM-9 reproduced stress and strain distributions close to the FEM and the information found in the literature [144], particularly in the periosteal callus.

Furthermore, in order to perform a more reliable and detailed analysis, nodes belonging to two regions of the model were chosen to study the variations of local von Mises effective stresses and equivalent effective strains, denoted by red lines in Figure 6.16. These regions allow the representation of the ossification paths.

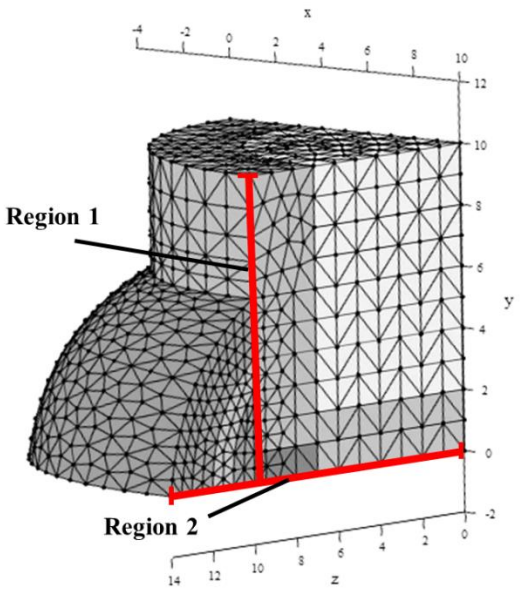

Figure 6.16- Regions selected to analyse the von Mises effective stress and equivalent effective strain.

Therefore, it was possible to perform graphical representations of the distribution of the von Mises effective stress and equivalent effective strain obtained with FEM, RPIM-4, RPIM-9, RPIM-16, RPIM-32 in each week of bone regeneration along the two selected regions, as shown in Figures 6.17 to 6.20.

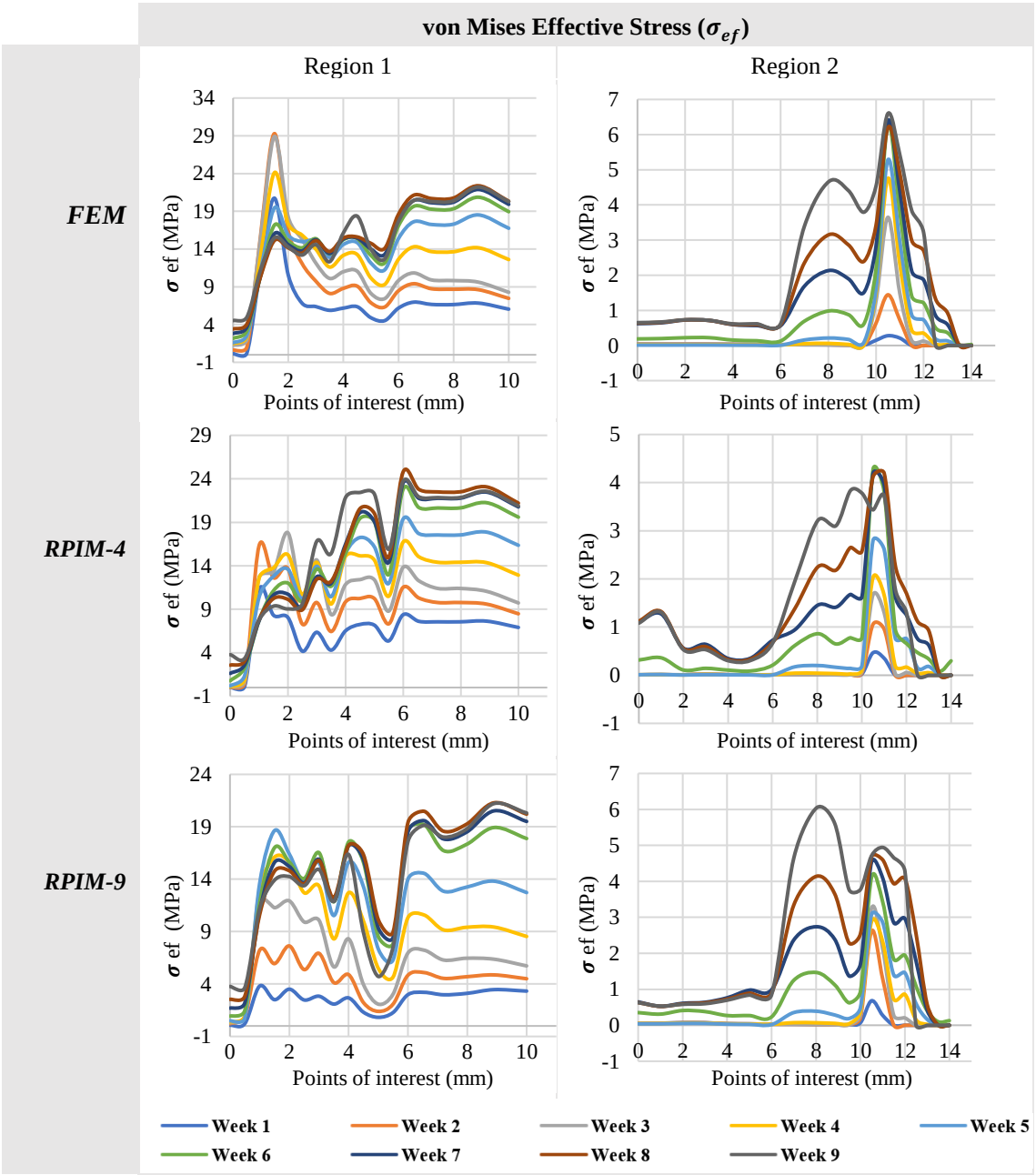

Figure 6.17- Graphical representations of the distribution of the von Mises effective stress in each week of bone regeneration along the regions 1 and 2 in FEM, RPIM-4 and RPIM-9.

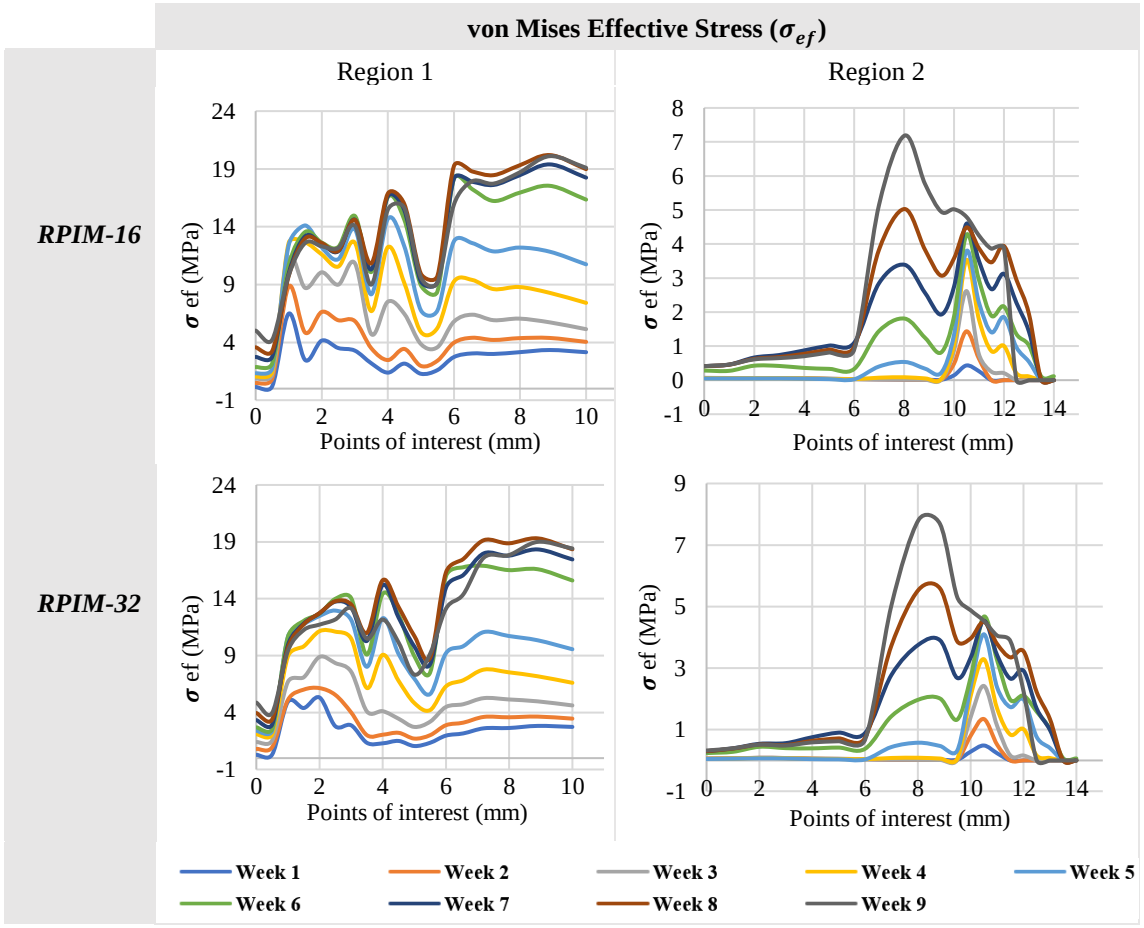

Figure 6.18- Graphical representations of the distribution of the von Mises effective stress in each week of bone regeneration along the regions 1 and 2 in RPIM-16 and RPIM-32.

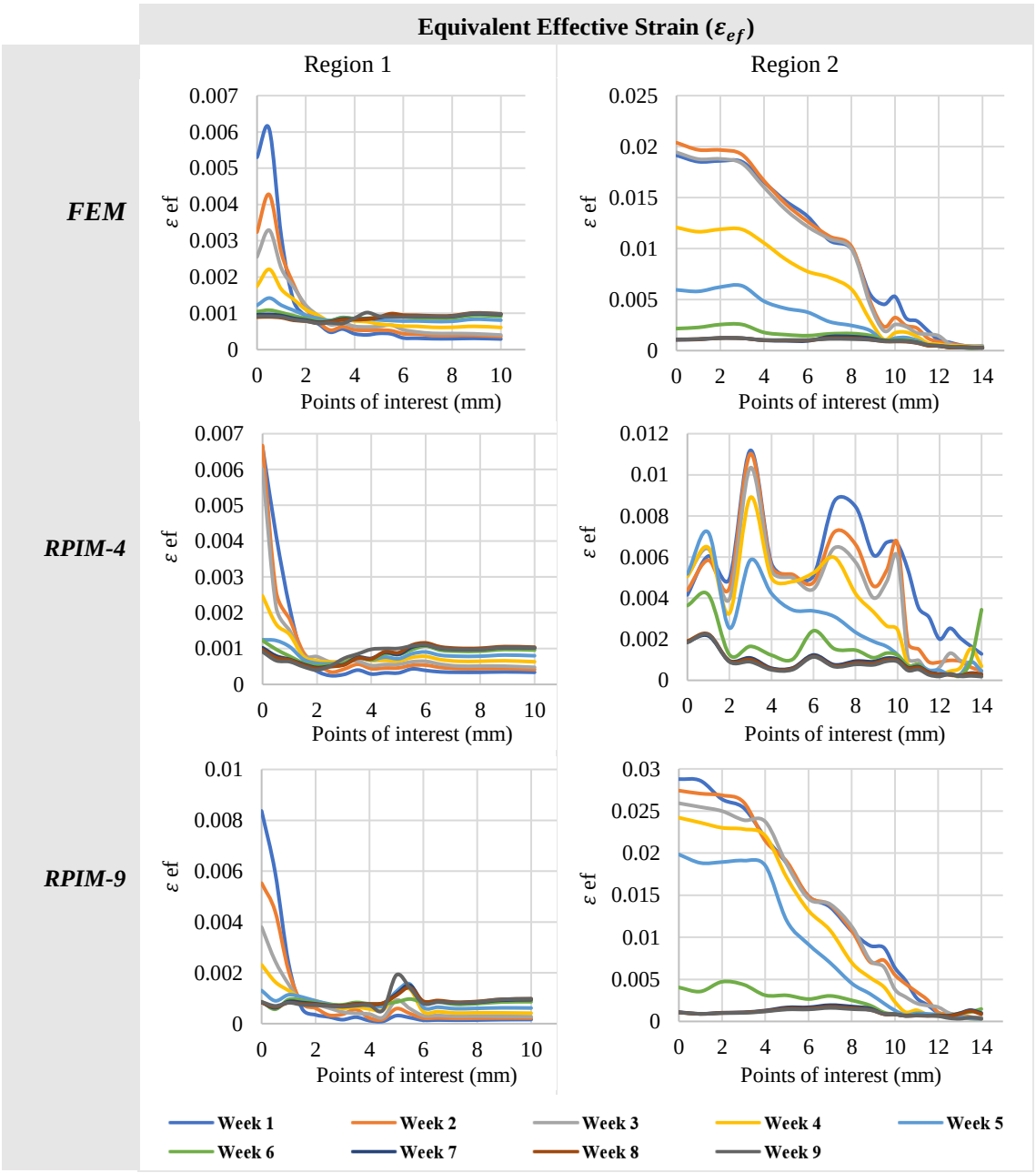

Figure 6.19- Graphical representations of the distribution of the equivalent effective strain in each week of bone regeneration along the regions 1 and 2 in FEM, RPIM-4 and RPIM-9.

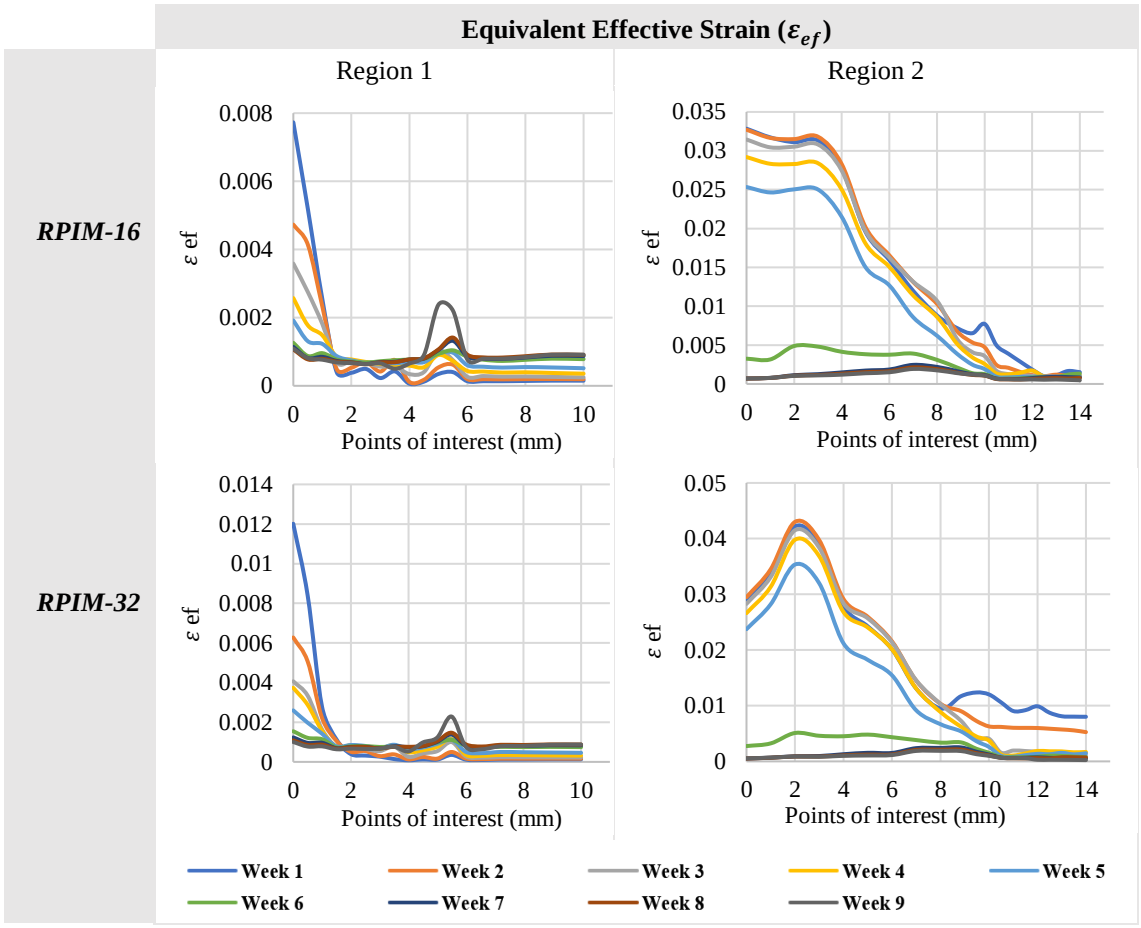

Figure 6.20- Graphical representations of the distribution of the equivalent effective strain in each week of bone regeneration along the regions 1 and 2 in RPIM-16 and RPIM-32.

In general, healing induces responses within the periosteum and external soft tissues that lead to external callus formation. Initially, bone formation occurs by intramembranous ossification in the periosteum, along the surface of the tibial cortical bone distant from the fracture gap. Afterwards, the callus enlarges in diameter and grows towards the fracture site by endochondral ossification.

Firstly, for region 1 of Figures 6.17 and 6.18, it can be observed in both FEM and RPIM that at the points of interest 0-1 mm, which belong to the fractured extremity, the von Mises effective stresses increase over the weeks of consolidation as callus passes from fibrous tissue to cartilage and woven bone. Subsequently, it can be noted that the stresses change at the interface between the periosteal callus and cortical bone. In the first four and five weeks, due to the consequent deposition of new bone by intramembranous ossification in this region, stress peaks are observed; however, as endochondral ossification starts towards the fracture gap and near the cortical bone (beginning of the

periosteal bony bridging), the von Mises effective stress decrease until nine weeks (points of interest 0-2 mm). Callus stabilisation is given by enlarging the cross-sectional area of the bridging tissue and the type of tissue present, improving structural and material properties. Initially, the bridge creates a load transfer path, mostly through the external callus. Over the progressive course of ossification, the mainline transfer is established between the fracture extremities (direct line through the cortical bone and bypasses the periosteal callus). In fact, it is reported in the literature that this reduction produced in the periosteal callus signals bone resorption by osteoclasts in the external callus and, therefore, the decrease in the size of the periosteal callus at nine weeks, as evidenced in histological images [187]. Moreover, it is reported that osteoclast activity increases from six to nine weeks [197].

Complementarily, it is perceptible that in region 2, the von Mises effective stress progressively increases throughout the weeks of consolidation in the periosteal callus areas, represented by the highest stress peaks, as compared to the remaining regions, for both FEM and RPIM-4 analyses (Figure 6.17). Similarly, the fracture gap is composed of fibrous tissue until the fifth week and, the stresses are relatively close to zero. As the ossification type transitions to endochondral, the callus increases towards the fracture site and exhibits an increase in stress until nine weeks, represented by the second-highest peaks of von Mises effective stress. Nevertheless, it should be noted that in the RPIM-9 analysis at week nine, a maximum stress peak is observed in the fracture site, specifically in the cortical gap, which due to the remodelling process new bone is formed in order to re-establish the cortical structure of the bone. In addition, when comparing RPIM-32 and RPIM-16, both showed similar behaviour to FEM, RPIM-9 and RPIM-4, differing only in the eighth and ninth week of consolidation in the cortical gap, with higher stresses than the other weeks.

In both FEM and RPIM for all influence-domains (Figures 6.19 and 6.20), the equivalent effective strains are higher in the first weeks of healing and, with the gradual stiffening of the callus, become more reduced, presenting greater strain tolerance. In fact, considering region 1, the peaks of maximum strain are visible closer to the fracture gap (point of interest 0-1 mm). In contrast, bone formation by intramembranous ossification in the external callus, along the cortical surface distant from the fracture gap, induces smaller strains in the first weeks (point of interest 2-10 mm). Additionally, in region 2, strains diminished relatively quickly with distance from the gap. The strains are high at

the fracture site due to the presence of fibrous tissue in the first weeks. These progressively decrease as bridging occurs between the fractured extremities, either first by cartilage followed by woven bone, which favours ossification of the fracture gap area. Consequently, closest to the external callus, strains are minimal. Low strain favours bone formation, whereas high strain leads to fibrous non-union [138], [139], [155].

6.1.3.2.2. Model's Stiffness Over the Healing Time

Stiffness describes the resistance of a material to deformation in response to an applied force, whereby greater stiffness implies higher resistance to deformation. It is essential in bones with a load-bearing function and, it has been shown that as bone healing progresses, stiffness increases within the healing tissue [198], [199].

The change in the overall stiffness of the model at different weeks of consolidation promotes the mechanical environment regarding the amount of motion created at the fracture site in response to the imposed displacement. Thus, greater stability provides the possibility of increasing the weight-bearing activities of the patient, consequently increasing the frequency and magnitude of applied loads.

The evolution of stiffness (k) during the regeneration period was determined from the applied displacement (δ) and the reaction force (F) at the top of the model through Eq. (6.3).

$$k = \frac{F}{\delta} \qquad \text{Eq. (6.3)}$$

As previously mentioned, a displacement of 0.01 mm along the y-axis was imposed on the model. Table 6.4 shows the reaction forces calculated from the stiffness matrix and displacement for each numerical method.

Table 6.4- Reaction forces along the y-axis in the course of bone healing obtained for each numerical method.

Healing Time (weeks)	Reaction Force (N)				
	FEM	**RPIM-4**	**RPIM-9**	**RPIM-16**	**RPIM-32**
1	-243.16	-313.007	-151.801	-135.958	-119.47
2	-314.964	-391.047	-206.083	-180.75	-155.042
3	-364.593	-460.548	-266.82	-237.681	-216.918
4	-546.473	-606.296	-386.148	-340.201	-312.28
5	-709.513	-755.121	-546.963	-480.196	-439.221
6	-789.921	-903.104	-728.459	-689.979	-663.291
7	-831.256	-973.257	-792.058	-767.651	-742.874
8	-856.203	-1004.3	-823.965	-804.221	-784.574
9	-849.612	-990.545	-820.31	-805.183	-775.642

Therefore, the stiffness was determined for each of the FEM and RPIM analyses, as shown in Figure 6.21.

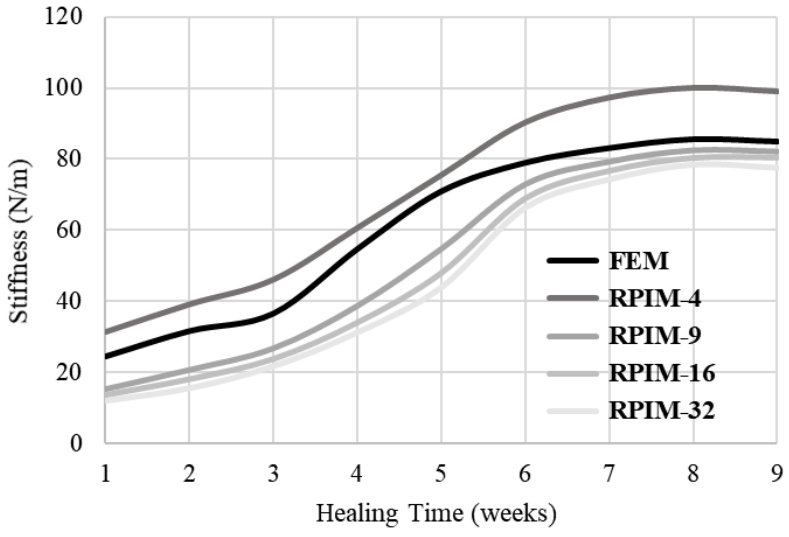

Figure 6.21- Course of model stiffness along the progression of bone healing according to the numerical method applied.

In general, there is a progressive increase in model stiffness over the weeks of bone healing as expected, which is not linear and presents a behaviour resembling a

sigmoid function (Figure 6.21). Stiffness increases throughout the regeneration process as a result of both increasing the quantity and changing the quality of repair tissues. Healing induces responses within the periosteum and external soft tissues that produce the external callus, causing a reduction of initial motion through increased stiffness.

A closer examination of the data obtained, over the first three weeks of bone healing, it is possible to observe a slow and gradual increase in stiffness, mainly due to bone formation in areas distant from the fracture gap. Subsequently, considering the beginning of endochondral ossification, with the appearance of cartilage, as well as the increase of new bone formation by intramembranous ossification both in the periosteum and near the fracture gap (periosteal bony bridging), there is a marked increase in stiffness up to six weeks. Then, with the formation of the endochondral bony bridge up to eight weeks, the increase of stiffness is more stable. Finally, close to nine weeks, the stiffness decreases due to the bone remodelling process with consequent bone resorption.

From the results produced, it is possible to note that the stiffness over the healing time was higher in the application of RPIM-4 compared to the others. Additionally, the RPIM solutions present smoother curves in relation to the FEM, with a behaviour closer to what is expected [200]. The results obtained by the meshless methods with larger influence-domains, RPIM-32, RPIM-16 and RPIM-9, are more distant from both the FEM and RPIM-4 solutions, although they present similar behaviour.

6.2. Numerical Study of Bone Remodelling in a Bone Fracture Callus

As previously mentioned, bone fracture healing is usually composed of an inflammatory phase, a reparative phase with a soft and hard callus formation, and a final remodelling phase. The reparative phase is essential to restore bone stiffness, while the remodelling phase allows the full strength of the bone to return and decreases the chance of re-fracture. It constitutes a crucial step in the fracture healing process in order to achieve complete healing.

Bone remodelling is a complex process involving a renewal of material with bone resorption followed by bone formation. In fact, once the bony bridging of the callus has occurred and reunited the extremities of the fracture, the processes of resorption and bone formation become the dominant activities in the callus. A better understanding of this

process can be achieved through mathematical modelling in order to simulate and predict experimental results.

Therefore, the current section presents the bone remodelling analyses conducted employing the remodelling algorithm of Belinha et al. [10], described in Chapter 4. These were performed on a two- and three-dimensional model and, the predicted bone distributions were then compared with the remodelling behaviour observed in histological images obtained from an *in vivo* study [5].

6.2.1. Two-Dimensional Model Analysis

6.2.1.1. Initial Conditions

In a first instance, a two-dimensional model was constructed in which the bone remodelling algorithm was validated. This model was based on the bone remodelling stage occurring at nine weeks, as described in section 6.1. After the construction of the geometric model, the problem domain was discretized in the nodal mesh presented in Figure 6.22. Subsequently, the corresponding mesh was imported to FEMAS© software. A vertical displacement was applied at the top of the model and, additionally, the node displacement was constrained both in the x direction along the line x = 0 and in the y direction along the line y = 0. Complementarily, the bone tissue assumed an isotropic behaviour, with a uniform apparent density distribution $\rho_{app}^{max} = 2.1\ g/cm^3$ and Poisson's ratio $\upsilon = 0.3$, regardless of the material direction.

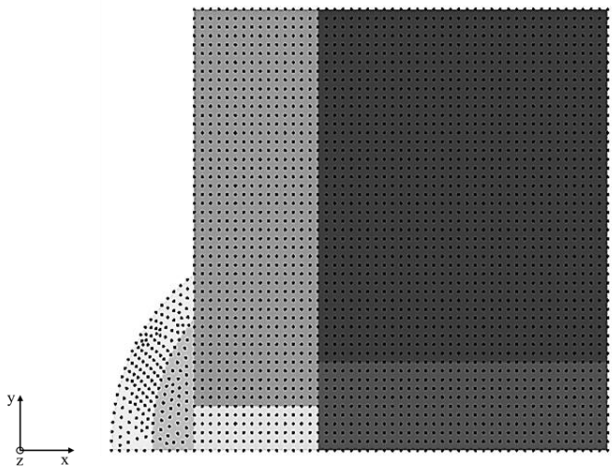

Figure 6.22- Two-dimensional model mesh with 3073 nodes.

Using Belinha's phenomenological law [10], described in section 2.3 of Chapter 2, the mechanical properties of bone tissue that depend on the updated apparent density are obtained. The strain energy field (SED) was imposed as a mechanical variable that coordinates the remodelling process. In addition, growth (α) and decay (β) rates of the apparent density of $\alpha = 0.0$ and $\beta = 0.05$ were considered in the analysis. Therefore, the density distributions were obtained by combining the bone remodelling algorithm with RPIM. In RPIM, an influence-domain of 16 nodes was defined, and the shape parameters of $c = 0.0001$, $p = 0.9999$ and a constant polynomial basis were also assumed.

6.2.1.2. Results and Discussion

Over time, in bone regeneration, the mineralisation of the soft callus proceeds from the fracture ends towards the centre of the fracture gap, forming a hard callus. After the fracture gap has been stabilized, the hard callus consisting of woven bone undergoes remodelling to its original lamellar configuration, trabecular or cortical. Thus, during remodelling, the trabecular bone density changes and is directly related to its strain energy density, and consequently, this was the criterion used in the simulation of the remodelling process, as mentioned above. In the final part of the remodelling, the superfluous bone material is resorbed, leaving behind an intact and healed bone, restoring its mechanical strength and stability. Ultimately, the process of bone remodelling will occur over several months resulting in the regeneration of normal bone structure.

Therefore, in this work, by applying the bone remodelling algorithm, the trabecular distributions are numerically obtained (Figure 6.23).

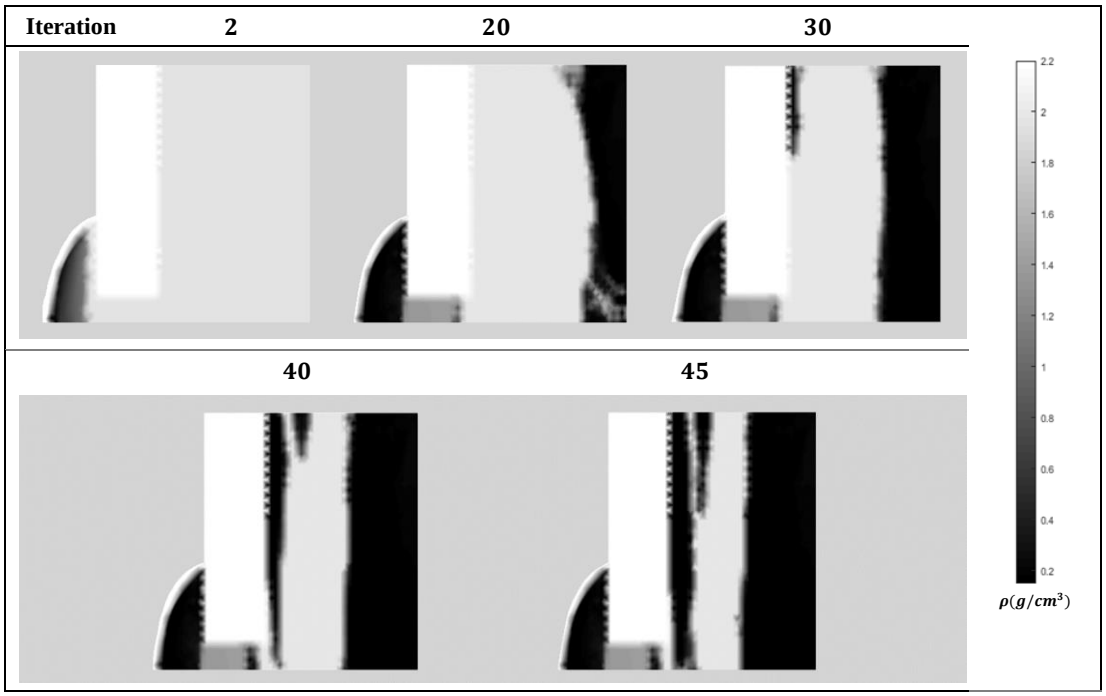

Figure 6.23- Evolution of the trabecular distribution and the corresponding apparent density obtained with RPIM in the two-dimensional model.

The evolution of the remodelling process is presented in Figure 6.23, in which the respective trabecular architecture is visible from the first steps of the iterative remodelling analysis up to the last iteration. In this figure, the evolution of the trabecular architecture is shown as grey tone isomaps, where the closest to white colour represents the considered maximum apparent density, $\rho_{app}^{max} = 2.1\ g/cm^3$, and black represents the minimum apparent density, $\rho_{app}^{min} = 0.1\ g/cm^3$. The remaining grey tones correspond to transitional apparent densities.

It is visible in the evolution of the remodelling process, the presence of a primary and secondary vertical trabeculae, between the fracture site and along the internal cavity. One of the main functions in this phase is the replacement of any callus between the fracture extremities with new bone that aligns with the mechanical load distribution [201]. In addition, the outermost regions of the periosteal callus are also subject to remodelling.

Note that for the final medium apparent density $\rho = 0.988\ g/cm^3$, one of the secondary trabeculae remains in the fracture gap close to the external callus, allowing a stabilization in the region. Therefore, the trabecular distribution obtained when compared

with the respective histological image at this stage resembles the physiological reality observed in the callus (Figure 6.24).

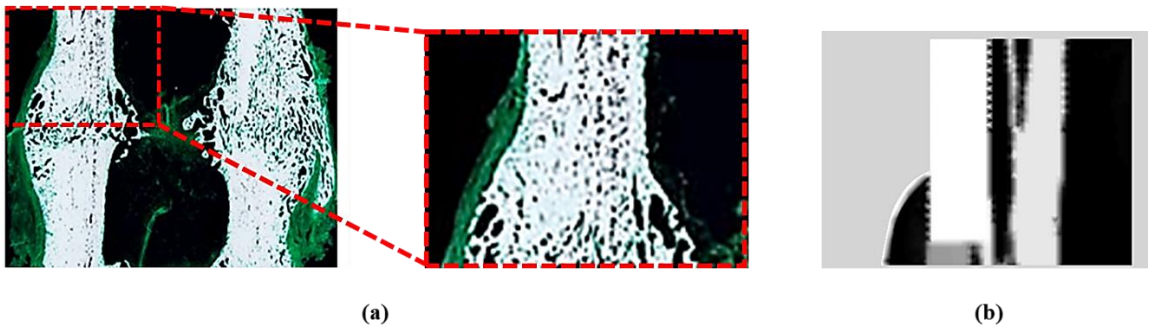

Figure 6.24- Bone distribution in the bone remodelling process occurring at nine weeks. (a) Microscopical image of the histological section with a zoom-in of the area in the red square (green: soft tissue, white: mineralized tissue) taken from the *in vivo* study [187], (b) solution obtained with the RPIM.

6.2.2. Three-Dimensional Model Analysis

6.2.2.1. Initial Conditions

Similarly to the two-dimensional analysis, the bone remodelling algorithm was tested on the three-dimensional model. This model represents the bone remodelling phase occurring at nine weeks, as described in section 6.1. The bone tissue assumed an isotropic behaviour, with a uniform apparent density distribution $\rho_{app}^{max} = 2.1\ g/cm^3$ and Poisson's ratio $\upsilon = 0.3$, regardless of the material direction. Additionally, growth (α) and decay (β) rates of the apparent density of $\alpha = 0.0$ and $\beta = 0.05$ were considered in the analysis. Therefore, the bone remodelling algorithm was combined with the RPIM. In RPIM, an influence-domain of 32 nodes was defined, and the shape parameters of $c = 0.0001$, $p = 0.9999$ and a constant polynomial basis were also assumed.

6.2.2.2. Results and Discussion

Following the same approach, the bone remodelling algorithm was applied in the three-dimensional model to numerically obtain the respective trabecular distributions. Therefore, the evolution of the remodelling process is presented in Figure 6.25, in which the trabecular architecture is visible from the first steps of the iterative remodelling

analysis until the last iteration. The final trabecular architecture is obtained with RPIM with a medium apparent density of $\rho = 1.22\ g/cm^3$.

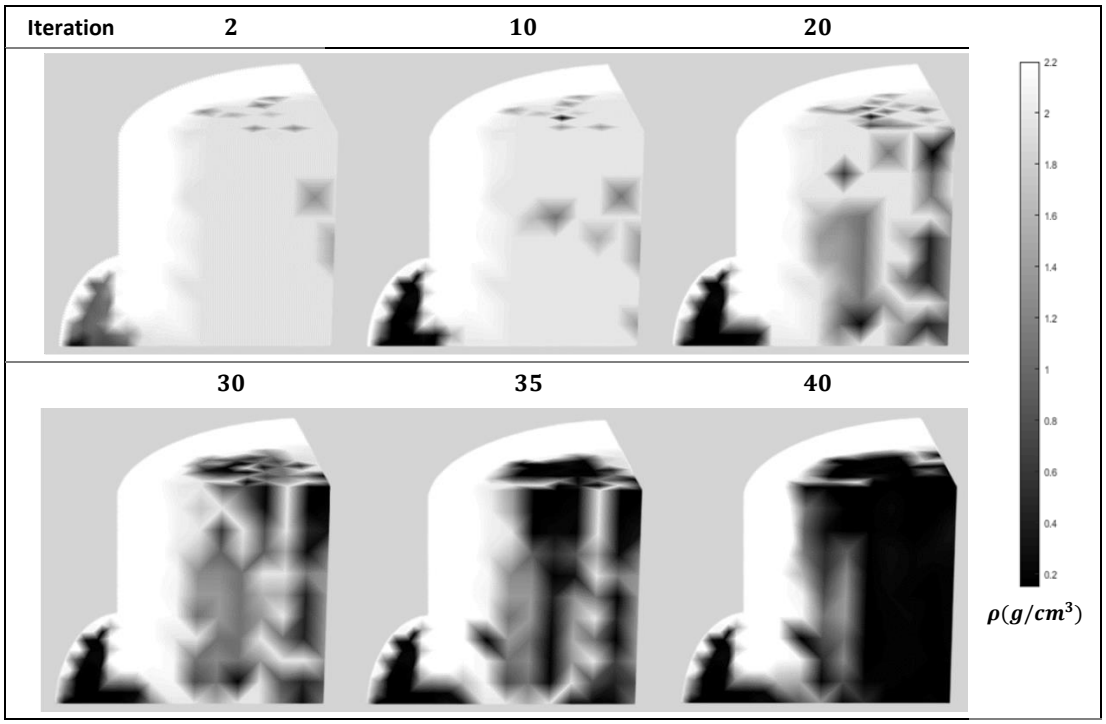

Figure 6.25- Evolution of the trabecular distribution and the corresponding apparent density obtained with RPIM in the three-dimensional model.

In the solution obtained in iteration 40 (Figure 6.25), significant changes are observed in both the fracture gap and the endosteal surface of the cortical bone. The apparent density of the callus closer to the cortical bone is higher when compared to the callus at a larger distance from the cortical surface. In fact, trabeculae formation occurs from the fracture site that extend towards the centre of the fracture, considering the imposed displacement and the heterogeneity in the mechanical properties from the periosteal to endosteal callus. Additionally, a trabecula parallel to the longitudinal axis of the model is visible near the endosteal surface of the cortical bone. The trabeculae formed provide greater mechanical strength and stability in the region.

Therefore, the histological image of the respective remodelling phase of the *in vivo* study is used in order to validate the internal trabecular distributions numerically obtained in response to the mechanical stimulus. Figure 6.26 shows the corresponding histological comparison section, outlined in red, and the final solution obtained with the

RPIM. By applying the remodelling algorithm, it was possible to reproduce structures in agreement with the experimental study, marked in yellow for better visualisation (Figure 6.26(b)). In fact, according to the qualitative histological descriptions and observations, the fracture site and the cortical bone surfaces display extensive remodelling activities. Furthermore, two different orientations of the bone tissue were observed and were related to the proximity to the fracture gap. The bone that is distant from the fracture gap presented a longitudinal orientation, and the bone adjacent to the gap was aligned in the radial direction. Complementarily, the outermost region is also subject to remodelling, as at this stage, bone resorption reduces the size of the external callus [187].

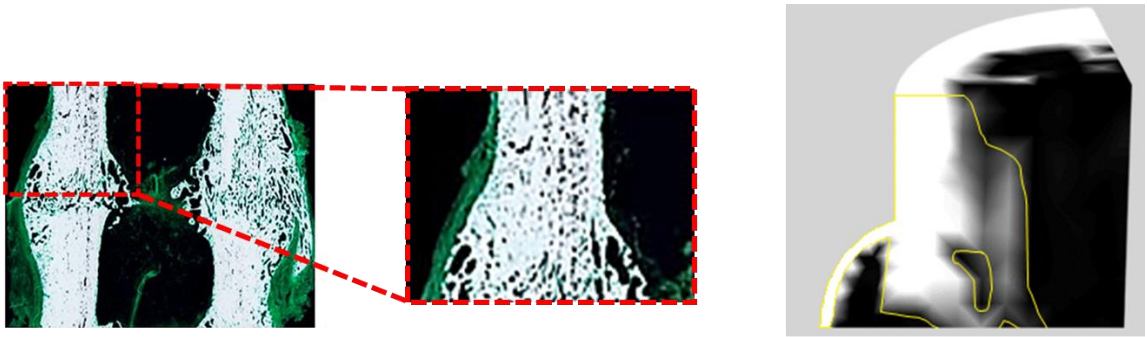

(a) (b)

Figure 6.26- Bone distribution in the bone remodelling process occurring at nine weeks. (a) Microscopical image of the histological section with a zoom-in of the area in the red square (green: soft tissue, white: mineralized tissue) taken from the *in vivo* study [187], (b) solution obtained through RPIM with the reproduced structures outlined in yellow.

Finally, this work allowed a satisfactory numerical reproduction of the trabecular distribution using a phenomenological law suitable for bone tissue, an efficient iterative remodelling algorithm, an accurate numerical method and a correct numerical model.

CHAPTER 7 – CONCLUSIONS AND FUTURE WORK

7. Conclusions and Future Work

Bone fracture healing is a complex and, at the same time, an expensive problem, mainly due to the difficulty to define a consolidation endpoint, increasing the incidence of delayed or non-unions. Consequently, it implies a significant impact on medical and hospital resources, being essential to produce answers in order to improve the adequate recovery of patients. In this context, it is essential to understand the basic biology and the mechanoregulatory mechanisms of bone regeneration and remodelling in order to develop more effective and less costly treatments.

The magnitude of mechanical stimulus at the tissue or cell level has implications on the spatial and temporal tissue distributions that define the biological repair process. Given the mechanical environment, cells act as sensors to produce active responses. Thus, experimental measurements are hampered by the determination of mechanical stimulus at wide local positions that result from the healing process. Therefore, computer simulation enables such sampling scales to produce a relevant impact in research science fields. Models require experimental validation, and therefore, it is important to select data from well-characterised experiments. However, the lack of reliable experimental data on the different bone healing stages is noteworthy.

Therefore, the present work allowed a comprehensive study of the bone healing process and the computational models developed over time. For a more detailed description of the callus during the “normal” healing process, 2D and 3D models were developed to reproduce the inherent characteristics of the bone callus in the different bone healing stages. For this, an analysis of histological sections obtained from an *in vivo* study was employed. The data allowed establishing the development of the callus geometry, the tissues arrangements in the callus, and Young’s modulus of the hard callus bone material over the healing time. Thus, using these input data for the FEM and RPIM calculations, it was possible to obtain the local stress and strain fields in the bone callus at different bone healing stages. Additionally, a curve of the stiffness versus healing time with a sigmoid pattern was obtained. Stiffness increases throughout the regeneration process due to both increasing the quantity and changing the quality of repair tissues. Using the meshless methods, the curves were smoother and in agreement with the literature.

In addition, a remodelling algorithm was applied to a 2D and 3D model in the final bone healing stage. The algorithm was combined with RPIM to validate the meshless

methods in the evaluation of bone callus remodelling. At this stage, it was possible to reproduce internal bone trabecular structures similar to the *in vivo* study.

Mathematical and numerical models test hypotheses and make simplifications in order to enable the reproduction of mechanical and biological phenomena. In this regard, the work developed involves some limitations. The first encompasses the use of only histological images of two-dimensional longitudinal sections without involving transversal histological sections of the callus and considering radial symmetry. Additionally, the experimental work is based only on sheep, making it difficult to understand the features of the healing process that are specific in a given animal species, from those that are more general and could be applied to humans. Similarly, tissue distributions within the fracture callus and the magnitudes of stress and strain can be influenced by several factors, such as the presence of disease, age, agility and cumulative global daily loading activity. Complementarily, it would be relevant to include models that go beyond linear elasticity and also consider material anisotropy.

Therefore, for a better knowledge of the bone healing process and the effects of the mechanical environment, it would be important to develop a mechanobiological model. In the long term, the implementation of a comprehensive and tested mechanobiological model in clinics would have a significant impact on medical procedures.

References

[1] F. PAUWELS, "[A new theory on the influence of mechanical stimuli on the differentiation of supporting tissue. The tenth contribution to the functional anatomy and causal morphology of the supporting structure].," *Z. Anat. Entwicklungsgesch.*, vol. 121, pp. 478–515, 1960.

[2] C. L. Ekegren, E. R. Edwards, R. De Steiger, and B. J. Gabbe, "Delayed Union and Mal-Union Following Long Bone Fracture," 2018, doi: 10.3390/ijerph15122845.

[3] C. L. Ekegren, E. R. Edwards, R. de Steiger, and B. J. Gabbe, "Incidence, costs and predictors of non-union, delayed union and mal-union following long bone fracture," *Int. J. Environ. Res. Public Health*, vol. 15, no. 12, 2018, doi: 10.3390/ijerph15122845.

[4] P. Pivonka and C. R. Dunstan, "Role of mathematical modeling in bone fracture healing," *Bonekey Rep.*, vol. 1, no. August, pp. 1–10, 2012, doi: 10.1038/bonekey.2012.221.

[5] H. Schell, D. R. Epari, J. P. Kassi, H. Bragulla, H. J. Bail, and G. N. Duda, "The course of bone healing is influenced by the initial shear fixation stability," *J. Orthop. Res.*, vol. 23, no. 5, pp. 1022–1028, 2005, doi: 10.1016/j.orthres.2005.03.005.

[6] P. Strube *et al.*, "Influence of age and mechanical stability on bone defect healing: Age reverses mechanical effects," *Bone*, vol. 42, no. 4, pp. 758–764, 2008, doi: 10.1016/j.bone.2007.12.223.

[7] L. Claes, P. Augat, G. Suger, and H. J. Wilke, "Influence of size and stability of the osteotomy gap on the success of fracture healing," *J. Orthop. Res.*, vol. 15, no. 4, pp. 577–584, 1997, doi: 10.1002/jor.1100150414.

[8] A. Serra *et al.*, "A4.7 T and B cells participate in bone repair by infiltrating the fracture callus in a two-wave fashion," *Ann. Rheum. Dis.*, vol. 74, no. Suppl 1, p. A39.1-A39, 2015, doi: 10.1136/annrheumdis-2015-207259.89.

[9] F. J. Secreto, L. H. Hoeppner, and J. J. Westendorf,

"Secreto2009_Article_WntSignalingDuringFractureRepa," 2009.

[10] J. Belinha, *Meshless Methods in Biomechanics - Bone Tissue Remodelling Analysis*. 2014.

[11] A. G. Robling, A. B. Castillo, and C. H. Turner, "Biomechanical and molecular regulation of bone remodeling," *Annu. Rev. Biomed. Eng.*, vol. 8, pp. 455–498, 2006, doi: 10.1146/annurev.bioeng.8.061505.095721.

[12] H. K. Datta, W. F. Ng, J. A. Walker, S. P. Tuck, and S. S. Varanasi, "The cell biology of bone metabolism," *J. Clin. Pathol.*, vol. 61, no. 5, pp. 577–587, 2008, doi: 10.1136/jcp.2007.048868.

[13] R. Setiawati and P. Rahardjo, "Bone Development and Growth," *Osteogenes. Bone Regen.*, pp. 1–20, 2019, doi: 10.5772/intechopen.82452.

[14] D. B. Burr, "The contribution of the organic matrix to bone's material properties," *Bone*, vol. 31, no. 1, pp. 8–11, 2002, doi: 10.1016/S8756-3282(02)00815-3.

[15] S. Weiner, W. Traub, and H. D. Wagner, "Lamellar bone: Structure-function relations," *J. Struct. Biol.*, vol. 126, no. 3, pp. 241–255, 1999, doi: 10.1006/jsbi.1999.4107.

[16] J. S. Nyman, A. Roy, X. Shen, R. L. Acuna, J. H. Tyler, and X. Wang, "The influence of water removal on the strength and toughness of cortical bone," *J. Biomech.*, vol. 39, no. 5, pp. 931–938, 2006, doi: 10.1016/j.jbiomech.2005.01.012.

[17] J. Wolff, *The Law of Bone Remodelling*. 1986.

[18] C. VanPutte, J. Regan, A. Russo, B. Manager, and A. Reed, *Seeley's Essential of Anatomy & Physiology*. 2016.

[19] S. BROWN, "Anatomy & Physiology," *Cat*, pp. 36–73, 2020, doi: 10.2307/j.ctvpwhfq5.5.

[20] E. Sornay-Rendu, S. Boutroy, F. Munoz, and P. D. Delmas, "Alterations of cortical and trabecular architecture are associated with fractures in postmenopausal women, partially independent of decreased BMD measured by DXA: The OFELY study," *J. Bone Miner. Res.*, vol. 22, no. 3, pp. 425–433, 2007, doi: 10.1359/jbmr.061206.

[21] D. Vashishth, "Collagen glycation and its role in fracture properties of bone," *J.*

Musculoskelet. Neuronal Interact., vol. 5, no. 4, p. 316, 2005.

[22] S. Viguet-Carrin, P. Garnero, and P. D. Delmas, "The role of collagen in bone strength," *Osteoporos. Int.*, vol. 17, no. 3, pp. 319–336, 2006, doi: 10.1007/s00198-005-2035-9.

[23] M. Saito, K. Fujii, S. Soshi, and T. Tanaka, "Reductions in degree of mineralization and enzymatic collagen cross-links and increases in glycation-induced pentosidine in the femoral neck cortex in cases of femoral neck fracture," *Osteoporos. Int.*, vol. 17, no. 7, pp. 986–995, 2006, doi: 10.1007/s00198-006-0087-0.

[24] S. Y. Tang, U. Zeenath, and D. Vashishth, "Effects of non-enzymatic glycation on cancellous bone fragility," *Bone*, vol. 40, no. 4, pp. 1144–1151, 2007, doi: 10.1016/j.bone.2006.12.056.

[25] R. Florencio-Silva, G. R. D. S. Sasso, E. Sasso-Cerri, M. J. Simões, and P. S. Cerri, "Biology of Bone Tissue: Structure, Function, and Factors That Influence Bone Cells," *Biomed Res. Int.*, vol. 2015, 2015, doi: 10.1155/2015/421746.

[26] J. D. Currey, "The many adaptations of bone," *J. Biomech.*, vol. 36, no. 10, pp. 1487–1495, 2003, doi: 10.1016/S0021-9290(03)00124-6.

[27] A. M. Parfitt, "The bone remodeling compartment: A circulatory function for bone lining cells," *J. Bone Miner. Res.*, vol. 16, no. 9, pp. 1583–1585, 2001, doi: 10.1359/jbmr.2001.16.9.1583.

[28] F. Yuan, S. R. Stock, D. R. Haeffner, J. D. Almer, D. C. Dunand, and L. C. Brinson, "A new model to simulate the elastic properties of mineralized collagen fibril," *Biomech. Model. Mechanobiol.*, vol. 10, no. 2, pp. 147–160, 2011, doi: 10.1007/s10237-010-0223-9.

[29] J. Y. Rho, L. Kuhn-Spearing, and P. Zioupos, "Mechanical properties and the hierarchical structure of bone," *Med. Eng. Phys.*, vol. 20, no. 2, pp. 92–102, 1998, doi: 10.1016/S1350-4533(98)00007-1.

[30] A. M. Parfitt, "Targeted and nontargeted bone remodeling: Relationship to basic multicellular unit origination and progression," *Bone*, vol. 30, no. 1, pp. 5–7, 2002, doi: 10.1016/S8756-3282(01)00642-1.

[31] S. Y. Smith and R. Samadfam, "Biochemical markers of bone turnover," *Mol. Integr. Toxicol.*, pp. 175–201, 2017, doi: 10.1007/978-3-319-56192-9_5.

[32] S. J. Mellon and K. E. Tanner, “Bone and its adaptation to mechanical loading: A review,” *Int. Mater. Rev.*, vol. 57, no. 5, pp. 235–255, 2012, doi: 10.1179/1743280412Y.0000000008.

[33] T. M. Keaveny, E. F. Morgan, O. C. Yeh, C. Material, C. Bone, and T. Bone, “Bone Mechanics,” *Lancet*, vol. 240, no. 6202, p. 43, 1942, doi: 10.1016/S0140-6736(00)62141-4.

[34] R. W. McCalden, J. A. McGlough, M. B. Barker, and C. M. Court-Brown, “Age-related changes in the tensile properties of cortical bone. The relative importance of changes in porosity, mineralization and microstructure,” *J. Bone Jt. Surg. - Ser. A*, vol. 75, no. 8, pp. 1193–1205, 1993, doi: 10.2106/00004623-199308000-00009.

[35] E. F. Morgan and T. M. Keaveny, “Dependence of yield strain of human trabecular bone on anatomic site,” *J. Biomech.*, vol. 34, no. 5, pp. 569–577, 2001, doi: 10.1016/S0021-9290(01)00011-2.

[36] B. D. Snyder, S. Piazza, W. T. Edwards, and W. C. Hayes, “Role of trabecular morphology in the etiology of age-related vertebral fractures,” *Calcif. Tissue Int.*, vol. 53, no. 1 Supplement, pp. 14–22, 1993, doi: 10.1007/BF01673396.

[37] P. Zioupos, R. B. Cook, and J. R. Hutchinson, “Some basic relationships between density values in cancellous and cortical bone,” *J. Biomech.*, vol. 41, no. 9, pp. 1961–1968, 2008, doi: 10.1016/j.jbiomech.2008.03.025.

[38] J. C. Lotz, T. N. Gerhart, and W. C. Hayes, “Mechanical properties of metaphyseal bone in the proximal femur,” *J. Biomech.*, vol. 24, no. 5, 1991, doi: 10.1016/0021-9290(91)90350-V.

[39] J. Belinha, R. M. N. Jorge, and L. M. J. S. Dinis, “A meshless microscale bone tissue trabecular remodelling analysis considering a new anisotropic bone tissue material law,” *Comput. Methods Biomech. Biomed. Engin.*, vol. 16, no. 11, pp. 1170–1184, 2013, doi: 10.1080/10255842.2012.654783.

[40] E. office Of journal “Morphologia,” *Junqueira’s Basic Histology : Text & Atlas (15th ed.), 2018*, vol. 13, no. 2. 2019.

[41] D. Bareither, *Thieme Atlas of Anatomy: General Anatomy and Musculoskeletal System*, vol. 96, no. 2. 2006.

[42] J. Tavares and N. Jorge, *Lecture Notes in Computational Vision and Biomechanics*.

2012.

[43] E. F. Eriksen, “Cellular mechanisms of bone remodeling,” *Rev. Endocr. Metab. Disord.*, vol. 11, no. 4, pp. 219–227, 2010, doi: 10.1007/s11154-010-9153-1.

[44] D. J. Hadjidakis and I. I. Androulakis, “Bone remodeling,” *Ann. N. Y. Acad. Sci.*, vol. 1092, pp. 385–396, 2006, doi: 10.1196/annals.1365.035.

[45] R. Owen and G. C. Reilly, “In vitro models of bone remodelling and associated disorders,” *Front. Bioeng. Biotechnol.*, vol. 6, no. OCT, pp. 1–22, 2018, doi: 10.3389/fbioe.2018.00134.

[46] M. O. Agerbæk, E. F. Eriksen, J. Kragstrup, L. Mosekilde, and F. Melsen, “A reconstruction of the remodelling cycle in normal human cortical iliac bone,” *Bone Miner.*, vol. 12, no. 2, pp. 101–112, 1991, doi: 10.1016/0169-6009(91)90039-3.

[47] M. F. Hauge EM, Qvesel D, Eriksen EF, Mosekilde L, “Hauge EM, Qvesel D, Eriksen EF, Mosekilde L, Melsen F. Cancellous bone remodeling occurs in specialized compartments lined by cells expressing osteoblastic markers,” *J Bone Min. Res*, vol. 16, no. 9, pp. 1575–1582., 2001.

[48] A. Y. Parra-torres, M. Valdés-flores, L. Orozco, and R. Velázquez-cruz, “Topics in Osteoporosis,” *Top. Osteoporos.*, pp. 1–28, 2013, doi: 10.5772/50259.

[49] L. J. Raggatt and N. C. Partridge, “Cellular and molecular mechanisms of bone remodeling,” *J. Biol. Chem.*, vol. 285, no. 33, pp. 25103–25108, 2010, doi: 10.1074/jbc.R109.041087.

[50] L. Xing and B. F. Boyce, “Regulation of apoptosis in osteoclasts and osteoblastic cells,” *Biochem. Biophys. Res. Commun.*, vol. 328, no. 3, pp. 709–720, 2005, doi: 10.1016/j.bbrc.2004.11.072.

[51] J. Kular, J. Tickner, S. M. Chim, and J. Xu, “An overview of the regulation of bone remodelling at the cellular level,” *Clin. Biochem.*, vol. 45, no. 12, pp. 863–873, 2012, doi: 10.1016/j.clinbiochem.2012.03.021.

[52] J. C. Gallagher and A. J. Sai, “Molecular biology of bone remodeling: Implications for new therapeutic targets for osteoporosis,” *Maturitas*, vol. 65, no. 4, pp. 301–307, 2010, doi: 10.1016/j.maturitas.2010.01.002.

[53] G. J. Atkins and D. M. Findlay, “Osteocyte regulation of bone mineral: A little

give and take," *Osteoporos. Int.*, vol. 23, no. 8, pp. 2067–2079, 2012, doi: 10.1007/s00198-012-1915-z.

[54] L. F. Bonewald, "The amazing osteocyte," *J. Bone Miner. Res.*, vol. 26, no. 2, pp. 229–238, 2011, doi: 10.1002/jbmr.320.

[55] J. S. Kenkre and J. H. D. Bassett, "The bone remodelling cycle," *Ann. Clin. Biochem.*, vol. 55, no. 3, pp. 308–327, 2018, doi: 10.1177/0004563218759371.

[56] E. Gómez-Barrena, P. Rosset, D. Lozano, J. Stanovici, C. Ermthaller, and F. Gerbhard, "Bone fracture healing: Cell therapy in delayed unions and nonunions," *Bone*, vol. 70, pp. 93–101, 2015, doi: 10.1016/j.bone.2014.07.033.

[57] L. A. Mills and A. H. R. W. Simpson, "The relative incidence of fracture non-union in the Scottish population (5.17 million): A 5-year epidemiological study," *BMJ Open*, vol. 3, no. 2, pp. 1–7, 2013, doi: 10.1136/bmjopen-2012-002276.

[58] N. K. Kanakaris and P. V. Giannoudis, "The health economics of the treatment of long-bone non-unions," *Injury*, vol. 38, no. SUPPL. 2, 2007, doi: 10.1016/S0020-1383(07)80012-X.

[59] M. Bonafede, D. Espindle, and A. G. Bower, "The direct and indirect costs of long bone fractures in a working age US population," *J. Med. Econ.*, vol. 16, no. 1, pp. 169–178, 2013, doi: 10.3111/13696998.2012.737391.

[60] E. Antonova, T. K. Le, R. Burge, and J. Mershon, "Tibia shaft fractures: Costly burden of nonunions," *BMC Musculoskelet. Disord.*, vol. 14, 2013, doi: 10.1186/1471-2474-14-42.

[61] "Fracture general principles - Startradiology." https://www.startradiology.com/the-basics/fracture-general-principles/index.html (accessed Mar. 30, 2021).

[62] L. Claes, S. Recknagel, and A. Ignatius, "Fracture healing under healthy and inflammatory conditions," *Nat. Rev. Rheumatol.*, vol. 8, no. 3, pp. 133–143, 2012, doi: 10.1038/nrrheum.2012.1.

[63] T. A. Einhorn, "Enhancement of fracture healing.," *Instr. Course Lect.*, vol. 45, pp. 401–416, 1996, doi: 10.2106/00004623-199506000-00016.

[64] A. Aydin, K. Memisoglu, A. Cengiz, H. Atmaca, B. Muezzinoglu, and U. S.

Muezzinoglu, “Effects of botulinum toxin A on fracture healing in rats: An experimental study,” *J. Orthop. Sci.*, vol. 17, no. 6, pp. 796–801, 2012, doi: 10.1007/s00776-012-0269-x.

[65] S. M. Perren, “Physical and biological aspects of fracture healing with special reference to internal fixation,” *Clin. Orthop. Relat. Res.*, vol. NO. 138, pp. 175–196, 1979.

[66] F. Shapiro, “Bone development and its relation to fracture repair. The role of mesenchymal osteoblasts and surface osteoblasts,” *Eur. Cells Mater.*, vol. 15, pp. 53–76, 2008, doi: 10.22203/eCM.v015a05.

[67] R. Marsell and T. A. Einhorn, “The biology of fracture healing,” *Injury*, vol. 42, no. 6, pp. 551–555, 2011, doi: 10.1016/j.injury.2011.03.031.

[68] H. T. Aro and E. Y. S. Chao, “Bone-healing patterns affected by loading, fracture fragment stability, fracture type, and fracture site compression,” *Clinical Orthopaedics and Related Research*, no. 293. pp. 8–17, 1993, doi: 10.1097/00003086-199308000-00003.

[69] M. Ansari, “Bone tissue regeneration: biology, strategies and interface studies,” *Prog. Biomater.*, vol. 8, no. 4, pp. 223–237, 2019, doi: 10.1007/s40204-019-00125-z.

[70] J. L. Roberts, D. N. Paglia, and H. Drissi, “Transcriptional Mechanisms of Secondary Fracture Healing,” 1914, doi: 10.1007/s11914-018-0429-9.

[71] L. Tian *et al.*, “Hybrid fracture fixation systems developed for orthopaedic applications: A general review,” *J. Orthop. Transl.*, vol. 16, no. July, pp. 1–13, 2019, doi: 10.1016/j.jot.2018.06.006.

[72] Y. C. Fung, *Biomechanics - Mechanical Properties of Living Tissues*, Second Edi. Springer US.

[73] P. K. Zysset, “A review of morphology-elasticity relationships in human trabecular bone: Theories and experiments,” *J. Biomech.*, vol. 36, no. 10, pp. 1469–1485, 2003, doi: 10.1016/S0021-9290(03)00128-3.

[74] H. Yamada, *Strength of Biological Materials*. Baltimore, MD: Williams and Wilkins, 1970.

[75] D. T. Reilly and A. H. Burstein, “The elastic and ultimate properties of compact bone tissue,” *J. Biomech.*, vol. 8, no. 6, 1975, doi: 10.1016/0021-9290(75)90075-5.

[76] J. Seto, H. S. Gupta, P. Zaslansky, H. D. Wagner, and P. Fratzl, “Tough lessons from bone: Extreme mechanical anisotropy at the mesoscale,” *Adv. Funct. Mater.*, vol. 18, no. 13, pp. 1905–1911, 2008, doi: 10.1002/adfm.200800214.

[77] J. D. Currey, “Bones : structure and mechanics,” p. 436, 2002.

[78] L. J. Gibson and M. F. Ashby, “Cellular Solids,” 1997, doi: 10.1017/CBO9781139878326).

[79] P. L. Leong and E. F. Morgan, “Measurement of fracture callus material properties via nanoindentation,” *Acta Biomater.*, vol. 4, no. 5, pp. 1569–1575, 2008, doi: 10.1016/j.actbio.2008.02.030.

[80] H. RY and L. JL, “Mechanical properties of the fibrous tissue found at the bone-cement interface following total joint replacement,” *J. Biomed. Mater. Res.*, vol. 16, no. 6, pp. 911–927, 1982, doi: 10.1002/JBM.820160615.

[81] X. Wei, T. Räsänen, and K. Messner, “Maturation-related compressive properties of rabbit knee articular cartilage and volume fraction of subchondral tissue,” *Osteoarthr. Cartil.*, vol. 6, no. 6, pp. 400–409, 1998, doi: 10.1053/joca.1998.0143.

[82] L. A. Setton, C. Mow, F. J. Muller, J. C. Pita, and D. S. Howell, “Mechanical behavior and biochemical composition of canine knee cartilage following periods of joint disuse and disuse with remobilization,” *Osteoarthr. Cartil.*, vol. 5, no. 1, pp. 1–16, 1997, doi: 10.1016/S1063-4584(97)80027-1.

[83] J. D. Hoffman, *Numerical Methods for Engineers and Scientists.*, 2e ed. New York: Taylor & Francis., 2001.

[84] D. D. Ganji, “Numerical and Analytical Solutions for Solving Nonlinear Equations in Heat Transfer,” 2018.

[85] C. Kuehn, *Numerical methods*, vol. 191. 2015.

[86] R. Trobec and G. Kosec, *Parallel scientific computing: Theory, algorithms, and applications of mesh based and meshless methods*, vol. 0, no. 9783319170725. 2015.

[87] E. Y. K. Ng, H. S. Borovetz, E. Soudah, and Z. Sun, “Numerical methods and applications in biomechanical modeling,” *Comput. Math. Methods Med.*, vol. 2013, pp. 2–4, 2013, doi: 10.1155/2013/727830.

[88] A. Hrennikoff, “Solution of Problems of Elasticity by the Framework Method,” *J. Appl. Mech.*, vol. 8, no. 4, pp. A169–A175, 1941, doi: 10.1115/1.4009129.

[89] R. Courant, “Variational methods for the solution of problems of equilibrium and vibrations,” *Bull. Am. Math. Soc.*, vol. 49, no. 1, pp. 1–23, 1943, doi: bams/1183504922.

[90] R. W. Clough, *The Finite Element Method in Plane Stress Analysis*. American Society of Civil Engineers, 1960.

[91] E. Oñate and A. Larese, “Master of Science in Computacional Mechanics INTRODUCTION TO,” no. October, 2008.

[92] J. Fish, *A first course in finite elements*, vol. 45, no. 06. 2008.

[93] I. Marter, “Handling different h and p refinements in the framework of Spectral Difference Method,” pp. 1–85, 2013.

[94] “Finite Element Mesh Refinement Definition and Techniques.” [Online]. Available: https://www.comsol.com/multiphysics/mesh-refinement.

[95] S. Garg and M. Pant, “Meshfree Methods: A Comprehensive Review of Applications,” *Int. J. Comput. Methods*, vol. 15, no. 4, 2018, doi: 10.1142/S0219876218300015.

[96] H. Li and S. S. Mulay, *Meshless Methods and Their Numerical Properties*. 2013.

[97] T. Belytschko, Y. Krongauz, D. Organ, M. Fleming, and P. Krysl, “Meshless methods: An overview and recent developments,” *Comput. Methods Appl. Mech. Eng.*, vol. 139, no. 1–4, pp. 3–47, 1996, doi: 10.1016/S0045-7825(96)01078-X.

[98] G. R. Liu, “Meshfree Methods : Moving Beyond the Finite Element Method, Second Edition,” *Meshfree Methods*, 2009, doi: 10.1201/9781420082104.

[99] S. Li and W. K. Liu, “Meshfree and particle methods and their applications,” *Appl. Mech. Rev.*, vol. 55, no. 1, pp. 1–34, 2002, doi: 10.1115/1.1431547.

[100] R. A. Gingold and J. J. Monaghan, “Smoothed particle hydrodynamics: theory and application to non-spherical stars,” *Mon. Not. R. Astron. Soc.*, vol. 181, no. 3, pp.

375–389, 1977, doi: 10.1093/MNRAS/181.3.375.

[101] E. Oñate, S. Idelsohn, O. C. Zienkiewicz, and R. L. Taylor, “A finite point method in computational mechanics. Applications to convective transport and fluid flow,” *Int. J. Numer. Methods Eng.*, vol. 39, no. 22, pp. 3839–3866, 1996, doi: 10.1002/(SICI)1097-0207(19961130)39:22<3839::AID-NME27>3.0.CO;2-R.

[102] T. J. Liszka, C. A. M. Duarte, and W. W. Tworzydlo, “hp-Meshless cloud method,” *Comput. Methods Appl. Mech. Eng.*, vol. 139, no. 1–4, pp. 263–288, 1996, doi: 10.1016/S0045-7825(96)01086-9.

[103] X. Zhang, X. H. Liu, K. Z. Song, and M. W. Lu, “Least-squares collocation meshless method,” *Int. J. Numer. Methods Eng.*, vol. 51, no. 9, pp. 1089–1100, 2001, doi: 10.1002/nme.200.

[104] B. Nayroles, G. Touzot, and P. Villon, “Generalizing the finite element method: Diffuse approximation and diffuse elements,” *Comput. Mech.*, vol. 10, no. 5, pp. 307–318, 1992, doi: 10.1007/BF00364252.

[105] T. Belytschko, L. Gu, and Y. Y. Lu, “Fracture and crack growth by element free Galerkin methods,” *Model. Simul. Mater. Sci. Eng.*, vol. 2, no. 3 A, pp. 519–534, 1994, doi: 10.1088/0965-0393/2/3A/007.

[106] T. Belytschko, Y. Y. Lu, L. Gu, and M. Tabbara, “Element-free galerkin methods for static and dynamic fracture,” *Int. J. Solids Struct.*, vol. 32, no. 17–18, pp. 2547–2570, 1995, doi: 10.1016/0020-7683(94)00282-2.

[107] W. K. Liu and S. Jun, “Multiple-scale reproducing kernel particle methods for large deformation problems,” *Int. J. Numer. Methods Eng.*, vol. 41, no. 7, pp. 1339–1362, 1998, doi: 10.1002/(SICI)1097-0207(19980415)41:7<1339::AID-NME343>3.0.CO;2-9.

[108] S. N. Atluri, H. T. Liu, and Z. D. Han, “Meshless Local Petrov-Galerkin (MLPG) mixed collocation method for elasticity problems,” *C. - Comput. Model. Eng. Sci.*, vol. 14, no. 3, pp. 141–152, 2006, doi: 10.3970/cmes.2006.014.141.

[109] S. N. Atluri, H. T. Liu, and Z. D. Han, “Meshless Local Petrov-Galerkin (MLPG) mixed finite difference method for solid mechanics,” *C. - Comput. Model. Eng. Sci.*, vol. 15, no. 1, pp. 1–16, 2006, doi: 10.3970/cmes.2006.015.001.

[110] G. R. Liu and Y. T. Gu, “A point interpolation method for two-dimensional solids,”

Int. J. Numer. Methods Eng., vol. 50, no. 4, pp. 937–951, 2001, doi: 10.1002/1097-0207(20010210)50:4<937::AID-NME62>3.0.CO;2-X.

[111] G. R. Liu, "A point assembly method for stress analysis for two-dimensional solids," *Int. J. Solids Struct.*, vol. 39, no. 1, pp. 261–276, 2001, doi: 10.1016/S0020-7683(01)00172-X.

[112] J. G. Wang and G. R. Liu, "A point interpolation meshless method based on radial basis functions," *Int. J. Numer. Methods Eng.*, vol. 54, no. 11, pp. 1623–1648, 2002, doi: 10.1002/nme.489.

[113] N. Sukumar, B. Moran, A. Y. Semenov, and V. V. Belikov, "Natural neighbour Galerkin methods," *Int. J. Numer. Methods Eng.*, vol. 50, no. 1, pp. 1–27, 2000, doi: 10.1002/1097-0207(20010110)50:1<1::AID-NME14>3.0.CO;2-P.

[114] N. Sukumar, B. Moran, and T. Belytschko, "The natural element method in solid mechanics," *Int. J. Numer. Methods Eng.*, vol. 43, no. 5, pp. 839–887, 1998, doi: 10.1002/(SICI)1097-0207(19981115)43:5<839::AID-NME423>3.0.CO;2-R.

[115] S. R. Idelsohn, E. Oñate, N. Calvo, and F. Del Pin, "The meshless finite element method," *Int. J. Numer. Methods Eng.*, vol. 58, no. 6, pp. 893–912, 2003, doi: 10.1002/NME.798.

[116] R. L. Hardy, "Theory and applications of the multiquadric-biharmonic method 20 years of discovery 1968-1988," *Comput. Math. with Appl.*, vol. 19, no. 8–9, pp. 163–208, 1990, doi: 10.1016/0898-1221(90)90272-L.

[117] L. M. J. S. Dinis, R. M. Natal Jorge, and J. Belinha, "Analysis of 3D solids using the natural neighbour radial point interpolation method," *Comput. Methods Appl. Mech. Eng.*, vol. 196, no. 13–16, pp. 2009–2028, 2007, doi: 10.1016/j.cma.2006.11.002.

[118] L. M. J. S. Dinis, R. M. Natal Jorge, and J. Belinha, "Analysis of plates and laminates using the natural neighbour radial point interpolation method," *Eng. Anal. Bound. Elem.*, vol. 32, no. 3, pp. 267–279, 2008, doi: 10.1016/j.enganabound.2007.08.006.

[119] S. Moreira, J. Belinha, L. M. J. S. Dinis, and R. M. N. Jorge, "Analysis of laminated beams using the natural neighbour radial point interpolation method," *Rev. Int. Métodos Numéricos para Cálculo y Diseño en Ing.*, vol. 30, no. 2, pp. 108–120,

2014, doi: 10.1016/J.RIMNI.2013.02.002.

[120] L. M. J. S. Dinis, R. M. Natal Jorge, and J. Belinha, “The natural neighbour radial point interpolation method: Dynamic applications,” *Eng. Comput. (Swansea, Wales)*, vol. 26, no. 8, pp. 911–949, 2009, doi: 10.1108/02644400910996835.

[121] E. Sancaktar, *Mechanics of solids and structures*, vol. 10 PART A, no. 2. 2008.

[122] D. R. Carter, D. P. Fyhrie, and R. T. Whalen, “Trabecular bone density and loading history: Regulation of connective tissue biology by mechanical energy,” *J. Biomech.*, vol. 20, no. 8, 1987, doi: 10.1016/0021-9290(87)90058-3.

[123] J. Eyckmans, T. Boudou, X. Yu, and C. S. Chen, “A Hitchhiker’s Guide to Mechanobiology,” *Dev. Cell*, vol. 21, no. 1, pp. 35–47, 2011, doi: 10.1016/j.devcel.2011.06.015.

[124] G. Civelekoglu-Scholey and J. M. Scholey, “Mitotic force generators and chromosome segregation,” *Cell. Mol. Life Sci.*, vol. 67, no. 13, pp. 2231–2250, 2010, doi: 10.1007/s00018-010-0326-6.

[125] J. Renkawitz and M. Sixt, “Mechanisms of force generation and force transmission during interstitial leukocyte migration,” *EMBO Rep.*, vol. 11, no. 10, pp. 744–750, 2010, doi: 10.1038/embor.2010.147.

[126] C. Kung, “A possible unifying principle for mechanosensation,” *Nature*, vol. 436, no. 7051, pp. 647–654, 2005, doi: 10.1038/nature03896.

[127] B. F. Keele *et al.*, “Identification and characterization of transmitted and early founder virus envelopes in primary HIV-1 infection,” *Proc. Natl. Acad. Sci. U. S. A.*, vol. 105, no. 21, pp. 7552–7557, 2008, doi: 10.1073/pnas.0802203105.

[128] T. A. Einhorn and L. C. Gerstenfeld, “Fracture healing: Mechanisms and interventions,” *Nat. Rev. Rheumatol.*, vol. 11, no. 1, pp. 45–54, 2015, doi: 10.1038/nrrheum.2014.164.

[129] B. McKibbin, “The biology of fracture healing in long bones,” *J. Bone Jt. Surg.*, vol. 60, no. 2, pp. 150–62, 1978, doi: 10.1007/978-1-4471-5451-8_139.

[130] E. F. Morgan *et al.*, “Correlations between local strains and tissue phenotypes in an experimental model of skeletal healing,” *J. Biomech.*, vol. 43, no. 12, pp. 2418–2424, 2010, doi: 10.1016/j.jbiomech.2010.04.019.

[131] C. J. Moran, A. Ramesh, P. A. J. Brama, J. M. O'Byrne, F. J. O'Brien, and T. J. Levingstone, "The benefits and limitations of animal models for translational research in cartilage repair," *J. Exp. Orthop.*, vol. 3, no. 1, pp. 1–12, 2016, doi: 10.1186/s40634-015-0037-x.

[132] M. C. H. Van der Meulen and R. Huiskes, "Why mechanobiology? A survey article," *J. Biomech.*, vol. 35, no. 4, pp. 401–414, 2002, doi: 10.1016/S0021-9290(01)00184-1.

[133] M. S. Ghiasi, J. Chen, A. Vaziri, E. K. Rodriguez, and A. Nazarian, "Bone fracture healing in mechanobiological modeling: A review of principles and methods," *Bone Reports*, vol. 6, pp. 87–100, 2017, doi: 10.1016/j.bonr.2017.03.002.

[134] A. Boccaccio and C. Pappalettere, "Mechanobiology of Fracture Healing: Basic Principles and Applications in Orthodontics and Orthopaedics," *Theor. Biomech.*, 2011, doi: 10.5772/19420.

[135] P. Weinans, H and Prendergast, "Tissue Adaptation as a Dynamical Process Far," *Bone*, vol. 19, no. 2, pp. 143–149, 1996.

[136] G. Kumar and B. Narayan, "The influence of induced micromovent upon the healing of experimental tibial fractures," *Class. Pap. Orthop.*, pp. 499–501, 2014, doi: 10.1007/978-1-4471-5451-8_131.

[137] D. C. Betts and R. Müller, "Mechanical regulation of bone regeneration: Theories, models, and experiments," *Front. Endocrinol. (Lausanne).*, vol. 5, no. DEC, pp. 1–15, 2014, doi: 10.3389/fendo.2014.00211.

[138] D. R. Carter, P. R. Blenman, and G. S. Beaupré, "Correlations between mechanical stress history and tissue differentiation in initial fracture healing," *J. Orthop. Res.*, vol. 6, no. 5, pp. 736–748, 1988, doi: 10.1002/jor.1100060517.

[139] D. R. Carter, G. S. Beaupré, N. J. Giori, and J. A. Helms, "Mechanobiology of skeletal regeneration," *Clin. Orthop. Relat. Res.*, no. 355 SUPPL., 1998, doi: 10.1097/00003086-199810001-00006.

[140] P. R. Blenman, D. R. Carter, and G. S. Beaupré, "Role of mechanical loading in the progressive ossification of a fracture callus," *J. Orthop. Res.*, vol. 7, no. 3, pp. 398–407, 1989, doi: 10.1002/jor.1100070312.

[141] E. G. Loboa, G. S. Beaupré, and D. R. Carter, "Mechanobiology of initial

pseudarthrosis formation with oblique fractures," *J. Orthop. Res.*, vol. 19, no. 6, pp. 1067–1072, 2001, doi: 10.1016/S0736-0266(01)00028-6.

[142] T. N. Gardner, S. Mishra, and L. Marks, "The role of osteogenic index, octahedral shear stress and dilatational stress in the ossification of a fracture callus," *Med. Eng. Phys.*, vol. 26, no. 6, pp. 493–501, 2004, doi: 10.1016/j.medengphy.2004.03.009.

[143] E. F. Morgan, M. T. Longaker, and D. R. Carter, "Relationships between tissue dilatation and differentiation in distraction osteogenesis," *Matrix Biol.*, vol. 25, no. 2, pp. 94–103, 2006, doi: 10.1016/j.matbio.2005.10.006.

[144] L. E. Claes and C. A. Heigele, "Magnitudes of local stress and strain along bony surfaces predict the course and type of fracture healing," *J. Biomech.*, vol. 32, no. 3, pp. 255–266, 1999, doi: 10.1016/S0021-9290(98)00153-5.

[145] L. E. Claes *et al.*, "Effects of mechanical factors on the fracture healing process," *Clin. Orthop. Relat. Res.*, no. 355 SUPPL., 1998, doi: 10.1097/00003086-199810001-00015.

[146] C. Ament and E. P. Hofer, "A fuzzy logic model of fracture healing," *J. Biomech.*, vol. 33, no. 8, pp. 961–968, 2000, doi: 10.1016/S0021-9290(00)00049-X.

[147] U. Simon, P. Augat, and L. Claes, *3D fracture healing model can help to explain delayed healing with interfragmentary shear movement compared to axial movement*. 2004.

[148] S. J. Shefelbine, P. Augat, L. Claes, and U. Simon, "Trabecular bone fracture healing simulation with finite element analysis and fuzzy logic," *J. Biomech.*, vol. 38, no. 12, pp. 2440–2450, 2005, doi: 10.1016/j.jbiomech.2004.10.019.

[149] M. A. Biot, "General theory of three-dimensional consolidation," *J. Appl. Phys.*, vol. 12, no. 2, pp. 155–164, 1941, doi: 10.1063/1.1712886.

[150] V. C. Mow, S. C. Kuei, W. M. Lai, and C. G. Armstrong, "Biphasic creep and stress relaxation of articular cartilage in compression: Theory and experiments," *J. Biomech. Eng.*, vol. 102, no. 1, pp. 73–84, 1980, doi: 10.1115/1.3138202.

[151] P. J. Prendergast, W. D. Van Driel, and J. H. Kuiper, "A comparison of finite element codes for the solution of biphasic poroelastic problems," *Proc. Inst. Mech. Eng. Part H J. Eng. Med.*, vol. 210, no. 2, pp. 131–136, 1996, doi:

10.1243/PIME_PROC_1996_210_402_02.

[152] A. Torcasio, G. H. van Lenthe, and H. Van Oosterwyck, “The importance of loading frequency, rate and vibration for enhancing bone adaptation and implant osseointegration.,” *Eur. Cell. Mater.*, vol. 16, pp. 56–68, Nov. 2008.

[153] C. R. Jacobs, C. E. Yellowley, B. R. Davis, Z. Zhou, J. M. Cimbala, and H. J. Donahue, “Differential effect of steady versus oscillating flow on bone cells,” *J. Biomech.*, vol. 31, no. 11, pp. 969–976, 1998, doi: 10.1016/S0021-9290(98)00114-6.

[154] P. J. Prendergast, “Finite element models in tissue mechanics and orthopaedic implant design,” *Clin. Biomech.*, vol. 12, no. 6, pp. 343–366, 1997, doi: 10.1016/S0268-0033(97)00018-1.

[155] P. J. Prendergast, R. Huiskes, and K. Søballe, “Biophysical stimuli on cells during tissue differentiation at implant interfaces,” *J. Biomech.*, vol. 30, no. 6, pp. 539–548, 1997, doi: 10.1016/S0021-9290(96)00140-6.

[156] H. Isaksson *et al.*, “Bone regeneration during distraction osteogenesis: Mechano-regulation by shear strain and fluid velocity,” *J. Biomech.*, vol. 40, no. 9, pp. 2002–2011, 2007, doi: 10.1016/j.jbiomech.2006.09.028.

[157] D. Lacroix and P. J. Prendergast, “A mechano-regulation model for tissue differentiation during fracture healing: Analysis of gap size and loading,” *J. Biomech.*, vol. 35, no. 9, pp. 1163–1171, 2002, doi: 10.1016/S0021-9290(02)00086-6.

[158] D. P. Byrne, D. Lacroix, and P. J. Prendergast, “Simulation of fracture healing in the tibia: Mechanoregulation of cell activity using a lattice modeling approach,” *J. Orthop. Res.*, vol. 29, no. 10, pp. 1496–1503, 2011, doi: 10.1002/jor.21362.

[159] L. Geris *et al.*, “Numerical simulation of tissue differentiation around loaded titanium implants in a bone chamber,” *J. Biomech.*, vol. 37, no. 5, pp. 763–769, 2004, doi: 10.1016/j.jbiomech.2003.09.026.

[160] D. J. Kelly and P. J. Prendergast, “Mechano-regulation of stem cell differentiation and tissue regeneration in osteochondral defects,” *J. Biomech.*, vol. 38, no. 7, pp. 1413–1422, 2005, doi: 10.1016/j.jbiomech.2004.06.026.

[161] A. Bailón-Plaza and M. C. H. Van Der Meulen, “Beneficial effects of moderate,

early loading and adverse effects of delayed or excessive loading on bone healing," *J. Biomech.*, vol. 36, no. 8, pp. 1069–1077, 2003, doi: 10.1016/S0021-9290(03)00117-9.

[162] S. Checa and P. J. Prendergast, "A mechanobiological model for tissue differentiation that includes angiogenesis: A lattice-based modeling approach," *Ann. Biomed. Eng.*, vol. 37, no. 1, pp. 129–145, 2009, doi: 10.1007/s10439-008-9594-9.

[163] L. Geris, J. Vander Sloten, and H. Van Oosterwyck, "Connecting biology and mechanics in fracture healing: An integrated mathematical modeling framework for the study of nonunions," *Biomech. Model. Mechanobiol.*, vol. 9, no. 6, pp. 713–724, 2010, doi: 10.1007/s10237-010-0208-8.

[164] A. Carlier, N. van Gastel, L. Geris, G. Carmeliet, and H. Van Oosterwyck, "Size Does Matter: An Integrative In Vivo-In Silico Approach for the Treatment of Critical Size Bone Defects," *PLoS Comput. Biol.*, vol. 10, no. 11, 2014, doi: 10.1371/journal.pcbi.1003888.

[165] H. Isaksson, W. Wilson, C. C. van Donkelaar, R. Huiskes, and K. Ito, "Comparison of biophysical stimuli for mechano-regulation of tissue differentiation during fracture healing," *J. Biomech.*, vol. 39, no. 8, pp. 1507–1516, 2006, doi: 10.1016/j.jbiomech.2005.01.037.

[166] S. Irandoust and S. Muftu, "Computer simulation of dental implant treatments," *2015 41st Annu. Northeast Biomed. Eng. Conf. NEBEC 2015*, pp. 2–3, 2015, doi: 10.1109/NEBEC.2015.7117097.

[167] M. J. Gómez-Benito, J. M. García-Aznar, J. H. Kuiper, and M. Doblaré, "Influence of fracture gap size on the pattern of long bone healing: A computational study," *J. Theor. Biol.*, vol. 235, no. 1, pp. 105–119, 2005, doi: 10.1016/j.jtbi.2004.12.023.

[168] F. O. Ribeiro, M. J. Gómez-Benito, J. Folgado, P. R. Fernandes, and J. M. García-Aznar, "In silico mechano-chemical model of bone healing for the regeneration of critical defects: The effect of BMP-2," *PLoS One*, vol. 10, no. 6, pp. 1–25, 2015, doi: 10.1371/journal.pone.0127722.

[169] W. Wilson, C. C. Van Donkelaar, B. Van Rietbergen, and R. Huiskes, "A fibril-reinforced poroviscoelastic swelling model for articular cartilage," *J. Biomech.*,

vol. 38, no. 6, pp. 1195–1204, 2005, doi: 10.1016/j.jbiomech.2004.07.003.

[170] J. M. García-Aznar, J. H. Kuiper, M. J. Gómez-Benito, M. Doblaré, and J. B. Richardson, "Computational simulation of fracture healing: Influence of interfragmentary movement on the callus growth," *J. Biomech.*, vol. 40, no. 7, pp. 1467–1476, 2007, doi: 10.1016/j.jbiomech.2006.06.013.

[171] H. Isaksson, "Recent advances in mechanobiological modeling of bone regeneration," *Mech. Res. Commun.*, vol. 42, pp. 22–31, 2012, doi: 10.1016/j.mechrescom.2011.11.006.

[172] A. Bailón-Plaza and M. C. H. Van Der Meulen, "A mathematical framework to study the effects of growth factor influences on fracture healing," *J. Theor. Biol.*, vol. 212, no. 2, pp. 191–209, 2001, doi: 10.1006/jtbi.2001.2372.

[173] L. Geris, A. Gerisch, J. Vander Sloten, R. Weiner, and H. Van Oosterwyck, "Angiogenesis in bone fracture healing: A bioregulatory model," *J. Theor. Biol.*, vol. 251, no. 1, pp. 137–158, 2008, doi: 10.1016/j.jtbi.2007.11.008.

[174] H. Isaksson, C. C. van Donkelaar, R. Huiskes, and K. Ito, "A mechano-regulatory bone-healing model incorporating cell-phenotype specific activity," *J. Theor. Biol.*, vol. 252, no. 2, pp. 230–246, 2008, doi: 10.1016/j.jtbi.2008.01.030.

[175] H. Isaksson, C. C. van Donkelaar, R. Huiskes, J. Yao, and K. Ito, "Determining the most important cellular characteristics for fracture healing using design of experiments methods," *J. Theor. Biol.*, vol. 255, no. 1, pp. 26–39, 2008, doi: 10.1016/j.jtbi.2008.07.037.

[176] M. A. Pérez and P. J. Prendergast, "Random-walk models of cell dispersal included in mechanobiological simulations of tissue differentiation," *J. Biomech.*, vol. 40, no. 10, pp. 2244–2253, 2007, doi: 10.1016/j.jbiomech.2006.10.020.

[177] N. C. Keramaris, G. M. Calori, V. S. Nikolaou, E. H. Schemitsch, and P. V. Giannoudis, "Fracture vascularity and bone healing: A systematic review of the role of VEGF," *Injury*, vol. 39, no. SUPPL.2, 2008, doi: 10.1016/S0020-1383(08)70015-9.

[178] L. Geris *et al.*, "Mathematical modeling of fracture healing in mice: Comparison between experimental data and numerical simulation results," *Med. Biol. Eng. Comput.*, vol. 44, no. 4, pp. 280–289, 2006, doi: 10.1007/s11517-006-0040-6.

[179] S. Checa and P. J. Prendergast, “Effect of cell seeding and mechanical loading on vascularization and tissue formation inside a scaffold: A mechano-biological model using a lattice approach to simulate cell activity,” *J. Biomech.*, vol. 43, no. 5, pp. 961–968, 2010, doi: 10.1016/j.jbiomech.2009.10.044.

[180] S. Checa, P. J. Prendergast, and G. N. Duda, “Inter-species investigation of the mechano-regulation of bone healing: Comparison of secondary bone healing in sheep and rat,” *J. Biomech.*, vol. 44, no. 7, pp. 1237–1245, 2011, doi: 10.1016/j.jbiomech.2011.02.074.

[181] D. P. Burke and D. J. Kelly, “Substrate stiffness and oxygen as regulators of stem cell differentiation during skeletal tissue regeneration: A mechanobiological model,” *PLoS One*, vol. 7, no. 7, 2012, doi: 10.1371/journal.pone.0040737.

[182] D. Burke, M. Dishowitz, M. Sweetwyne, E. Miedel, K. D. Hankenson, and D. J. Kelly, “The role of oxygen as a regulator of stem cell fate during fracture repair in TSP2-null mice,” *J. Orthop. Res.*, vol. 31, no. 10, pp. 1585–1596, 2013, doi: 10.1002/jor.22396.

[183] A. Carlier, L. Geris, N. van Gastel, G. Carmeliet, and H. Van Oosterwyck, “Oxygen as a critical determinant of bone fracture healing-A multiscale model,” *J. Theor. Biol.*, vol. 365, pp. 247–264, 2015, doi: 10.1016/j.jtbi.2014.10.012.

[184] M. S. Ghiasi, J. E. Chen, E. K. Rodriguez, A. Vaziri, and A. Nazarian, “Computational modeling of human bone fracture healing affected by different conditions of initial healing stage,” *BMC Musculoskelet. Disord.*, vol. 20, no. 1, pp. 1–14, 2019, doi: 10.1186/s12891-019-2854-z.

[185] T. N. Gardner and S. Mishra, “The biomechanical environment of a bone fracture and its influence upon the morphology of healing,” *Med. Eng. Phys.*, vol. 25, no. 6, pp. 455–464, 2003, doi: 10.1016/S1350-4533(03)00036-5.

[186] P. Augat, K. Margevicius, J. Simon, S. Wolf, G. Suger, and L. Claes, “Local tissue properties in bone healing: Influence of size and stability of the osteotomy gap,” *J. Orthop. Res.*, vol. 16, no. 4, pp. 475–481, 1998, doi: 10.1002/JOR.1100160413.

[187] D. R. Epari, H. Schell, H. J. Bail, and G. N. Duda, “Instability prolongs the chondral phase during bone healing in sheep,” *Bone*, vol. 38, no. 6, pp. 864–870, 2006, doi: 10.1016/j.bone.2005.10.023.

[188] A. Vetter *et al.*, “Temporal tissue patterns in bone healing of sheep,” *J. Orthop. Res.*, vol. 28, no. 11, pp. 1440–1447, 2010, doi: 10.1002/jor.21175.

[189] J. R. Lieberman and G. E. Friedlaender, “Bone regeneration and repair: Biology and clinical applications,” *Bone Regen. Repair Biol. Clin. Appl.*, pp. 1–398, 2005, doi: 10.1385/1592598633.

[190] E. F. Morgan, H. H. Bayraktar, and T. M. Keaveny, “Trabecular bone modulus-density relationships depend on anatomic site,” *J. Biomech.*, vol. 36, no. 7, pp. 897–904, 2003, doi: 10.1016/S0021-9290(03)00071-X.

[191] I. Manjubala *et al.*, “Spatial and temporal variations of mechanical properties and mineral content of the external callus during bone healing,” *Bone*, vol. 45, no. 2, pp. 185–192, 2009, doi: 10.1016/j.bone.2009.04.249.

[192] I. L. Gitajn and E. K. Rodriguez, “Biomechanics of Musculoskeletal Injury,” *Biomech. Appl.*, 2011, doi: 10.5772/20672.

[193] K. L. L. ONG, “Orthopaedic biomaterials in research and practice, second edition.,” 2017.

[194] A. Lipphaus and U. Witzel, “Finite-Element Syntheses of Callus and Bone Remodeling: Biomechanical Study of Fracture Healing in Long Bones,” *Anat. Rec.*, vol. 301, no. 12, pp. 2112–2121, 2018, doi: 10.1002/ar.23893.

[195] M. S. Thompson, H. Schell, J. Lienau, and G. N. Duda, “Digital image correlation: A technique for determining local mechanical conditions within early bone callus,” *Med. Eng. Phys.*, vol. 29, no. 7, pp. 820–823, 2007, doi: 10.1016/j.medengphy.2006.08.012.

[196] D. P. Comiskey, B. J. MacDonald, W. T. McCartney, K. Synnott, and J. O’Byrne, “Predicting the external formation of a bone fracture callus: An optimisation approach,” *Comput. Methods Biomech. Biomed. Engin.*, vol. 15, no. 7, pp. 779–785, 2012, doi: 10.1080/10255842.2011.560843.

[197] H. Schell *et al.*, “Osteoclastic activity begins early and increases over the course of bone healing ☆,” vol. 38, pp. 547–554, 2006, doi: 10.1016/j.bone.2005.09.018.

[198] J. B. Richardson, J. Kenwright, and J. L. Cunningham, “The Clinical Biomechanics Award 1990 Fracture stiffness measurement in the assessment and management of tibia1 fractures,” pp. 75–79, 1992.

[199] J. L. Cunningham, M. Evans, J. D. Harris, and J. Kenwright, “The Measurement of Stiffness of Fractures Treated with External Fixation:,” *http://dx.doi.org/10.1243/EMED_JOUR_1987_016_051_02*, vol. 16, no. 4, pp. 229–232, 2016, doi: 10.1243/EMED_JOUR_1987_016_051_02.

[200] T. Wehner, M. Steiner, A. Ignatius, and L. Claes, “Prediction of the Time Course of Callus Stiffness as a Function of Mechanical Parameters in Experimental Rat Fracture Healing Studies - A Numerical Study,” pp. 1–16, 2014, doi: 10.1371/journal.pone.0115695.

[201] D. Lacroix, “Simulation of tissue differentiation during fracture healing,” University of Dublin, 2000.

isep Instituto Superior de Engenharia do Porto

Instituto Superior de Engenharia do Porto ⊙ Rua Dr. António Bernardino de Almeida, 431 ⊙ 4249-015 Porto
Tel. +351 228 340 500 ⊙ Fax +351 228 321 159 ⊙ mail@isep.ipp.pt ⊙ www.isep.ipp.pt

INSTITUTO SUPERIOR DE ENGENHARIA DO PORTO

isep

The Biomechanical Analysis of Bone Callus using a Meshless Method

ANDREIA FILIPA FERNANDES OLIVEIRA
Novembro de 2021

INSTITUTO SUPERIOR DE ENGENHARIA DO PORTO

MESTRADO EM ENGENHARIA BIOMÉDICA

isep

The Biomechanical Analysis of Bone Callus using a Meshless Method

ANDREIA FILIPA FERNANDES OLIVEIRA
Novembro de 2021

P.PORTO